8-2018

Functionalized and Nanostructured Fibers for Photocatalysis and Energy Conversion

Jared R. Jaksik
The University of Texas Rio Grande Valley

FUNCTIONALIZED AND NANOSTRUCTURED FIBERS FOR PHOTOCATALYSIS AND ENERGY CONVERSION

A Thesis

by

JARED R. JAKSIK

Submitted to the Graduate College of
The University of Texas Rio Grande Valley
In partial fulfillment of the requirements for the degree of

MASTER OF SCIENCE

August 2018

Major Subject: Chemistry

FUNCTIONALIZED AND NANOSTRUCTURED FIBERS

FOR PHOTOCATALYSIS AND

ENERGY CONVERSION

A Thesis
by
JARED R. JAKSIK

COMMITTEE MEMBERS

Dr. Mohammed Jasim Uddin
Chair of Committee

Dr. Jason Parsons
Committee Member

Dr. Javier Macossay-Torres
Committee Member

Dr. Hassan Ahmad
Committee Member

August 2018

ABSTRACT

Jaksik, Jared R., Functionalized and Nanostructured Fibers for Photocatalysis and Energy Conversion. Master of Science (MS), August, 2018, 103 pp., 2 tables, 24 figures, references, 167 titles.

Fiber-type / flexible materials present a unique opportunity for the incorporation of photocatalytic / energy generating technology, as they typically have a broad surface area exposed to light (clothing, curtains, carpet). In this work, several methods of harvesting incident light striking a flexible substrate to perform useful work are examined. In the first section a gold and silver nanoparticle augmented TiO_2 thin film textile coating is evaluated for its self-cleaning / UV-protective / anti-microbial properties, and stability of the film / substrate over time is examined. In the second section a dye sensitized / hybrid type solar cell architecture based on flexible carbon nanotube yarn is evaluated for its ability to convert incident light into electrical energy. In the final section an entirely polymer / hybrid based solar cell architecture also based on carbon nanotube yarn is evaluated and the relative strengths of flexible polymer-type cells are discussed.

DEDICATION

The completion of my master's studies would not have been possible without the love and support of my family. My mother, Dorothy Jaksik, my father, Raymond Jaksik, my darling, Shauna Miller, and my two hound dogs, Walter and Ruth-Ann, wholeheartedly inspired, motivated and supported me by all means to accomplish this degree. Thank you for your love and patience.

ACKNOWLEDGEMENTS

I will always be grateful to Dr. Mohammed Jasim Uddin, chair of my dissertation committee, for all his mentoring and advice. For funding my RA-ship, guiding me when the methodologies / instruments weren't cooperating, and assisting with manuscript editing, he encouraged me to complete this process through his infinite patience and relentless positivity. My thanks go to my dissertation committee members: Dr. Jason Parsons, Dr. Javier Macossay-Torres, and Dr. Hassan Ahmad. Their advice, inputs, and comments helped to ensure the quality of my intellectual work. I'd also like to thank the department chairs, Dr. Yuanbing Mao and Dr. Justin Moore, and the graduate student coordinator, Dr. Evangelia Kotsikorou for making my time in the graduate college of UTRGV great.

I would also like to thank Isaac Martinez and Jesus Salazar, undergraduates who volunteered their time to assist me with these projects, and my fellow graduate students Aminur Chowdhury and Istiak Hussain for providing moral support.

TABLE OF CONTENTS

Page

LIST OF TABLES

Page

LIST OF FIGURES

Page

CHAPTER I

INTRODUCTION

Demand for renewable and clean energy is ever increasing, and of the current sources of renewable / clean energy, solar has seen the most consumer availability and widespread utilization [1], likely due to solar energy being available everywhere unlike wind, geothermal, or hydroelectric power generation which all require specific environments to be feasible. While only 1% of global energy production was solar-derived in 2013, solar power is projected to become the largest source of energy by the year 2050 [2].

The ubiquitous presence of solar energy means that many consumer products could potentially be augmented to take advantage of solar power, however, many materials that are used in day to day applications have flexibility as a requirement: inflexible clothing would be infeasible, couches that remained rigid and unyielding when sat on would never sell, and carpets made of inflexible materials would be uncomfortable. All these objects present ideal candidates for the incorporation of photocatalysis / solar energy harvesting as they generally have a large surface area directly exposed to ambient light, but creating flexible photocatalytically-active devices presents unique challenges. Flexible substrates often have characteristics that make them challenging to create photoactive layers on: the photoactive components must themselves be either flexible, or on such a nanostructured scale that macroscale bending and stretching of the material's fibers does not disrupt them. In the case of clothing and textiles that will have direct skin contact, biocompatibility is also a key concern. In the case of solar energy harvesting

devices, traditional crystalline / polycrystalline devices built on glass substrates are wholly unsuitable for applications that require flexibility since they are built on a rigid substrate and utilize thick layers of crystalline components. The purpose of this research is to investigate the application of photocatalytic and solar energy harvesting technology to flexible, fiber-type substrates.

The portion of the solar spectrum that makes it to the earth's surface contributes 1366.1 W / m^2 of energy [3], most of which comes from photons with wavelengths that fall within the "visible" region of the electromagnetic spectrum which extends from ~390 – 700 nm [4]. Thus, for a photocatalyst to be efficient, it must absorb light strongly over and near this range. Once light has been absorbed by a photoactive material, an electron / hole pair known as an exciton is generated. In semiconductor materials separation of the electrons and the holes can take place, which is desirable as recombination leads to thermalization of the photon's energy rather than harvesting to perform useful work. For example, in the well-known photocatalyst [5] titanium dioxide, the photocatalytically generated holes are trapped at the surface of the TiO_2 within picoseconds, and can survive for microseconds, providing sufficient time for oxidation of organic species adsorbed on the surface to take place [6]. These holes are readily reactive, and if sufficient organic material is present on the surface most of them will react within 3.3 ns. As the hole is thus consumed in the oxidation of some adsorbed molecule at the TiO_2 surface, TiO_2 itself is reduced by the photogenerated electron to Ti_2O_3, or even further to other intermediate species or metallic titanium [7]. This reduction is reversible in the presence of atmospheric oxygen due to titanium's ready ability to be oxidized in air, which enable this cycle of reduction / re-oxidation by atmospheric oxygen to continue indefinitely [7]. Furthermore, if there are any hydroxyl-containing species adsorbed on the surface of the semiconductor, hydroxyl radicals can

be generated that have significantly longer lifetimes and can go on to oxidize other species [7]. Superoxide has also been detected on the surface of illuminated TiO_2 substrates, and the combination of this superoxide with an additional free hole can produce singlet oxygen, an extremely powerful oxidizer that is estimated to play an important role in the oxidation of many relatively stable organic species [8].

Cellulose, or cotton, makes up the majority of consumer textile goods, so the creation photoactive cellulose fibers could have a large impact on the consumer textile market. Solar energy along with a suitable photocatalyst can be used to mineralize stains (successively oxidizing the organic components of the stain all the way to water and carbon dioxide), effectively removing the organic / hydrophobic portion of the stain that would otherwise require detergents to remove and leaving behind only the hydrophilic components of the contaminant which can be removed with a simple rinse in water. In this research, the photocatalyst under investigation is a thin, uniform film of TiO_2, which typically only absorbs UV / near UV light, further sensitized with silver (Ag) and gold (Au) nanoparticles to absorb a longer wavelength light / a higher percentage of the solar spectrum, thus harvesting more incident photons and promoting photocatalysis more efficiently.

TiO_2 in its bulk phase absorbs UV and near UV incident light well, however without modification its photocatalytic efficiency is limited due to its limited absorption range [9]. On its own it has seen widespread testing however, having been shown to effectively mineralize a wide range of organic substances under irradiation with broad-spectrum solar light, including methylene blue [10], isothiazolin-3-ones [11], formaldehyde [12], acid orange [13], acid red [14], phenol [15], ammonia [16], and even the chemical warfare agent Soman [17]. TiO_2 is such a popular photocatalyst because its innate photocatalytic effectiveness is very high for the

reasons discussed above; a layer of TiO_2 under standard weak artificial room lighting has been found to be able to completely mineralize a 1 μm thick layer of hydrocarbon every hour [18].

Gold and silver nanoparticles are potentially great sensitizers for enhancing the absorption range of TiO_2 / allowing the efficient utilization of more visible spectrum light. Au / Ag nanoparticles have size-dependent and thus tunable absorption profiles due to the effects of surface plasmon resonance [19]. As the size of the nanoparticles is increased, the λ_{max} of the particles increases since the effects of quantum confinement are diminished and the particles are excitable by lower energy incident photons [20,21].

Silver nanoparticles have been demonstrated to reduce the incidence of electron / hole recombination when combined with TiO_2 substrates [22], which should help improve photocatalytic efficiency even further. In addition to acting as a visible light sensitizer and potentially reducing the rate of electron / hole recombination, silver nanoparticles exhibit antibacterial activity [23], and have been extensively investigated for their antibacterial effects, even in combination with cellulose for use as a packing material [24]. While macroscopic metallic silver and solutions of silver compounds have been known to have antibacterial properties for some time, recent research suggests that small (~5nm) silver nanoparticles exhibit antimicrobial activity enhanced over all other forms of silver [25]. While the mechanism by which silver (and to some extent gold) nanoparticles exhibit bactericidal properties is at present unclear, several possible mechanisms include disruption of cysteine / disulfide bonds in the proteins on the exterior of bacterial cell walls leading to decreased cell wall integrity [26], direct inhibition of ATP production [27], or through DNA degradation [28,29].

Gold nanoparticles can absorb even longer wavelengths of light than silver nanoparticles, and in tandem with silver nanoparticles can help obtain more complete coverage of the visible

spectrum [20]. Gold nanoparticles have been demonstrated to lower the effective bandgap of TiO_2 substrates, and allow for the photocatalytic mineralization of stable organics under UV-filtered / visible only lighting conditions [17]. Like silver nanoparticles, gold nanoparticles have also been shown to enhance the photocatalytic activity of TiO_2 by acting as catalytic sites / electron traps [30]. Finally, gold nanoparticles may serve an additional enhancement effect in combination with TiO_2 by improving the rate of oxygen reduction (which is consumed in the re-oxidation of the Ti_2O_3 or further reduced titanium species produced when the photocatalytically generated holes are consumed) [7].

The excitons generated from these photocatalysts can also be converted into electrical energy provided that the electron and hole are separated and transferred to different electrodes. Devices that accomplish this are referred to as solar cells, and many different types exist. The traditional rigid silicon-based cells are unsuitable for use with textiles, clothing, or in other applications that require flexibility, and this the development of flexible, fiber type cells is a popular area of research.

In the 1960's, it was discovered that illuminated organic dyes will produce electrical current at the interface between themselves and a metallic oxide electrode, which led to the construction of dye sensitized solar cells (DSSC's) [31]. These cells have five basic components: a dye which absorbs incident light to generate excitons, an oxide layer that transports the electrons away from the excited dye molecules, an electrolyte that transports the holes away from the dye, a working electrode that ultimately receives the electrons transported through the oxide layer, and a counter electrode that completes the circuit with the electrolyte and supplies electrons to reduce the holes [32]. The earliest cells utilized flat cell designs similar to modern crystalline / polycrystalline panels. These cell designs require a transparent conductive counter

electrode to both allow light to penetrate through it to the dye / oxide layer, and to complete the circuit with the electrolyte; transparent conductive oxides (TCO's) are often used for this purpose [32]. Transparent conductive oxides have several major drawbacks however, the most apparent / quantifiable being their exorbitant price (TCO production requires vacuum chambers and expensive input materials) [33], and their rigidity / ill-suitability to deployment in flexible cell architectures. Traditional flat DSSCs also characteristically utilize I^-/I_3^- redox mediators in a liquid electrolyte. Liquid electrolytes present multiple problems in that they can leak as the cells age, make the cells very prone to temperature-fluctuation induced wear, and they make production of flexible DSSC's more difficult as the electrolyte must be carefully contained.

The electrode materials used in DSSC's and indeed all types of solar cells can have a large impact on the total efficiency of the cell. The counter electrode material must demonstrate high catalytic activity to reduce the redox mediator / push electrons back into the solar cell as efficiently as possible [32]. Platinum counter electrodes lead to very high power conversion efficiencies (PCE); however, the cost of using platinum commercially would make the implementation of DSSCs expensive. The working electrode material must ideally be able to be well coated with the oxide material and should be very conductive to allow the transport of the photo-generated electrons with minimal resistance. A promising electrode material for use in three dimensional wire-type DSSCs and other flexible solar cell architectures is carbon nanotube yarn, which allows for facile chemical modification / functionalization, moderate to good conductivity, and is innately significantly more flexible than metallic wires or even conductive polymers (which tend to be somewhat brittle) [32]. The catalytic activity of carbon nanotube based substrates can be enhanced by platinization / sputtering with a small amount of platinum, and the conductivity of the working electrode, can be further enhanced with chemical techniques

such as chemical cross-dehydrogenative coupling [32]. Further enhancement of the working electrode can be accomplished by introducing mesoporous TiO_2 structures which dramatically increase the surface area and active depth of the oxide layer on the electrode surface [34]. This enhancement of surface area / active dye / TiO_2 composite depth is important because light trapping is a major consideration for dye sensitized solar cells. If the layer of dye / TiO_2 isn't thick enough light will penetrate the layer uselessly. This problem is significant since the molar absorptivity coefficient of the most common dyes used in DSSCs (which must have a broad range of absorption that overlaps with the visible spectrum) is typically fairly low, and a fair amount of research has been undertaken to develop dyes with higher molar absorptivity coefficients [35]. This particular problem is a non-issue for the organic / polymer based solar cell architecture discussed later.

For normal dye sensitized solar cells, the electrolyte / redox couple must be readily reduced / oxidized, however temperature stability, volatility, and hazards to human health / the environment must also be considered. Solid electrolytes are an emerging technology, however early attempts at utilizing a solid-state electrolyte have been found to impair cell efficiency [36]. However, the development of solid or semi solid state electrolytes could allow for the ready fabrication of wire-shaped DSSCs that have uniform performance regardless of the incident angle of the light striking them due to their shape, a factor that is completely absent in flat conventional solar panels [32].

Sensitizers can help improve cell performance over unsensitized DSSCs by allowing higher-energy incident photons to react with higher bandgap materials thereby converting more of their energy into electrical potential by avoiding the thermalization that occurs when high energy photons strike low bandgap materials [37]. These sensitizers provide additional

"junctions", or sites where photons and electrons can be separated, which improve efficiency by working around the Shockley-Queisser limit on single junction photovoltaics which predicts a maximum of 33.7% efficiency utilizing a single junction material with a bandgap of 1.34 eV [38]. This limit applies rigorously to flat junction dye sensitized solar cells even if a variety of sensitizers with different bandgaps are distributed on a two-dimensional surface, so layering of the sensitizers on the cell surface is important when trying to improve cell efficiency. Cells utilizing multiple junctions are referred to as tandem solar cells, and theoretically a perfect tandem cell with an infinite number of junctions could reach an efficiency of up to 86.8% under concentrated sunlight [39]. Even if a particular cell architecture falls well short of the 33.7% theoretical single junction efficiency, the incorporation of additional sensitizers can improve efficiency.

The main "sensitizer" in DSSCs is the dye itself. The most popular dye currently is Di-tetrabutylammonium *cis*-bis(isothiocyanato)bis(2,2'-bipyridyl-4,4'-dicarboxylato)ruthenium(II) or N719. When combined with TiO_2 it allows for rapid electron injection into the TiO_2 layer and effective charge separation, and has demonstrated good compatibility with some solid state electrolytes [40]. Theoretical and experimental absorption spectra for N719 indicate a wide energy absorption range with a maximum absorption deviation of less than 0.1 eV over that range, and it was concluded that the speed of electron injection from N719 into TiO_2 can be partially accounted for by the strong coupling between N719's absorption spectrum and density of TiO_2 unoccupied states [41]. While this strongly indicates that N719 is perhaps the best dye discovered to date for use with TiO_2 in terms of both absorption range and charge separation / injection time, N719 is currently very expensive and alternatives are being sought to replace it in DSSCs intended for commercialization.

Cadmium selenide (CdSe) quantum dots have shown promise as potential sensitizers for DSSC's and other organic based solar cells, as they decrease electron recombination and have been shown to enhance electron transfer processes, both of which increase the PCE of cells [42]. Morphologically CdSe quantum dots are non-spherical with many edges and faces, and they have been demonstrated to facilitate multiple electron injection (the conversion of high-energy incident photons into multiple lower energy electrons) which is desirable as lower energy electrons are less prone to thermalization than single high-energy electrons liberated by high intensity photons [43]. Furthermore, because they are quantum dots their size can be tweaked to alter their bandgap, which is usually around ~1.7 eV (< 770 nm) [43]. Cadmium sulfide quantum dots have a bandgap of 2.25 eV (< 550 nm), however they are more efficient at electron injection into TiO_2 than cadmium selenide because the conduction band of cadmium selenide is below that of TiO_2 [44]. The combination of these two sensitizers and their incorporation into 3-D wire-type DSSCs could improve efficiency dramatically. Furthermore, both sensitizers could be deployed in the layered, polymeric-type cell architecture, discussed below.

Polymer-based or "organic" solar cells are another important area of research that promises to produce highly efficient three-dimensional wire-type carbon nanotube based solar cells. By their nature they utilize conductive organic polymers or small organic molecules to produce excitons and facilitate charge separation in much the same way as the above outlined materials. Polymer-based cells offer unique advantages, mainly that if crystalline materials can be entirely avoided the cells will have no components that are liable to be damaged by flexing. In contrast to the above described DSSCs which require the use of a metallic oxide material, polymer based organic solar cells built on carbon nanotube yarn could potentially avoid the inclusion of oxides entirely. This type of cell architecture is composed principally of three main

components: the working electrode, counter electrode, and a pair of two polymers that act as a photoactive layer and are themselves electron / hole transporters.

In organic cells the working and counter electrodes serve as electron acceptor and electron donor respectively just like in the previously discussed DSSC cell architecture. In cutting edge cell designs it is common to use an electron transport facilitating / hole and exciton blocking layer between the polymer layer and the working electrode, to help prevent charge recombination [45]. Other than this a high work function for the working electrode and a low work function for the counter electrode is preferred to help establish a charge gradient across the organic layers, but if utilizing a combination of polymers and a blocking layer (discussed below) this isn't entirely necessary, which means that carbon nanotube yarn can potentially serve as both the working and counter electrode material in this type of cell design. Differentiation of the working and counter electrode CNTs can be accomplished via platinization or other methods of chemical modification to increase / decrease the work function of the carbon nanotube yarn as well. It should be noted that surface morphology of the electrodes, while important, is not as important for organic solar cells as it is for DSSCs which utilize oxide materials and typically low molar absorptivity dyes [46].

The organic polymers used in the photoactive region of organic solar cells typically have high molar extinction coefficients, which eliminates the need for an electrode or substrate with complex surface morphology, as is necessary with traditional oxide based DSSCs. However, a new problem introduced by this type of device architecture is the more amorphous / non-crystalline nature of the polymer materials, which can dramatically shorten exciton lifetimes. In order for excitons to dissociate they must reach an interface between the pure domains of the polymer materials used in the photoactive layer, which can be an issue if the exciton is only able

to diffuse a few nanometers within the polymer. To get around this problem while maintaining a layer of polymer thick enough to absorb the majority of incident light, a bulk heterojunction architecture was developed [47]. This architecture can be envisioned as a complex matrix of interconnecting polymer domains generated by annealing / recrystallization of a homogenous mixture of the two polymers into discrete domains composed of only a single polymer, that ultimately terminate on the working / counter electrodes [48]. The two most polymers / small molecules used for this type of device are Poly(3-hexylthiophene-2,5-diyl) (P3HT) and Phenyl-C61-butyric acid methyl ester (PCBM), and the mechanisms behind their bulk heterojunction formation and the morphology thereof have been investigated exhaustively [49–51]. Depending on annealing temperature and time, the degree of polymer self-separation and the resultant size of the domains varies, and optimization of these factors has allowed the production of purely P3HT/PCBM cells with up to 5% power conversion efficiency [51]. But this "bulk heterojunction" layer still constitutes only a single true junction, since there is only one type of junction present.

Another key advantage that organic / polymer type cells have over the other types of cells is modifiability of organic polymers to tune their bandgap, and thus the ready ability for junctions of different polymers to be successively layered, all the way to the fabled infinite junction tandem cell design discussed above. The recent record efficiency for a double junction tandem cell was just set with 15%, which, at half the efficiency of polycrystalline type cells, means that this type of cell design is becoming substantially competitive with existing solar cell technologies [45].

In summary, the goal of this research was to generate flexible, photocatalytic and photo energy harvesting materials utilizing a variety of substrates and methodologies. A thorough

investigation of TiO_2 / Ag / Au functionalized fabrics was conducted and the self-cleaning, antimicrobial, and photoprotective effects of the produced functional textile material were analyzed in depth. The methodology used for the preparation of the fabric was compatible with modern paradigms of "green chemistry", was wholly solution based / scalable, and sought to minimize the number of steps required to produce a functional textile. Two sets of carbon nanotube yarn-based dye sensitized solar cells utilizing cadmium sulfide (CdS), CdSe, PCBM, P3HT, and a traditional TiO_2 / DSSC architecture were constructed and thoroughly characterized. Finally, a set of novel carbon nanotube based DSSCs utilizing an advanced electron facilitating / hole and exciton blocking layer, in tandem with a PCBM / P3HT bulk heterojunction subject to optimized annealing conditions were constructed and characterized.

CHAPTER II

REVIEW OF LITERATURE

Functionalization of Cellulose Fibers

The development of advanced textile materials has been a popular research topic in the recent past, and textiles with a wide range of exceptional properties have been prepared including: hydrophobicity [52], bactericidality [53], UV impermeability [54], and the ability to self-cleanse organic stains [55]. Typically, the treatment methodology used to produce these functional textile materials is complex, and poorly scalable. Furthermore, while a textile material may be photocatalytic, or may possess bactericidal properties, materials that exhibit these properties in combination are rare. It is the aim of this work to produce cellulose fibers completely and uniformly coated with a thin film of TiO_2, and to enhance the photocatalytic efficiency of the semiconductor layer with the addition of Au / Ag nanoparticles.

Because TiO_2 is such a popular photocatalysts, a variety of methods have been studied for the deposition of TiO_2 thin films on a wide range of substrates. Three methods evaluated by Yuranova et al. in 2007 involved pretreatment of the textile with radio frequency plasma, microwave plasma, or vacuum-UV irradiation to functionalize the outermost layer of the fibers carboxylic acid groups that could strongly chelate the TiO_2 and secure the coating to the surface [55]. Another method employed in 2010 for the generation of a thin, uniform coating involved the use of a TiO_2 emulsion mixed with polymer-generating additives that was sprayed on the textile before the material was heated to around 100 °C to generate the TiO_2 layer [56]. And yet

another common method employs the direct growth of TiO_2 on the surface of the textile material from a titanium isopropoxide based precursor solution [57,58]. This final method of TIO_2 deposition starting with a titanium isopropoxide based precursor solution and proceeding via a room temperature sol-gel process was selected for this study as it is well developed / easy to carry out, avoids the use of environmentally harmful halogenated organics or other toxic materials, and utilizes solutions that have been observed to be stable for a period of several days, all factors which suggests good industrial scalability compared to the other methods.

Titanium dioxide (TiO_2) exists in three crystallographic phases: anatase, rutile, and brookite [59]. In bulk / thermodynamically (after high temperature annealing), rutile is the most stable phase [60]. The anatase and brookite phases are both metastable, however the brookite phase is very seldom studied due to the difficulty of its synthesis [60], and there is debate over whether or not some of the synthetic methods reported in the literature to produce "pure" brookite were even successful [61]. Regardless, for this project anatase phase TiO_2 is the synthetic objective given its apparently superior catalytic performance [60]. Despite rutile being the most stable phase of TiO_2 in bulk, the photocatalytically superior anatase phase is more thermodynamically stable in particles and films less than 11 nm thick due to crystallographic effects [62], which is convenient as the low temperature annealing of the sol-gel produced thin films can be used to ensure that the TiO_2 film / particles have reached their most thermodynamically stable state / are mostly anatase.

A "sol-gel" process is a method used for the creation of solid materials from small molecules, and it is essentially an inorganic polymerization reaction [63]. By starting with molecular precursors and proceeding via hydroxylation-condensation reactions, it becomes possible to control the morphology and structure of the produced oxide layer [63]; this method is

also very useful given that it allows fine morphology control using solution-based chemistry rather than more complex vacuum-based techniques. The parameters of concern for the sol-gel coating process include annealing temperature, and the ratio of the alkoxide precursor (titanium isopropoxide in this case) to solvent; using a higher ratio of alkoxide to solvent generates a thicker, but more defect / crack rich film, while a lower ratio of alkoxide to solvent allows for the creation of a thin, uniform, mostly homogenous film [64]. Such films have been found in previous work to be scratch, acid, and alkali resistant [64].

The most common method used for the incorporation of noble metal nanoparticles into / onto a film involves synthesizing the nanoparticles via a solution-based process, followed by separating them and applying them to the substrate by dip coating the material into a stabilized / well-dispersed colloidal suspension of nanoparticles [65], but while this method allows for the fine-tuning and optimization of nanoparticle surface morphology and size [66], it requires an additional synthetic step which makes it ill-suited for process scaling. A more straightforward and scalable method for producing the nanoparticle decorated surface would involve the direct growth of noble metal nanoparticles on the TiO_2 coated surface. It has been known since 1932 that silver nitrate and gold chloride, common precursors used to generate silver and gold nanoparticles respectively, are readily reduced on the surface of illuminated photocatalytically active oxides [67]. More recently it was discovered that noble metal nanoparticles could be grown directly on the surface of certain polysaccharides, presumably with the native functional groups acting to reduce the precursor compounds when exposed to UV irradiation [68,69]. The authors found no nanoparticle growth when testing this method with glass / other inert substrates, which suggests that the cellulosic medium plays a key role in the photoreduction of the precursor salts, even absent any traditional photocatalyst. Thus, the combination of the photocatalytic

activity of the TiO_2 thin film with the apparent photo-activity of cellulose itself when under UV irradiation should be more than sufficient to directly reduce the noble metal nanoparticle precursors and produce TiO_2 coated / gold and silver nanoparticle decorated cellulosic fibers directly, without the need for separate preparation of the nanoparticles.

Because this experiment wasn't concerned with solar power generation, characterization of the photocatalytic activity was performed utilizing two organic stain analogs: methylene blue and Congo red. These two dyes show markedly different susceptibility to photocatalytic mineralization; methylene blue is commonly used as a stain analog in photocatalysis experiments because it is readily degraded, whereas Congo red is significantly more stable / resistant to photooxidation [70]. Methylene blue is typically present as its monomeric, dimeric, and trimeric forms which have λ_{max} values of 673, 596, and 570 nm respectively [71], whereas Congo red has a single λ_{max} of 497 nm. The combination of these two dyes should serve as an appropriate analog for a wide variety of colored, variably stable organic stains, and their strong absorption should make quantitative analysis of the photocatalytic properties of the produced oxide / metal nanoparticle coating straightforward via:

$$\ln\left(\frac{[C]}{[C]_0}\right) = -kt$$

which assumes that the stain decomposition follows roughly first-order kinetics.

Flexible Dye-Sensitized Solar Cells

Flexible solar cell technology is a wide and varied field, with many approaches being tried to address the fundamental problems encountered with flexible devices: finding flexibility-compatible photoactive materials, achieving good fabrication yield (the ratio of the produced

cells that function to those that are inoperable due to some fabrication-related defect), keeping fabrication and material costs low, and producing devices that are stable over many hours of light exposure and many flexing cycles [32]. Two major cell architectures were tested in this work, one based on a more traditional dye sensitized solar cell architecture, and one based on a modern organic / polymer solar cell architecture. Research into novel, non-silicon based cells is progressing rapidly; the promise of cheaper and competitively efficient solar cells based on newly developed materials (like carbon nanotubes) is very enticing (Figure 1).

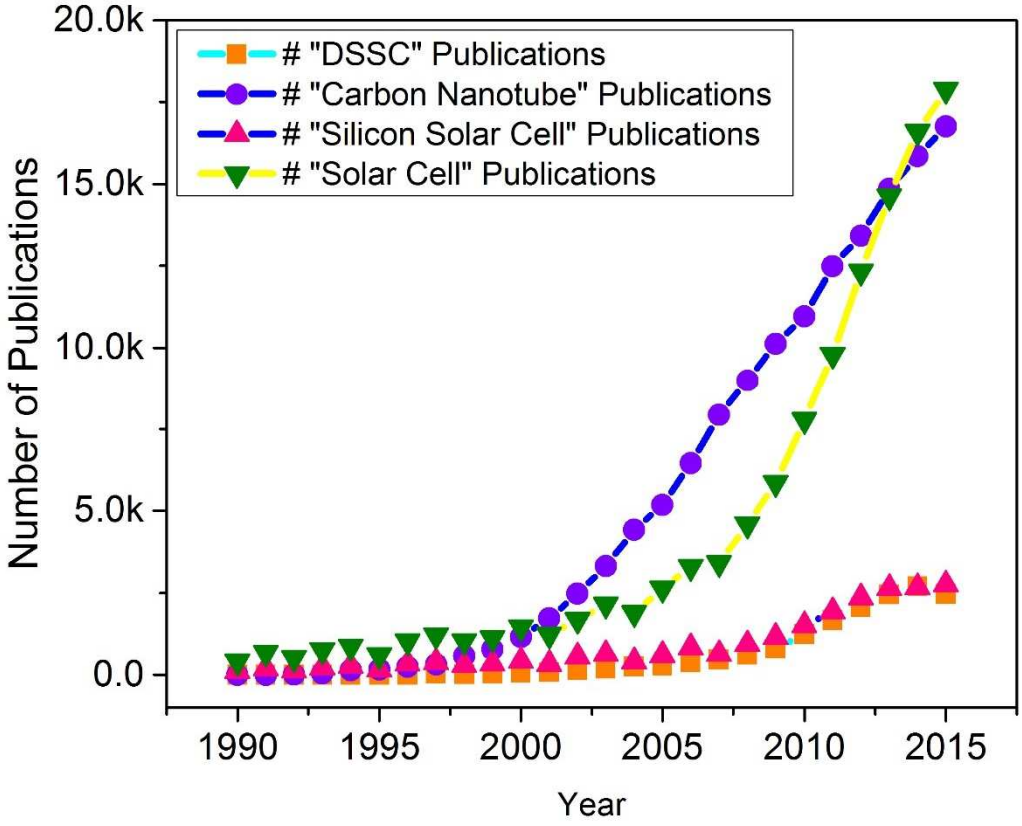

Figure 1: Research Trends Pertaining to Dye Sensitized Solar Cells, Carbon Nanotubes, Silicon Solar Cells, and Solar Cells Generally (Jaksik et al.) [32].

The choice of the material for the working electrode has a dramatic effect on the flexibility of the final cell. Because electrons are injected into the working electrode, it must itself be resistant to oxidation and degradation with prolonged use. Elemental carbon is an ideal candidate for a working electrode material, given its high resistance to oxidation, flexibility in certain forms, and somewhat facile surface functionalization / modification; carbon has been deployed as a working electrode for DSSCs as a powder [72], as aligned nanotubes (increasing electrode conductivity) [73], as freestanding nanotube arrays grown on graphene sheets [74], and as nanotubes incorporated into a polymer-based matrix [75]. Typically, the performance of carbon nanotube-based devices is reported treating the produced carbon nanotubes as a simple homogenous bulk substance, and including a few SEM images and some morphological characterization. This greatly complicates the analysis of the published results as the electronic properties of carbon nanotubes can vary greatly depending on their exact chirality, average degree of interalignment within the material / average bending degree of the individual tubes, average number of "walls" per tube, whether or not residual solvents or other components are trapped within the tubes during device fabrication, degree of coupling between the tubes, etc.

Carbon nanotube-based devices are typically compared to the more traditional device architectures that utilize a metallic working electrode. With the use of a titanium based working electrode, the TiO_2 layer morphology and thickness can be carefully controlled as the oxide layer can be produced through simple anodization [76]. This type of metal-wire supported cell does suffer some limits to its flexibility however, and repeated flexing can cause metal fatigue which can weaken the working electrode. For example, TiO_2 / Platinum (Pt) wire based DSSCs have been fabricated with PCEs of up to 5.4 %, and they were bendable / shapeable, however they showed gradually diminishing PCE with repeated reshaping [77]. It is likely that cells based on

carbon nanotubes would suffer this performance decrease with repeated flexing and reshaping much less as metal fatigue and crystallographic effects within the bulk material of the working / counter electrodes are a non-issue. Another type of device architecture based on metal wires is the waveguide fiber-type structure with solar concentrators, and it has been explored in some detail [78]. This type of cell has good potential for converting the light passing through windows into electrical energy to help offset electricity, and with the use of concentrators overall cell surface area / the costs of fabrication can be reduced while still allowing for a large area of sunlight to be harvested.

A titanium wire based photoanode with a TiO_2 micron-cone-nanowire array structure was produced to help alleviate some of the typical efficiency reduction that occurs after repeated flexing when utilizing a metallic working electrode [79]. While this device's architecture reduces the strain on the oxide layer with flexing, it is still metal based, however it was able to retain 96.6 % of its initial PCE (4.75 % max) after being flexed 100 times [79]. Another group prepared a 3D network of TiO_2 on titanium foil which retained 97.3 % of its initial PCE (4.98 %) after twenty consecutive bends [80]. While whether or not the reduction in efficiency of 3.4 % after 100 flex cycles or 2.7 % after 20 flex cycles is low enough to allow for commercialization is obviously debatable depending on the intended application of the cell, titanium wire / foil-based cells remain popular for initial testing of novel TiO_2 based cell architectures.

The electrophoretic deposition of graphene-TiO_2 hierarchical spheres on titanium thread was tested as a means to generate an oxide layer with more varied morphology to increase light-trapping by allowing for reflection between the spheres [81]. This type of deposition technique and surface morphology could be adapted to improve the PCE of other types of photoanodes. A careful analysis of a basic titanium wire / titania core device architecture was performed and neat

carbon nanotubes, core-sheath carbon nanotube (CNT) / reduced graphene oxide nanoribbon, CNT / reduced graphene oxide composite, and reduced graphene oxide fibers were all evaluated for their relative performance as counter electrode materials, and a PCE of 5.64 % was obtained from the CNT / reduced graphene oxide nano ribbon electrode [82]. They also found that if this material was platinized (a small amount of platinum deposited on the surface of the electrode by physical vapor deposition / "sputtering") they were able to improve the efficiency to 6.83 %.

The incorporation of platinum provides catalytic sites where the reduction of the electrolyte can proceed more rapidly, however platinum is expensive and even when used sparingly its inclusion can potentially make the cells prohibitively expensive to produce and replacements for platinum are a key area of carbon-based solar cell research. $CoNi_2S_4$ nanoribbon can be grown on carbon nanofibers in a single step, and has been used in cells producing up to 7.03 % conversion efficiency, which is competitive with cells utilizing platinum wire counter electrodes [83]. The same research group also investigated porous titanium nitride nanoplates as a potential surface coating for carbon fibers to improve electrolyte reduction rate / overall PCE, and was able to obtain 7.20 % PCE [83]. Many different materials, such as other metallic nitrides, carbides, sulfides, and oxides have all shown promising results when deployed in traditional flat solar cell architectures, thus, progressive investigations towards new and facile methods of coating these inorganic metal compounds onto the highly-curved surface morphologies of carbon nanofibers will potentially lead to platinum free / less expensive fiber-type DSSC architectures [32,83].

Carbon "nano-felt" has also been evaluated as a cost-effective DSSC counter electrode, and a counter electrode composed of this material when utilized in a conventional DSSC system was able to achieve up to 6.94 % PCE [84]. Carbon fibers are also good candidates for

deployment as counter electrodes due to their extensive flexibility, which allows them to be wrapped around other more inflexible substrates such as metal wire [85]. Carbon fibers are readily functionalizable, and the exposed functional groups on their surface can be modified through treatment utilizing a variety of methods [86]. Furthermore, carbon nanotubes can readily be used as a substrate for growing nanocrystals for use in DSSCs. Cadmium sulfide nanowire crystals were grown around a carbon fiber which served as the core electrode, and dye / polymer layers were deposited over top of this to create a core-shell photovoltaic device [87]. While this device architecture obtained only very low PCE, the successful growth of CdS crystals and attempting to utilize them in a solar cell architecture which also includes dye / traditional components of DSSCs in a type of hybrid cell is interesting. Cadmium sulfide on its own is a notable photocatalyst and thus its inclusion can even further enhance cell efficiency.

These hybrid-type carbon nanotube-based cells have the potential to be substantially competitive with silicon-based devices in the near future, however a major hurdle that still needs to be overcome is the liquid electrolyte. The liquid electrolyte impairs cell stability over time and also, more severely, limits the cells to being deployed in environments where the electrolyte won't be allowed to freeze, which is a massive drawback [88]. A cell architecture utilizing carbon nanotube yarn as both the working and counter electrodes, and with a semi-solid state electrolyte has been evaluated and achieved a max PCE of 2.57 %, with prolonged stability [89]. Through the incorporation of cadmium sulfide and cadmium selenide quantum dots they were able to raise the PCE to 6.4 %, a notable achievement given the use of carbon-based working and counter electrodes [89].

Quantum dots such as the cadmium sulfide and cadmium selenide utilized in the above reference work are a current popular area of research, both for the development of new more

powerful types of lasers / LEDS and for use in other physics-based applications [90], and for their potential applicability to solar cells [91]. Quantum dots have several properties that make them ideally suited for use as solar cell sensitizers, including generally high molar absorptivity coefficients which helps minimize the thickness of the required active layer of the quantum dots and thus promotes better charge separation, tunable band gaps based on quantum dot size, and the ability to generate multiple charge carriers when absorbing light with a higher energy than the bandgap of the quantum dot [92,93]. However, the efficiency of produced quantum-dot based solar cells up to this point has been limited by charge recombination / the difficulty in utilizing quantum dots in the traditional DSSC architecture which utilizes a porous or highly irregular working electrode surface to increase the thickness of the photoactive layer.

Cadmium sulfide (CdS) and cadmium selenide (CdSe) are potentially good candidates to replace the first generation quantum dot sensitizers which use lead compounds [92] that are toxic to the environment and pose a significant safety hazard, and research into replacements for lead / other acutely toxic heavy metals has been an important subfield within the green chemistry movement for some time [94]. While cadmium is also a heavy metal and poses health risks, it is markedly less prevalent in the environment and exposures must be larger than that of lead to produce negative health outcomes [95,96].

The bandgap of quantum dots in general can be experimentally determined via analysis of the band edge present in the UV-Vis spectrum of the material, and this information can be used to approximate the size of the quantum dots, or vice-versa, via:

$$\Delta E = \frac{h^2\pi^2}{2R^2}\left[\frac{1}{m_e} + \frac{1}{m_h}\right] - \frac{1.8\,e^2}{\varepsilon_2 R} + polarization\ term$$

Where R is the particle's radius, ε is the dielectric constant, and ΔE is the confinement-induced shift in the energy of the conduction band (added to the bandgap of the bulk material to

determine the bandgap of the quantum dots) [97]. It is readily apparent that as particle size is decreased, the bandgap of the material is increased, and a variety of experiments have demonstrated the size-dependence of the bandgap on small (< 50 nm) particles of semiconductors [98]. Because the bulk bandgap of cadmium sulfide is ~ 2.25 eV and that of cadmium selenide is ~1.7 eV, and because both of these bandgaps can be increased with size-control of the nanoparticles, it's obvious how a large range of bandgaps are accessible utilizing just these two materials.

It should also be noted that cadmium sulfide nanostructures, depending on the synthetic process used, can take on a wide range of morphologies, including nanoparticles, nanowires / nanorods, nanobelts, and nanospheres [97]. Likewise, cadmium selenide also has a wide range of accessible nanostructured morphologies available utilizing facile synthetic techniques [99,100]. A couple different cadmium sulfide preparation methods were attempted over the course of this work with a focus on nanorods and nanoparticles specifically.

Organic / Polymer Based Hybrid Solar Cells

The last type of device architecture investigated in this work is the polymer-based or organic solar cell, based on a bulk heterojunction. As discussed briefly in the introduction, this type of device architecture is based entirely on small molecules / amorphous polymers which should theoretically allow for complete device flexibility due to the lack of any crystalline / polycrystalline materials. While great advances towards the achievement of flexible devices based on crystalline oxide materials have been made, recent achievements in the field of organic / polymer-based cell technology make this type of device architecture more promising than ever for the development of efficient, fully flexible, and stable cells that can be produced with good

fabrication yields due to the more straightforward method of generating the photoactive layer [45].

Polymers in general have garnered a great deal of interest among solar cell researchers as they present a class of novel materials that can be used to improve the characteristics of traditional device architectures. TiO_2 based DSSCs built upon conductive plastic substrates via a selective sintering method have been evaluated [101], and this laser-based fabrication method could potentially be used to generate devices on a roll-to-roll scale. Flexible, ultrathin polyaniline nanoribbons have been tested as a counter electrode material for TiO_2 based DSSCs, and cells utilizing them were able to achieve up to 7.23 % PCE [102]. UV-catalyzed cross linkable polymers have also been evaluated as a way to replace the liquid electrolyte and improve overall cell stability, and testing on polymer / metal mesh based DSSCs utilizing this solid-state electrolyte yielded reasonable efficiency [103].

Thus, we've seen that polymers have been evaluated as to their potential to enhance the characteristics of the working electrode, counter electrode, and the electrolyte. But the class of cells known as organic or polymer solar cells utilizes polymers as the actual photoactive material. As noted earlier the organic polymers used in this type of cell often have molar absorptivity coefficients much larger than that of the organic dyes used in traditional DSSCs, which means that a thinner layer of the polymers is necessary to absorb most of the incident photons. However, due to the fairly amorphous and irregular nature of the polymer matrix, exciton lifetime and thus diffusion distance is dramatically shortened. The increased molar absorptivity is not sufficient to completely offset this reduced exciton diffusion distance, and thus the bulk heterojunction cell morphology was developed [47].

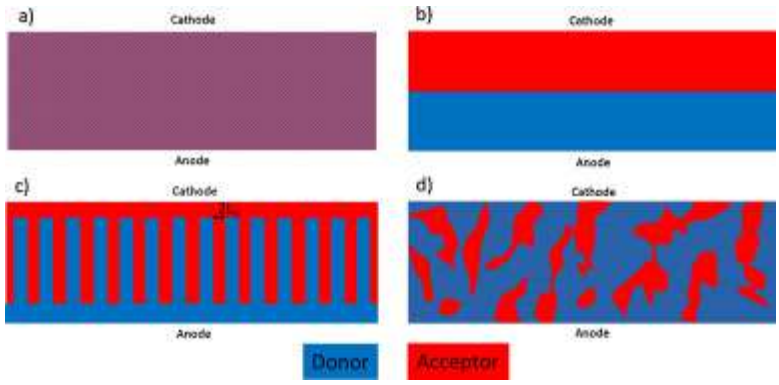

Figure 2. Schematic Cross-Section of Nanomorphologies of Bulk Heterojunction Colar Cells. (a) Fine Mixture of Donor and Acceptor Molecules, (b) Bilayer Arrangement, (c) Theoretical Ideal Morphology of Bulk Heterojunction Solar Cells and (d) Typical Morphology of a Solution Processed Device (Scharber et al.) [47].

To generate the morphology apparent in Figure 2 (d) above, a fine mixture of two polymers is prepared (in the case of this work P3HT and PCBM were used), and then the polymer layer is annealed for a period of time to promote the self-separation of the intimate polymer mix into pure domains intermixed with one another. Due to the complexity of the produced layer and the parameters involved with the generation of the intermixed bulk heterojunction architecture (including annealing temperature, duration, and solvent characteristics / quantity), a great deal of research has gone into computationally modeling and optimizing bulk heterojunction characteristics [104]. There is some debate over whether or not bulk heterojunction layer morphology has a dramatic impact on cell efficiency in this type of device or not, with some studies like the previously cited one being entirely focused on the theoretical modeling of bulk heterojunction layer morphology and characteristics with the aim of improving overall cell efficiency, and other studies [47] conceding that while nanomorphologic considerations are important for optimization of a particular combination of materials, ultimately they have little to do with the overall efficiency limit of this type of device.

As per the Shockley-Queisser limit discussed earlier [38], the theoretical efficiency limit of a single junction device is 33.7 %. However polymer-based cells have an additional advantage over traditional DSSC / oxide based cell designs, and that is their ready amenability to multi-junction cell architectures [45]. Through the pairing of different polymers, the effective bandgap of the devices can be varied, in the above cited work, two different pairs of polymers were utilized with the high-bandgap pair being placed in front of the low bandgap pair. Thus, incident high energy photons are absorbed and usefully converted to electrical energy, while the lower energy photons pass through this high bandgap layer to the rear cell where they are in turn absorbed and converted by the low bandgap polymer pair.

The oxide layer in traditional cells serves to separate the working electrode, and the already-injected electrons flowing along it, from the rest of the cell / electrolyte / recombination sites. In organic solar cells 1,3,5-Tri(m-pyridin-3-ylphenyl)benzene (TmPyPb) is often employed for this purpose as it allows the transfer of electrons but blocks the movement of holes and undissociated excitons [105]. A further method for improving the degree of charge separation in P3HT / PCBM based polymeric solar cells is the insertion of a blocking layer composed of pure PCBM between the P3HT:PCBM layer and the working electrode, ensuring that the working electrode is entirely in intimate contact with PCBM and not in contact with P3HT; the insertion of this layer has been observed to increase overall cell efficiency from 3.57 % to 4.24 % for a standard P3HT:PCBM cell architecture [106].

To replace the liquid iodine-based electrolyte typically used in flexible cells, poly(3,4-ethylenedioxythiophene) polystyrene sulfonate (PEDOT:PSS), a water-soluble conductive polymer, can simply be coated over the exterior of the polymer-based cell [45]. This approach works in polymer based cells because the outermost surface of the polymeric bulk heterojunction

layer is fairly flat, in sharp contrast to the DSSC architectures where interpenetration of the electrolyte into the complex morphology of the dye impregnated porous TiO_2 layer is vital to ensure good hold diffusion / cell efficiency [107]. This is another fundamental difference between DSSC and organic / polymer-based cell architecture, and another advantage that polymer-based cells have in terms of potential for large scale manufacture prolonged device stability in the environment.

On the topic of device stability however polymer-based bulk heterojunction devices do have a key drawback. As already discussed, the bulk heterojunction layer is produced by the thermal annealing of a homogenous mixture of the two organic molecules (P3HT:PCBM in this case). This causes spontaneous phase separation, and localized pure domains of the two components are generated via a process called Ostwald ripening [108]. Ostwald ripening occurs because large particulates or domains are thermodynamically more stable than small ones in a mixture of two components as large particulates minimizes the relative interfacial surface area between different domains, which lowers the overall energy of the system. This process has a couple negative implications for bulk heterojunction cells, namely that the pure domains in the polymer mixture will continue to grow spontaneously and this rate of growth is dependent on the amount of thermal energy present, thus making the cells somewhat innately temperature unstable. It should be noted that the lower molecular weight component of the bulk heterojunction layer (in this case PCBM) is more likely to diffuse, thus another important topic of research for the production of polymer based solar cells has been the development of polymers that effectively suppress fullerene (or lower molecular weight material generally) diffusion [109]. This is beyond the scope of this work as standard P3HT:PCBM was used however cell stability was considered.

Of the synthetic techniques used to assemble the cells, the most important one used was solution-based layer deposition, or dip coating. Dip coating has received a remarkable amount of interest in the literature due to its ability to be easily scaled to produce devices on a roll-to-roll or continuous assembly line [110]. Furthermore since the use of large vacuum chambers to manufacture the FTO / ITO transparent conductive oxide glass substrates for traditional silicon / polycrystalline solar cells accounts for 60% of their manufacturing cost [32], solution based / scalable synthetic techniques are vital to reduce the manufacturing costs of the next generation of solar cells.

The mechanism of dip coating can be theoretically approximated by considering a flat, uniform, infinite plate being moved at constant velocity out of a vessel containing the coating solution, a situation already examined in the literature [111] and now colloquially known as the "Landau-Levich problem". The thickness of a film produced by withdrawing of a submerged flat substrate from a solution at constant speed can be approximated via:

$$h = 0.94 \frac{(\eta u)^{\frac{2}{3}}}{\gamma^{\frac{1}{6}}(\rho g)^{\frac{1}{2}}}$$

where h is the thickness of the thin film, η is the viscosity of the coating solution, u is the constant linear speed of withdrawal from the coating solution, γ is the liquid-vapor surface tension, ρ is the density of the coating solution, and g is acceleration due to gravity [111,112]. This relationship holds well when the withdrawal speeds are between 1 and 10 mm/s and the viscosity of the coating liquid is relatively low [112]. From this equation we can see that numerous variables influence the thickness of the produced thin films of liquid when an object is coated via dip coating. Further complicating factors include the variability in solution viscosity

when the material that is to be coated is dissolved (or dispersed in the case of suspensions used for coating) in it, the variability in solution liquid-vapor surface tension (as well as viscosity) when polymers of variable molecular weights are incorporated [113], and the innate problem of surface effects caused by previously deposited layers of material.

This simplest approximation assumes that the substrate being withdrawn from the coating solution is an infinitely large plate with negligible edges, however the substrate used in the construction of the dye sensitized / hybrid polymer solar cells produced in this work is carbon nanofiber yarn / thread, which is roughly cylindrical and thus, while this simple approximation can yield approximate values for the final thickness of the thin films produced on this cylindrical substrate, the theoretical analysis of the mechanisms behind dip coating on a cylindrical substrate is complex [114]. Further complicating the theoretical analysis of the dip coating process on the carbon nanotube yarn / thread substrates used in this work is the fact that the surface of the carbon nanotube yarn, while roughly cylindrical, is both highly irregular and semi-porous due to the interwoven nature of the individual carbon nanotubes that make up the yarn. Thus, the parameters used to establish the thickness of the produced films will be based on the previous work done in the field in cases of the photocatalytic TiO_2 thin film for the Ag-Au/TiO_2 functionalized cellulose [115–118], and the dip coating based deposition of colloidally suspended TiO_2 for the porous oxide layer of the traditional architecture DSSC-based cells [89,119–121]. However, for the hybrid / polymer type cells a more careful analysis of the dip coating process was carried out to generate the experimental parameters and predict the thickness of the various layers, since the materials used in the preparation of the polymer-type cells were fairly novel.

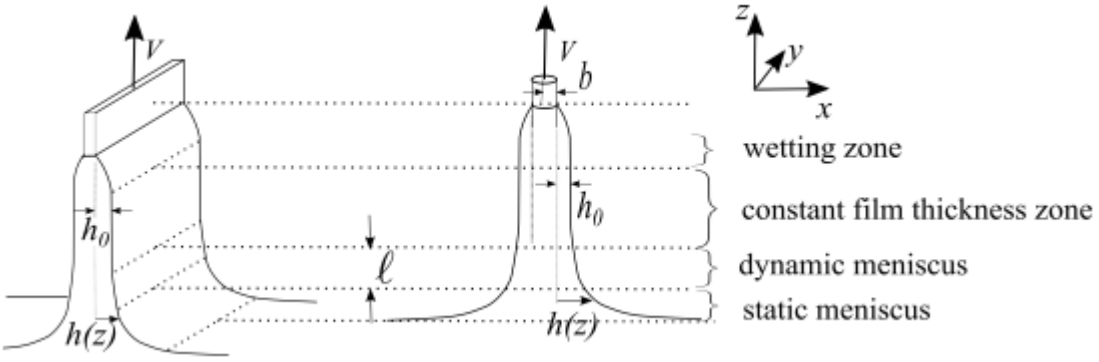

Figure 3. Coating of a Solid Pulled at a Velocity *V* Outside a Liquid Bath in a Plate (left) or a Fiber (right) Geometry. The Liquid is Sheared in the Dynamic Meniscus, Whose Length is *l*. A Film of Constant Thickness is Formed Between This Dynamic Meniscus and the Wetting Zone (Rio et al.) [122].

From Figure 3 we can see that the dip coating process occurs over a series of four "zones" [122]. Both the static and dynamic meniscus zones are responsible for determining the thickness of the thin film present in the constant film thickness zone. The height of the static meniscus is given by the equilibrium between hydrostatic and capillary pressures via:

$$h_m = \sqrt{2} l_c$$

where l_c, the capillary length, is given by:

$$l_c = \sqrt{\frac{\gamma}{\rho g}}$$

where γ is the surface tension, ρ is the density of the liquid, and g is acceleration due to gravity [122]. In the case of fibers however the static meniscus is also affected by the curvature of the fiber itself, and if the radius of the fiber (*b*) is significantly smaller than the capillary length

(predicted via the above equation), the height of the meniscus simply becomes $h_m = \sqrt{2}b$ since the azimuthal curvature of the fiber has a greater effect than the vertical curvature at the fiber / liquid interface [122]. To determine which radius of curvature has a larger effect on the formation of the meniscus, we can calculate the Goucher number [123], which quantifies the relative importance of the two types of curvature [122], via:

$$\mathrm{Go} = \frac{b}{l_c}$$

which for the carbon nanotube yarn / thread used in this work (with an outer diameter of ~ 100 μm) in conjunction with a coating solution of chlorobenzene (which has a surface tension of 0.03299 N m^{-1} at 25 °C [124], and a density of 1110 kg m^{-3} [125]) is:

$$\mathrm{Go} = \frac{50 * 10^{-6}\ \mathrm{m}}{\sqrt{\frac{0.03299\ \frac{\mathrm{N}}{\mathrm{m}}}{1100\ \frac{\mathrm{kg}}{\mathrm{m}^3} * 9.98\ \frac{\mathrm{m}}{\mathrm{s}^2}}}} = 16.6\ .$$

Thus, even though the substrate is fiber-shaped, given the relatively low viscosity of chlorobenzene / the coating solution the contribution of the azimuthal curvature of the fiber to meniscus formation is negligible, so the simple approximation would be incorrect; in this case the height of the static meniscus is better-approximated by $h_m = \sqrt{2}l_c$.

While the height of the static meniscus is important, it is the characteristics of the dynamic meniscus that ultimately determine the thickness of the film in the constant film thickness zone [111]. The forces acting in the dynamic zone can be thought of as shear (viscous) stress, and the force of capillary pressure [122]. The viscous stress gradient is balanced by the capillary pressure gradient via:

$$\frac{\eta V}{h_0^2} \sim \frac{\gamma h_0}{l^3}$$

where l is the length of the dynamic meniscus which is given by $l^p = \sqrt{h_0 l_c}$ for plates, since the diameter of the fibers used in this work is not sufficiently small enough to warrant treatment as fibers (in which case $l^f = \sqrt{h_0 b}$). With all this considered, we end up with:

$$\frac{h_0}{l_c} = 0.94 \left(\frac{\eta V}{\gamma}\right)^{\frac{2}{3}}$$

which neglects density / gravity and is valid up to capillary numbers ($\mathrm{Ca} = \left(\frac{\eta V}{\gamma}\right)$) of 10^{-3}. To test if this approximation is valid we can calculate the capillary number of chlorobenzene, the solvent that was used to dip coat the TmPyPB and pure PCBM layers for the polymer / hybrid type cell structure, knowing that the viscosity (η) of chlorobenzene is 0.753 mPa at 25 °C [124], the linear speed of withdrawal from the solution is 1 cm s^{-1}, and the surface tension of chlorobenzene at 25 °C is 0.03299 N m^{-1} [124]:

$$\mathrm{Ca} = \left(\frac{[.753 * 10^{-3}\ \mathrm{Pa\ s}] * \left[0.01\ \frac{\mathrm{m}}{\mathrm{s}}\right]}{0.03299 \frac{\mathrm{N}}{\mathrm{m}}}\right) = 2.28 * 10^{-4}$$

thus, because the capillary number is smaller than 10^{-3}, the Landau-Levich regime is an appropriate approximation for the dip coating carried out in this work.

Finally, the thickness of the thin film of chlorobenzene deposited on the ~100 μm diameter yarn at a withdrawal rate of 1 cm s^{-1} can be calculated as follows [122]:

$$h_0 = 0.94 * \left(\frac{[.753 * 10^{-3}\ \text{Pa s}] * \left[0.01\ \frac{\text{m}}{\text{s}}\right]}{0.03299 \frac{\text{N}}{\text{m}}} \right)^{\frac{2}{3}} * \sqrt{\frac{0.03299\ \frac{\text{N}}{\text{m}}}{1100\ \frac{\text{kg}}{\text{m}^3} * 9.98\ \frac{\text{m}}{\text{s}^2}}} = 6.08\ \mu m$$

With this information, we can calculate the concentrations required to produce the various layers of the polymer / hybrid type solar cells via a completely solution-based dip-coating methodology, as explained below.

For the polymeric / hybrid type cell architecture, there are four polymeric layers that must be deposited on the carbon nanotube yarn / thread-based substrate via dip coating. The first layer to be directly deposited directly onto the carbon nanotube yarn is the TmPyPB electron transport / hole blocking layer. In previous works this compound or close / relatively low molecular weight analogs have been deposited via vacuum deposition [45], spin coating [126], and ultrasonic spray coating [127], the latter two of which are solution-based methods, thus TmPyPB should be amenable to dip coating onto carbon nanotube yarn. The target thin film layer thickness to serve as a hole / back-recombination blocking layer without providing significant resistance to electron transport (thereby impairing overall cell efficiency) is ~ 5nm [45]. In order to approximate the concentration of TmPyPB in chlorobenzene necessary to deposit an ~5nm thick layer in a single dip coating step (assuming a low concentration of TmPyPB / negligible volumetric change upon addition of TmPyPB to the chlorobenzene), we can use the above information regarding the approximate thickness of the chlorobenzene thin film deposited with those parameters (6.08 μm), the density of TmPyPB (estimated to be ~1.2 g cm^{-3} based on similar compounds [128]), and the molecular weight of TmPyPB of 537.65 g mol^{-1} [129] to calculate the amount of TmPyPB that should be used to prepare 10 mL of coating dip-coating solution via:

$$\text{grams TmPyPB} = \frac{5 * 10^{-9}\ \text{m}}{6.08 * 10^{-6}\ \text{m}} * 10\ \text{cm}^3 * 1.2\ \frac{\text{g}}{\text{cm}^3} = 8.22\ \text{mg}$$

The second layer is deposited over top of the TmPyPB is a pure PCBM layer to serve as backing for the P3HT:PCBM bulk heterojunction layer, the use of which has been shown to improve bulk heterojunction device performance in comparison with bulk heterojunction devices whose architecture potentially allows a P3HT domain to come into direct contact with the working electrode / electron transport layer [106]. The optimal thickness of this layer from previous work was determined to be ~15 nm [106]. Once again, PCBM has been commonly deposited via spin coating to ensure good coating homogeneity, however a simpler dip-coating based approach is preferred with fiber-type substrates due to the inherent difficulty of spin coating a three-dimensional substrate. Using the same assumptions as the dip coating of TmPyPB, utilizing chlorobenzene as a solvent once against since it is a good solvent for PCBM [130], and knowing that the density is PCBM is ~ 1.5 g cm^{-3} [131] we can calculate the amount of PCBM required to prepare 10 mL of dip coating solution via:

$$\text{grams PCBM} = \frac{15 * 10^{-9}\ \text{m}}{6.08 * 10^{-6}\ \text{m}} * 10\ \text{cm}^3 * 1.5\ \frac{\text{g}}{\text{cm}^3} = 37\ \text{mg}$$

The bulk heterojunction layer (the mixture of P3HT / PCBM) will be prepared as a binary mixture of P3HT (solubilized in chloroform) and PCBM (solubilized in chlorobenzene), since this method of preparing the bulk heterojunction precursor solution has been demonstrated to yield favorable results [130]. Despite some work showing that a variable weight ratio of P3HT:PCBM (namely the use of additional P3HT relative to the weight percentage of PCBM) could potentially increase efficiency [132], there are a number of theoretical and experimental studies demonstrating that there is insufficient evidence to conclude that any weight ratio other

than 1:1 will produce cells with optimal efficiency [133], so a 1:1 ratio of the two compounds will be used. The optimal thickness of this layer, which is the main photoactive layer, is around 200 nm to ensure complete absorption of incident light [106,133], however this thickness is also subject to optimization as excess thickness can impair charge transfer. We can estimate the viscosity of a 1:1 by volume mixture of chloroform and chlorobenzene via the Gambill method [134]:

$$\eta^{\frac{1}{3}} = 0.5\ (.753 * 10^{-3}\ \text{Pa s})^{\frac{1}{3}} + 0.5\ (.542 * 10^{-3}\ \text{Pa s})^{\frac{1}{3}}$$

and thus we obtain .641 mPa s for a 1:1 mixture of chloroform and chlorobenzene. Calculation of the surface tension of a mixture of liquids is considerably more complex [135,136], however a simple average is usually close if the surface tension of the components do not vary too widely, thus the surface tension of the 1:1 mixture of chloroform and chlorobenzene can be estimated as .02983 N m^{-1}. Because the mixture is similar to chlorobenzene it is assumed that the previous approximations still apply. With the density of the 1:1 mixture being the average of chlorobenzene and chloroform (1.11 g cm^{-3} and 1.49 g cm^{-3} respectively) the thickness of solvent thin film produced by dip coating can be calculated via:

$$h_0 = 0.94 * \left(\frac{[.641 * 10^{-3}\ \text{Pa s}] * \left[0.01\ \frac{\text{m}}{\text{s}}\right]}{0.02983 \frac{\text{N}}{\text{m}}} \right)^{\frac{2}{3}} * \sqrt{\frac{0.02983\ \frac{\text{N}}{\text{m}}}{1300\ \frac{\text{kg}}{\text{m}^3} * 9.98\ \frac{\text{m}}{\text{s}^2}}} = 5.10\ \mu m$$

With the density of the PCBM / P3HT mixture equal to the average of the density of the two components: 1.5 g cm^{-3} for PCBM and 1.1 g cm^{-3} for P3HT thus 1.3 g cm^{-3} for a 1:1 by weight mixture, we can calculate the amount of PCBM/P3HT required for ten mL of the dip coating solution:

$$\text{grams P3HT/PCBM} = \frac{200 * 10^{-9}\ \text{m}}{5.10 * 10^{-6}\ \text{m}} * 10\ \text{cm}^3 * 1.3\ \frac{\text{g}}{\text{cm}^3} = 509.8\ \text{mg}$$

this is a significantly larger amount of dissolved material than the other dip coating solutions, and it is not immediately clear whether or not half of that amount of P3HT / PCBM will be soluble in 5 mL of chloroform / chlorobenzene respectively [130]. P3HT solubility in chloroform from the literature is estimated as 14.1 mg / mL which means that the solubility limit for 5 mL of chloroform would be ~ 70.5 mg [130]. PCBM is more soluble in chlorobenzene however, with a literature solubility value of ~59.5 mg / mL in chlorobenzene, meaning that ~ 300 mg of PCBM could be readily dissolved in 5 mL of chlorobenzene [130]. To simplify the solution preparation process however a series of four discrete dip coating steps will be performed, meaning that the total mass of 1:1 P3HT/ PCBM required in the dip coating solution is just 127 mg, so 63.7 mg of P3HT will be used, which is a small enough amount to ensure complete dissolution in the dip coating solution.

The last layer that will be deposited for the polymer / hybrid type cell structure is the PEDOT:PSS transparent / conductive counter electrode layer. In the literature PEDOT:PSS is commonly deposited via a number of methods including dip coating [137], and its deposition is fairly straightforward given its solubility in water. Thus, distilled water will be used as the coating solvent for the deposition of PEDOT:PSS. The ideal thickness of this layer is ~50 nm to ensure that charge transfer is adequate, but also that the film is thin enough to not block too much incident light [45]. To ensure that the contribution of the azimuthal curvature of the fiber was still negligible with water which is a more viscous solvent, the Goucher number was recalculated for the carbon nanotube fiber / water system and is 6.93, which is still much larger than one, so approximating the cylindrical fiber as a plate is still appropriate. Furthermore, to

ensure that the Landau-Levich regime is appropriate the capillary number for water assuming a withdrawal rate of 1 cm s^{-1} was calculated and determined to be 0.000124, which is still less than 10^{-3} so this approximation is also still appropriate. Thus, the thickness of the thin film of water resulting from dip coating of the carbon nanotube yarn can be calculated via:

$$h_0 = 0.94 * \left(\frac{[.8937 * 10^{-3}\ \text{Pa s}] * \left[0.01\ \frac{\text{m}}{\text{s}}\right]}{0.07197 \frac{\text{N}}{\text{m}}} \right)^{\frac{2}{3}} * \sqrt{\frac{0.07197\ \frac{\text{N}}{\text{m}}}{1000\ \frac{\text{kg}}{\text{m}^3} * 9.98\ \frac{\text{m}}{\text{s}^2}}} = 6.28\ \mu m$$

and, with the density of dried coatings of PEDOT:PSS = 1.011 g cm^{-3} [138], we can calculate the amount of PEDOT:PSS required for 10 mL of dip coating solution via:

$$\text{grams PEDOT: PSS} = \frac{50 * 10^{-9}\ \text{m}}{6.28 * 10^{-6}\ \text{m}} * 10\ \text{cm}^3 * 1.011\ \frac{\text{g}}{\text{cm}^3} = 80\ \text{mg}$$

CHAPTER III

METHODOLOGY AND FINDINGS

Functionalization of Cellulose Fibers

The functionalized cotton fibers were prepared as follows: acetone, 2-propanol, titanium isopropoxide, hydrochloric acid, silver nitrate, and glacial acetic acid were purchased from Sigma Aldrich. Gold chloride was purchased from Acros Organics. The raw cotton fibers that were used for morphological characterization were obtained from an agricultural plot in the Rio Grande Valley, Texas. Pure 100% cotton fiber was also obtained from the Rio Grande Valley, Texas, United States.

The raw cotton fibers and the 100% cotton fabric were soxhlet extracted with acetone for a period of 3 hours to remove any impurities that may be present like natural waxes and oils. After washing, the cotton fibers and fabric were allowed to dry at room temperature for twelve hours. The nanostructured interface was generated using the procedure reported in previous work [57] which is as follows: the nanosol solution used for coating the fibers was prepared as two separate solutions: (a) containing 50 mL of 2-propanol, 1 mL acetic acid, and 5.91 mL titanium isopropoxide and (b) containing 50 mL of 2-propanol, 3 mL concentrated hydrochloric acid, and 0.72 mL of mili-Q water. Both solutions were stirred vigorously for a period of 30 minutes, and then solution B was slowly added to solution A under vigorous (400-800 rpm) stirring. The cotton fibers were immersed in the thus prepared nanosol solution for 30 seconds, and then

allowed to dry for 24 hours. The nanosol solution was observed to maintain its integrity / clarityfor one week before degrading and polymerizing / qualitatively appearing to precipitate out TiO_2 and become opaque, which suggests that this coating solution would be ideal for re-use and cost efficiency. Calcination of the fibers to remove residual solvent was then performed at 65 °C for ten minutes and then 90 °C for five minutes. The calcined fibers were hydrothermally treated to remove excess oxide for a period of three hours. The pristine / control fiber samples were subjected to the same calcination and hydrothermal treatment process; however they were not coated with the nanosol TiO_2 solution.

With the TiO_2 coating applied, the gold and silver nanoparticle direct growth was performed: 2 mM solutions of gold chloride ($AuCl_3$) and silver nitrate ($AgNO_3$) were prepared and serially diluted to create additional 100 mL solutions of 1 mM and 0.5 mM $AuCl_3$ and $AgNO_3$. The fiber samples were immersed in these solutions for thirty second and allowed to dry in air at room temperature for 24 hours. Finally, the $AuCl_3$ and $AgNO_3$ / TiO_2 coated fiber samples were exposed to 254 nm UV radiation in an Ultra-Violet Productions CL-1000 ultraviolet crosslinker for a period of thirty minutes. The gold coated samples were seen to take on a purple coloration after the development of the nanoparticles under UV light, while the silver nanoparticle coated samples took on a characteristic brown coloration. A total of sixteen fiber samples were prepared, two each of: 0.5 mM $AuTiO_2$, 1 mM Au-TiO_2, 2 mM Au-TiO_2, 0.5 mM Ag-TiO_2, 1 mM Ag-TiO_2, 2 mM Ag-TiO_2, TiO_2 only, and pristine cotton. Additional 5 mM Ag-TiO_2 and 5 mM Au-TiO_2 samples were prepared for UV-Vis characterization of the nanoparticles grown on the TiO_2 fabric surface. Two replicates of each sample were prepared for stain testing with Congo red and methylene blue separately.

Methylene blue (0.001% w/v and 0.1% w/v) and Congo red (0.1% w/v) solutions were prepared from Milli-Q water (ultrapure water produced from a Milli-Q Integral Water Purification System) and the corresponding compounds (purchased from Sigma Aldrich). The fiber samples were scanned via UV-Vis spectroscopy (methodology below) prior to staining, and staining was conducted by simply immersing the fiber samples in a stirred solution of the dye for ten minutes. Stain uptake was qualitatively observed to be slower for the TiO_2 / nanoparticle coated samples compared to the pristine fiber, likely due to the mild hydrophobic properties imparted by the TiO_2 coating, and so the ten-minute interval with stirring was necessary. Staining of the fiber samples was performed multiple times to verify that the photocatalytic activity of the TiO_2 / nanoparticle coated samples wasn't decreased with repeated staining events followed by UV exposure. The two initial cycles staining of the methylene blue treated samples were performed with the 0.001% w/v methylene blue solution while the third staining was done with the 0.1 % w/v solution. The Congo red samples were stained only once with the prepared 0.1 % w/v Congo Red solution. Stain extinction was observed to be virtually complete between staining events. For UV-Vis analysis the fiber samples were mounted on custom made rigid plexiglass sample holders that easily mounted to the instrument and ensured that the same area / orientation of the fabric samples was being scanned each time, and the fiber samples were kept mounted on the sample holders during UV exposure to ensure uniform / flat exposure of the fiber surface.

Exposure of the fiber samples to simulated solar light was carried out using a Honle UV-Technology UVACUBE 400 USA. Stained fiber samples were placed in the solar simulator and exposed to simulated solar light (AM 1.5), and then UV-Vis scans were performed to verify the extinction of the stain. UV-Vis measurements were carried out using a Perkin Elmer Lambda

950 UV-Vis-NIR spectrometer equipped with a 150 nm integrating sphere for reflectance measurements. All scans were acquired over the full range of the instrument (2500-250 nm) with 1 nm resolution. Fourier-transform infrared spectroscopic analysis was carried out using a Perkin Elmer Frontier FTIR spectrometer, and data was collected in absorbance mode over the full range of the instrument (4000-450 cm^{-1}). Samples for FTIR analysis were prepared by thoroughly mixing 25 mg of finely divided Au-TiO_2 and pristine cotton fibers with 25 nm of optical grade potassium bromide (purchased from International Crystal Labs), and pressing of the mixture into a thin, one-inch diameter pellet using a hydraulic press. The pellets were very fragile and were directly transferred onto copper tape (to act as a rigid backing) with a hole such that the IR beam was obstructed only by the pellet. FTIR samples were repeatedly exposed to simulated solar light in the same solar simulator used for UV-Vis characterization and were scanned at regular two-hour intervals.

SEM and EDS characterization of the Ag/Au-TiO_2 cotton fiber samples was performed using a JEOL 7800F Field Emission Scanning Electron Microscope, equipped with an Electron Dispersive X-ray Spectroscopy system (EX-37270VUP). Preparation for AFM characterization of the Ag/Au-TiO_2 cotton fibers was carried out by stretching and gluing the cotton fibers to a flat mica surface using double-sided tape. AFM imaging was performed using a Bruker Bio-Scope Catalyst AFM microscope (Bruker, Santa Barbara, CA). Si cantilevers with spring constants of 0.4 N/m and resonance frequencies of 300 kHz were selected for this measurement. AFM height and deflection images were recorded using tapping mode at room temperature. While height images provide quantitative surface topography information, the deflection images exhibit a higher contrast of morphological details. Image processing of the data was performed

using WSxM 5.0 (Nanotex Electronica, Spain) software. XRD analysis was carried out using the D2 Phaser 2nd Gen X-ray diffractometer D5000 X-ray diffractometer (Bruker).

Verification of the anti-microbial properties of the Ag/Au-TiO_2 coated cotton fiber was carried out using the Kirby-Bauer disk diffusion method. Agar plates were inoculated with *Escherichia coli* bacteria. A 2 cm diameter rough disk, derived from the above prepared fiber samples, was placed in the center of each plate. Plates were then incubated at 37 °C for a period of 72 hours, and the zone of inhibition was measured in millimeters after the incubation period.

Analysis via SEM revealed that the TiO_2 coated cotton fiber samples were uniformly coated, and the coating was thin enough so that the natural folds present in the cotton fibers were still visible through the folds, although a slight decrease in the definition of the folds is visible after the TiO_2 coating is applied (Figure 4-a,b,c,d). This is desirable as these folds increase the exposed surface area of the fiber and can improve photocatalytic efficiency by allowing more sites for photoreactions to take place and a large surface area for the anchoring of the gold and silver nanoparticles, furthermore, it allows a large surface area for the absorption of the organic stains or other organic matter that will be photocatalytically decomposed, which has been shown to increase the rate of decomposition [139]. The growth of gold and silver nanoparticles on the TiO_2 coated cellulose fibers was verified as successful as a number of small particulates were present (Figure 4-e,f,g,h). Additionally, although some loose aggregates / nanoparticle clusters are visible in the high magnification images (Figure 4-f,h), they are not grafted to the surface / fiber.

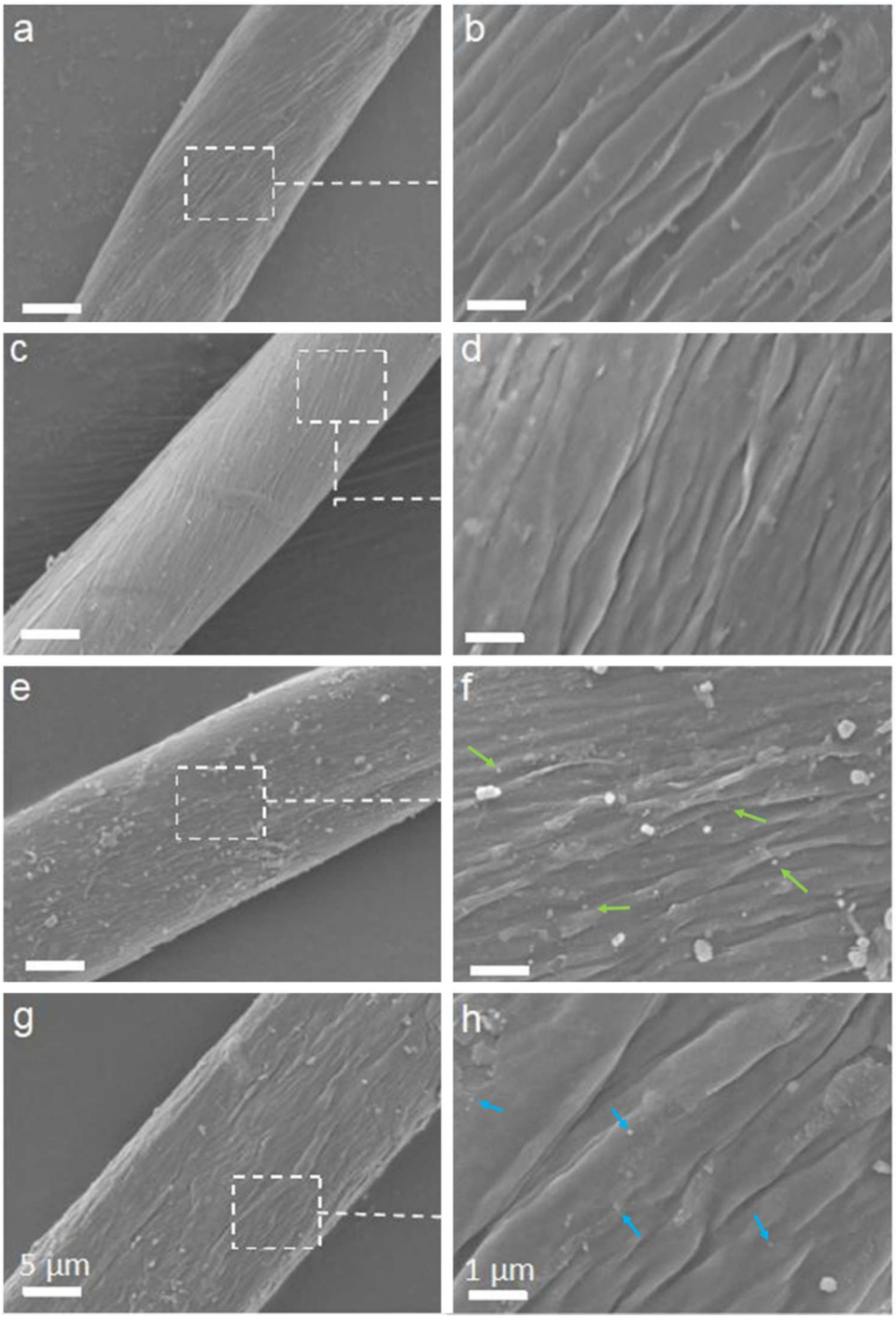

Figure 4. SEM Imaging of the TiO_2 Coated and Pristine Cotton Fibers at Low and High Magnification: (a,b) Pristine Untreated Cotton, (c,d) TiO_2 Coated Cotton Fiber, (e,f) Ag-TiO_2 Coated Cotton Fiber with Non-agglomerated Ag Nanoparticles Marked (green arrows), and (g,h)

Au-TiO_2 Coated Cotton Fiber with Non-agglomerated Au Nanoparticles Marked (blue arrows). The Scales for all Images in the Left and Right Columns are the Same.

Analysis via EDS mapping revealed that the TiO_2 coating was indeed uniform across the entire surface of the fibers with no cracking (Figure 5-a,b,c), which is desirable as it protects the underlying cotton fiber from staining or degradation by acting as a protective barrier. Additionally, spot EDS analysis of the particulates that are clearly visible in Figure 5-f indicated that they were silver particles that had been successfully grown on the fiber's surface. Note that because gold was sputtered on the yarns prior to EDS / SEM analysis the gold peak is present in all of the collected EDS spectra. The heat mapping is the most important result obtained from the EDS data as it helps verify that the coating process was successful, and that complete coverage of the fibers was obtained. Furthermore Figure 5-c is presented to verify that no TiO_2 or other titanium-based contamination was accidentally applied to or already present in the pristine control sample that was used to provide a comparison for the photocatalytic assessment.

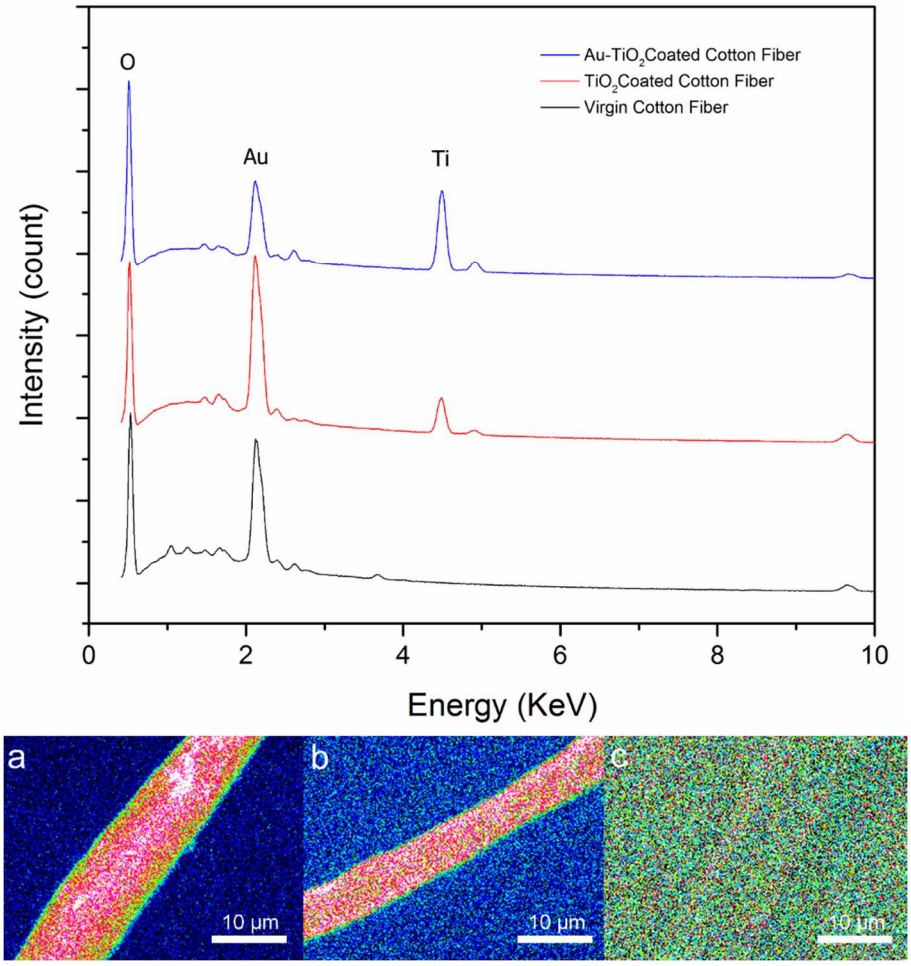

Figure 5. EDS Spectra of the TiO_2 Coated and Pristine Cotton Fibers. Heat Map Showing the Distribution of Titanium on the Surface of the: a) Au-TiO_2 Coated Fiber, b) TiO_2 Coated Fiber, and c) Pristine Cotton Fiber.

The final morphological characterization technique used was atomic force microscopy (AFM). AFM analysis was complicated by a number of factors, not the least of which being that fibrous materials are exceptionally hard to stabilize for the purposes of performing AFM, which depends on having an immobilized substrate to interact with the vibrating tip. However through trial and error stabilized samples were obtained, and AFM analysis of the pristine and TiO_2

coated cotton fibers also revealed the TiO_2 coating to be uniformly deposited, however some areas of aggregation of TiO_2 on the surface of the treated fibers were visible (Figure 6-c,d). These clusters of aggregated TiO_2 further increase the photocatalytic activity by increasing the area for stain molecules to adsorb on the surface of the fibers [139,140], by promoting light scattering and absorption across the surface of the TiO_2 coated fiber rather than penetration or reflection [141], and by providing more sites for the anchoring of noble metal nanoparticles with good interfacial contact between themselves and the TiO_2 layer, which is markedly important for the enhancement of photocatalytic activity by the metallic nanoparticles [142]. In the AFM images (Figure 6-a,b,c,d) the definition of the natural folds of the cotton fibers visible through the TiO_2 coating appear to be even more reduced than in the SEM, although this may just be due to a difference in imaging technique / because AFM relies on having a completely immobilized substrate to a large degree than SEM, the lack of complete immobilization may have reduced detail contrast / definitely contributed to the slight blurring visible in Figure 6-d. Regardless, it is evident that the TiO_2 layer has been evenly adhered to the fiber surface and covers the entirety of the fibers.

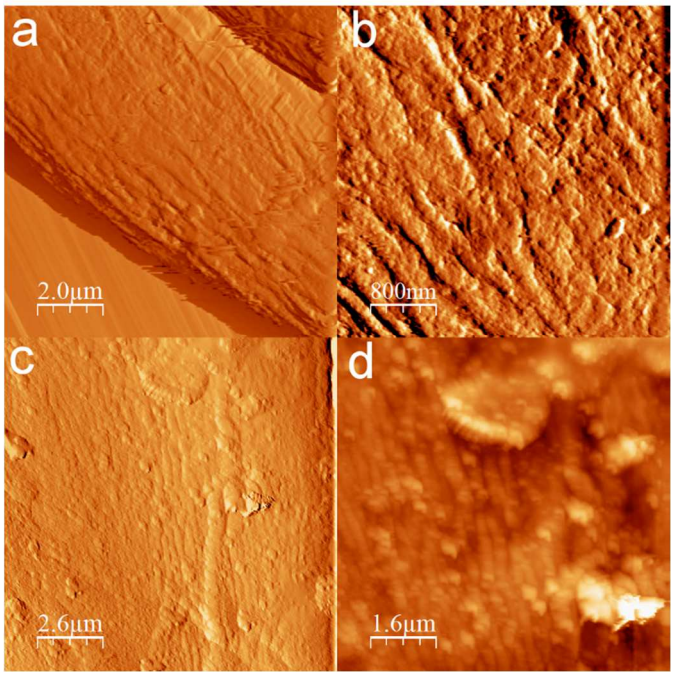

Figure 6. AFM Scans of (a,b) Pristine Cotton Fiber and (c,d) TiO_2 Coated Cotton Fiber.

With verification of the efficacy of the coating process (Figures 4-6), characterization of the electrical / physical properties of the nanoparticle coated samples was performed using UV-Vis spectroscopy. The samples coated with the 5 mM precursor solutions of $AgNO_3$ / $AuCl_3$ were analyzed after photoreduction of the precursors / development of the nanoparticles was completed under UV light exposure (Figure 7). Using approximations based on the equation relating nanoparticle size / bandgap presented in the literature review section, and other data concerning the relationship between the physical size of gold nanoparticles and their electronic properties, the gold λ_{max} of 547 nm matches up with what would be expected if the gold nanoparticles took on roughly spherical shapes [143], and had an average size between 60 and 80 nm [20,144]. More precisely from the work of Haiss et al., the nanoparticle diameter can be calculated from:

$$d = \frac{\ln(\frac{\lambda_{spr} - \lambda_0}{L_1})}{L_2}$$

When d > 25 nm and where $\lambda_0 = 512$, $L_1 = 6.53$, and $L_2 = 0.0216$ with less than 3% error [144]. Using the wavelength of maximum absorption of 547 nm we estimate that the gold nanoparticles are, on average, 77 nm in diameter. Qualitatively based on the width the gold absorption peak (Figure 7) it is evident that nanoparticles with a range of sizes were generated on the TiO_2 coating, which is to be expected given the non-size selective nature of the synthetic method employed.

The silver nanoparticle λ_{max} at 440 nm closely matches what would be expected if the average size of the nanoparticles was between 40 and 60 nm [21]. More precisely based on available literature information it is like that the average size of the silver particle was close to 55 nm [25], however no convenient analytical chemistry equations relating nanoparticle size to λ_{max} have been derived in the literature. As in the case of the gold nanoparticles marked peak broadening was present (Figure 7) suggesting that a range of nanoparticle sizes were generated by the direct-reduction synthetic technique.

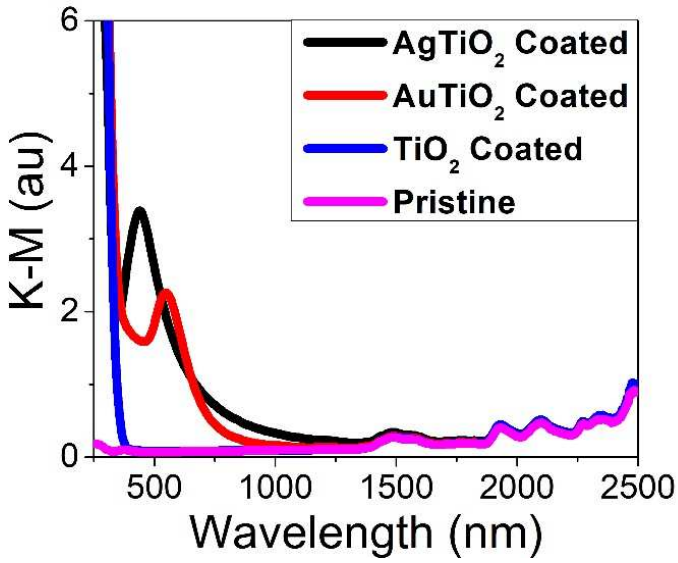

Figure 7. UV-Vis Spectra of the Fiber Samples Prepared with 5 mM Precursor Solutions Prior to Staining, with the Nanoparticle Peaks Visible.

XRD analysis of the fabric samples was also carried out, however the low proportion of TiO_2 present in the thin film coating made the signal from the TiO_2 coating very weak, but some semblance of peaks corresponding to anatase phase TiO_2 is visible when directly compared to the pristine cotton fiber sample (Figure 8). Characteristic peaks corresponding to cotton fibers at 16.27°, 20.67°, and 22.31° [145] are readily apparent on the XRD spectra, while additional peaks 29.38°, 43.84°, and 56.05° due to the presence of anatase phase TiO_2 are visible upon close inspection (Figure 8).

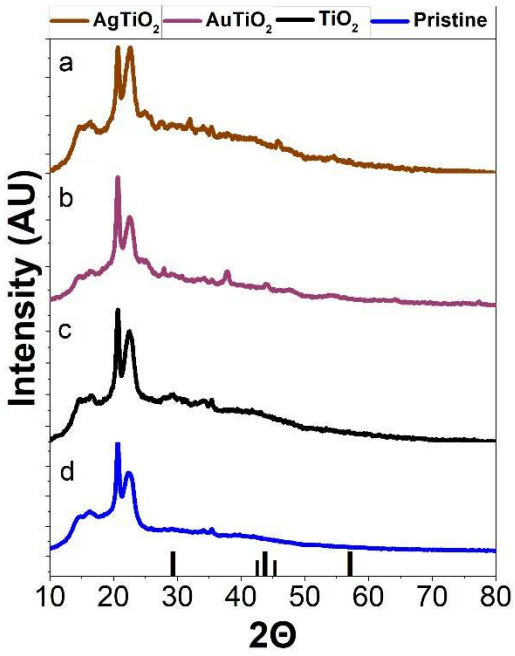

Figure 8. XRD Spectra for (a) $AgTiO_2$ Coated Cotton Fibers, (b) $AuTiO_2$ Coated Cotton Fibers, (c) TiO_2 Coated Cotton Fibers, and (d) Pristine Uncoated Cotton Fibers.

The UV-Vis spectra acquired from the stain extinction testing of the fiber samples clearly show that the methylene blue stain is removed by the Ag/Au-TiO_2 coating at a faster rate than that of the pristine cotton sample (Figures 9, 10). As discussed earlier methylene blue is present as monomeric, dimeric, and trimeric forms with λ_{max} values of 673, 596, and 570 nm respectively [71]. The mineralization of the dimeric and trimeric forms can be seen to proceed more rapidly than the decay of the monomeric form. Nonetheless, the breakdown of methylene blue proceeds much more quickly for the fiber samples that have been coated with TiO_2, and further improvement of the rate of decay is obtained when gold / silver nanoparticles are deposited on the fibers. The rate of extinction for each type of sample was obtained by subtracting the pre-stain UV-Vis spectra from the spectra obtained at each time interval and integrating the resulting

subtracted spectra over the entirety of the range of the peak due to the methylene blue (or Congo red) dye absorbance (475 to 750 nm in the case of methylene blue) (Figure 9).

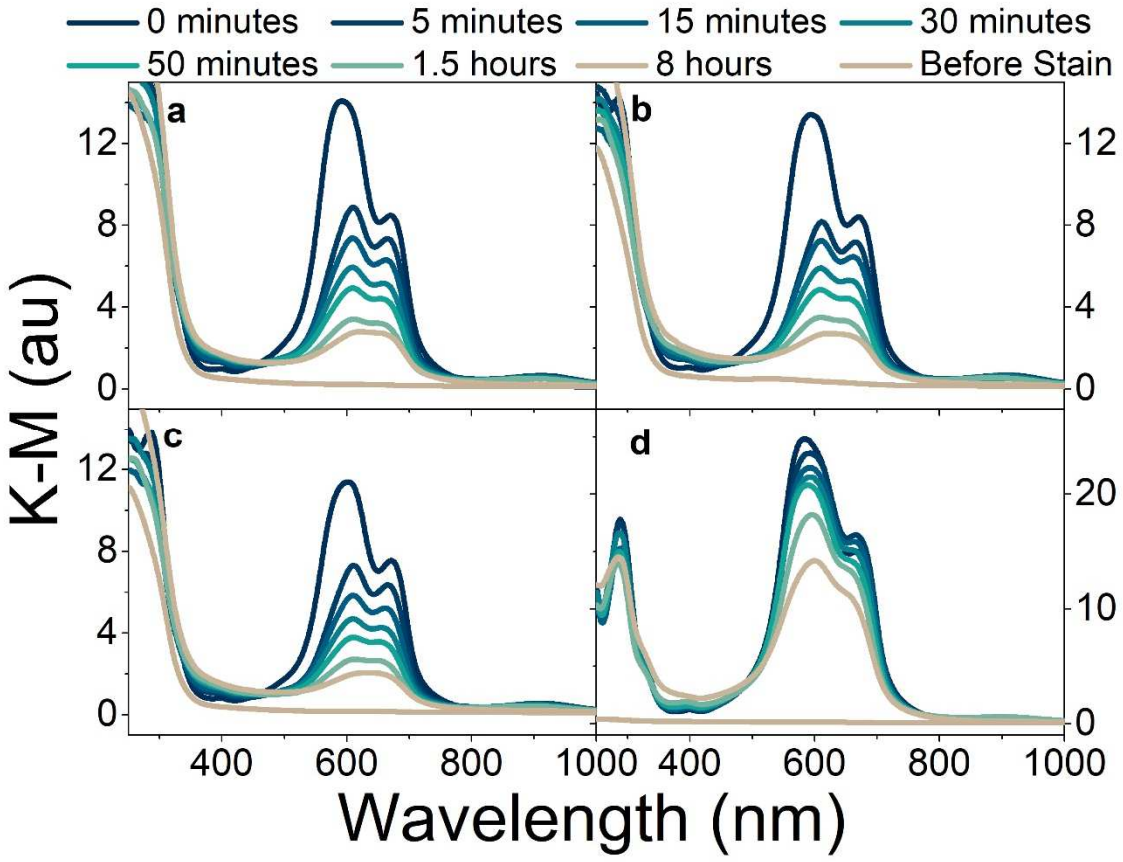

Figure 9. UV-Vis spectra of the TiO_2 / Nanoparticle Coated Samples after Staining with Methylene Blue, and upon exposure to Simulated Solar Light: a) 1mM Ag-TiO_2 Coated Fibers, b) 1 mM Au-TiO_2 Coated Fibers, c) TiO_2 Coated Fibers and d) Pristine Cotton Fibers. Note that the Rate of Stain Extinction is Significantly Increased on the Nanoparticle / TiO_2 Coated Samples Compared to the Pristine Fabric.

While the 1 mM precursor concentration data qualitatively demonstrates that the rate of stain extinction was improved with the use of TiO_2, it is more difficult to see the effect that the noble metal nanoparticles had on the rate of stain extinction from Figure 9. The results of the

variable concentration tests are presented in Figure 10, and from them it is apparent that with the increasing concentration of noble metal nanoparticle the rate of methylene blue stain mineralization was increased.

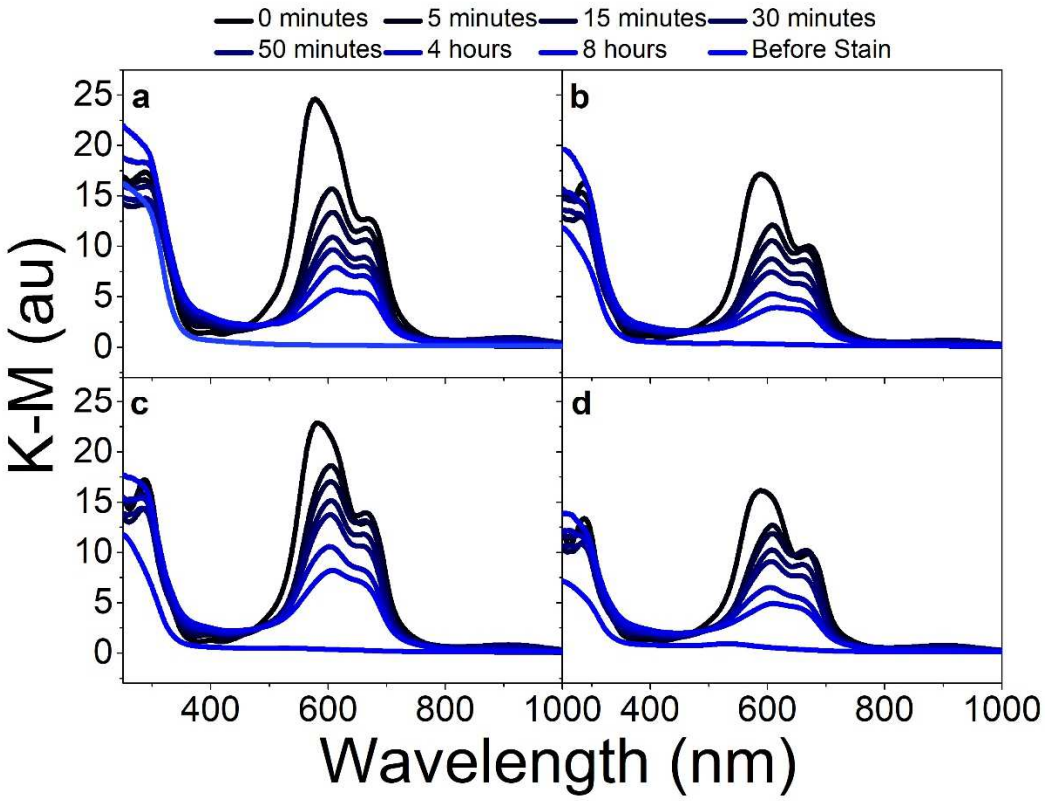

Figure 10. UV-Vis Spectra of the TiO_2 / Nanoparticle Coated Samples after Staining with Methylene Blue, and upon Exposure to Simulated Solar Light: a) 0.5 mM Ag-TiO_2 Coated Fibers, b) 0.5 mM Au-TiO_2 Coated Fibers, c) 2 mM AgTiO_2 Coated Fibers, and d) 2 mM AuTiO_2 Coated Fibers. Note That the Concentration of Metallic Nanoparticles on the Fiber Surface is Increased from Left to Right.

Again, as noted earlier the mineralization kinetics are roughly first order so the standard first order kinetic equation was used. Integrating these peaks and plotting them as first order kinetic graphs allowed roughly linear fitting (Figure 10) and direct calculation of the kinetic

constants. However, based on the tail ends of the kinetic graphs it is likely that the photocatalytic mineralization isn't exactly first order (as the plots appear to show some exponential characteristics) however the extinction data for the pristine / untreated cotton fiber appears to be exactly first order / linear. Regardless, the rate of extinction was reduced for the pristine sample and increased for all the other samples (Figure 11).

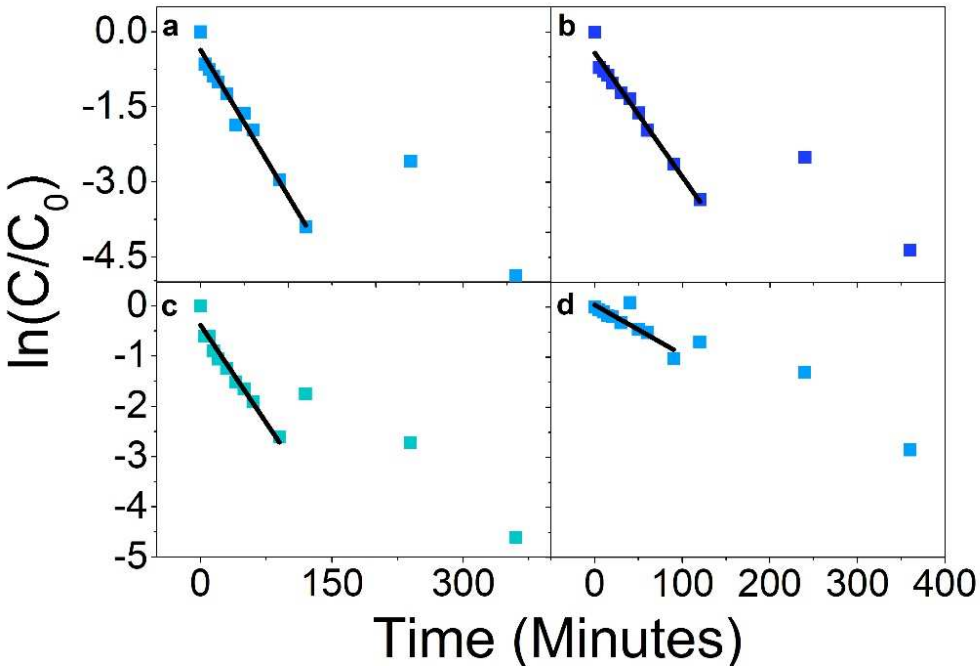

Figure 11. The Natural Log of the Ratio of the Methylene Blue Peak Area to the Initial Stain Peak Area Upon Repeated Exposure to Simulated Solar Light for Au/Ag-TiO_2 Fiber Samples: a) 1 mM Ag-TiO_2 Coated Fibers, b) 1mM AuTiO_2 Coated Fibers, c) Fibers Coated with TiO_2 Only and d) Pristine Cotton Fibers. Note That The Rate of Stain Extinction is Much Slower for the Pristine Fiber Sample, and That it Appears to Follow Absolute First Order Kinetics.

With this fitting it is even more apparent that the rate of methylene blue mineralization is improved with the addition of an Ag/Au-TiO_2 coating. Kinetic data for the variable nanoparticle concentrations is presented at Figure 12, and this data is more difficult to interpret. Due to the somewhat second or higher order kinetics apparently involved with photocatalytic methylene blue decomposition fitting and the obtaining of kinetic values is difficult. However, by examining the relative final concentration ratio (the concentration ratio after 360 minutes of simulated solar light exposure) it becomes apparent that increasing nanoparticle concentration did have a positive effect (Figure 12-c,d) however quantitative analysis of this effect is difficult, as will be evidenced by the tabulated methylene blue extinction data. It is likely that this non-first order effect is due to interconversion between the monomer, dimer, and trimer of methylene blue during the process of photocatalytic decomposition, and the subtly different molar absorptivities that these different chemical species possess [146]. However an effort was made to extract quantitative kinetic data from the experimental results, and this same issue was not as prevalent with the Congo red staining data.

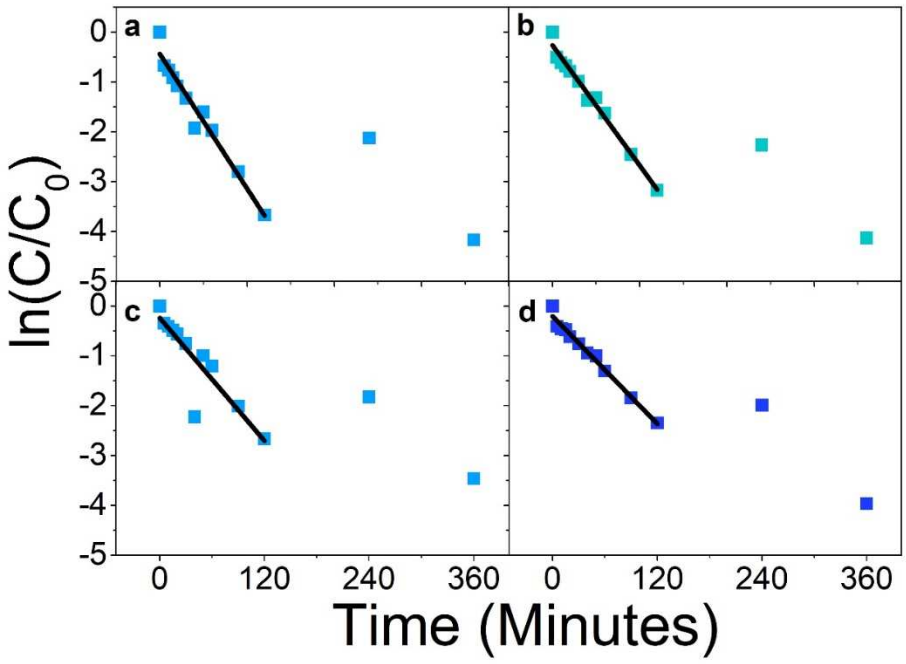

Figure 12. The Natural Log of the Ratio of Methylene Blue Peak Area to Starting Peak Area Upon Repeated Exposure to Simulated Solar Light for TiO_2 / Nanoparticle Coated Fiber Samples: a) 0.5 mM Ag-TiO_2 Coated Fibers, b) 0.5 mM Au-TiO_2 Coated Fibers, c) 2 mM Ag-TiO_2 Coated Fibers and d) 2 mM Au-TiO_2 Coated Fibers.

The tabulated data is somewhat difficult to interpret as noted above. Even though the TiO_2 / nanoparticle coated samples mineralized a large fraction of the stain after a set period of time, the lack of exactly first order kinetic data makes comparison between the photocatalytically active samples and the control somewhat skewed. Regardless in the case of methylene blue stain mineralization the nanoparticle samples, particularly all the gold nanoparticle coated samples, showed an improved rate of stain mineralization compared to the TiO_2 only coating (Table 1). Furthermore, all samples performed dramatically better than the pristine / untreated cotton sample. Methylene blue is easier to mineralize than Congo red as stated above, so it is likely that

the photogenerated electrons from the gold nanoparticles (which would have less energy than those generated from the silver nanoparticles due to the gold nanoparticles' higher λ_{max} value) were able to play a significant role in the mineralization of the comparatively easy to mineralize methylene blue.

Sample	K	Avg
2 mM $AgTiO_2$	0.02054	.02556
1 mM $AgTiO_2$	0.02917	
0.5 mM $AgTiO_2$	0.02699	
2 mM $AuTiO_2$	0.01799	.02228
1 mM $AuTiO_2$	0.02476	
0.5 mM $AuTiO_2$	0.02411	
TiO_2 Only	0.02591	.02591
Virgin Cotton	0.00998	.00998

Table 1. Tabulated Kinetic Data for the Mineralization of Methylene Blue by the Various Types of Ag/Au-TiO_2 Coatings.

Staining with Congo red was also performed to evaluate the photocatalytic performance with a different, less easily mineralized stain (Figure 13). In general, the extinction of the Congo red stain was seen to proceed more slowly; the rate of Congo red removal on the pristine fabric sample was roughly half the rate of methylene blue removal on the untreated cotton fibers.

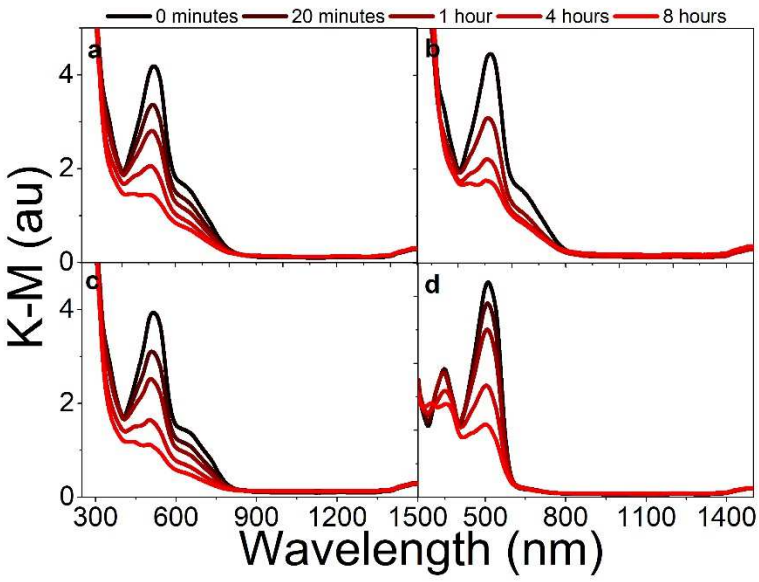

Figure 13. UV-Vis Spectra of the TiO_2 / Nanoparticle Coated Fiber Samples after Staining with Congo red, and upon Exposure to Simulated Solar Light: a) 1 mM Ag-TiO_2 Coated Fibers, b) 1 mM Au-TiO_2 Coated Fibers, c) TiO_2 Coated Fibers, and d) Pristine Cotton Fibers.

Increasing nanoparticle concentration had somewhat indeterminate effects on the rate of extinction in the case of the Au-TiO_2 coated sample, however it was seen to have some positive effect on the rate of extinction in the silver nanoparticle coated sample, with qualitatively less of the stain present after eight hours of simulated solar exposure in the 2 mM $AgNO_3$ coated sample compared to the 0.5 mM $AgNO_3$ coated sample (Figure 14). It should also be noted here that in the methylene blue extinction experiments data was collected out to six hours and complete stain extinction was observed, however in the case of Congo red even after eight hours some portion of the original stain still remains.

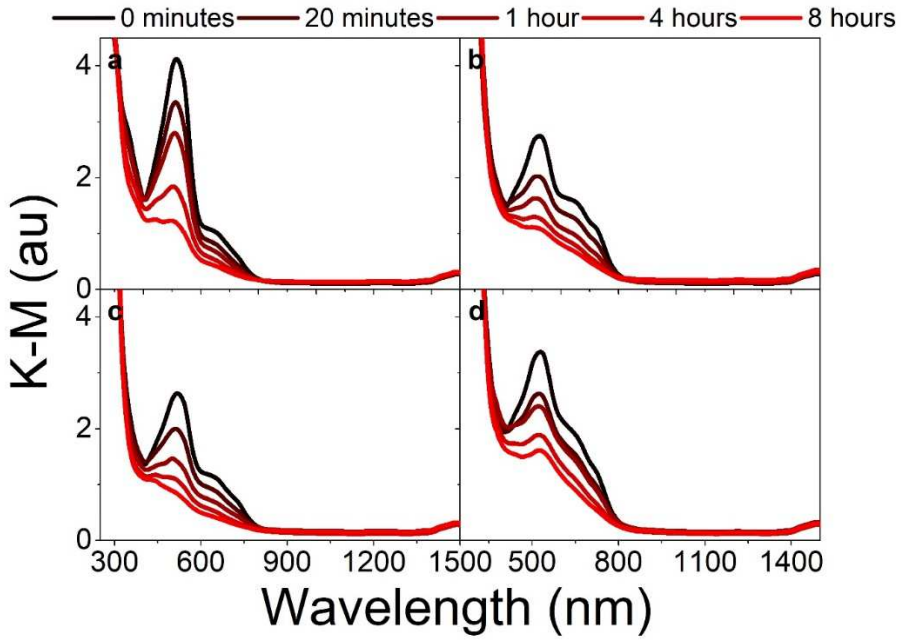

Figure 14. UV-Vis Spectra of the TiO_2 / Nanoparticle Coated Fiber Samples after Staining with Congo Red, and upon Exposure to Simulated Solar Light: a) 0.5 mM Ag-TiO_2 Coated Fibers, b) 0.5 mM 0.5 mM Au-TiO_2 Coated Fibers, c) 2.0 mM Ag-TiO_2 Coated Fibers, and d) 2.0 mM Au-TiO_2 Coated Fibers.

Fitting of the kinetic data was simplified versus the fitting in the case of methylene blue, as all of the evaluated samples showed much more linearity when plotted as first order kinetic data. It is apparent however that the benefits of the nanoparticle / TiO_2 coating over the untreated fabric were markedly less when stained with such a stable / difficult to mineralize dye (Figure 15). Qualitatively the gold nanoparticle coated sample showed superior performance compared to the silver nanoparticle coated sample. Congo red has its main absorption peak at 496 nm, however it also has two absorption peaks in the UV region at 236 nm and 338 nm [147]. Because of this, it is likely that some of the incident high-energy UV and near UV radiation was absorbed by the Congo red dye itself rather than interacting with the Ag/Au-TiO_2 layer, which decreased

the apparent efficiency of the coating. Organic compounds like Congo red which absorb high energy incident radiation are a good example of why Au / Ag nanoparticle-based sensitizers, or rather sensitizers in general, are important for photocatalytic applications; by increasing the effective absorption range of the photoactive layer, compounds which inherently absorb high-energy incident photons can still be quickly and efficiently degraded.

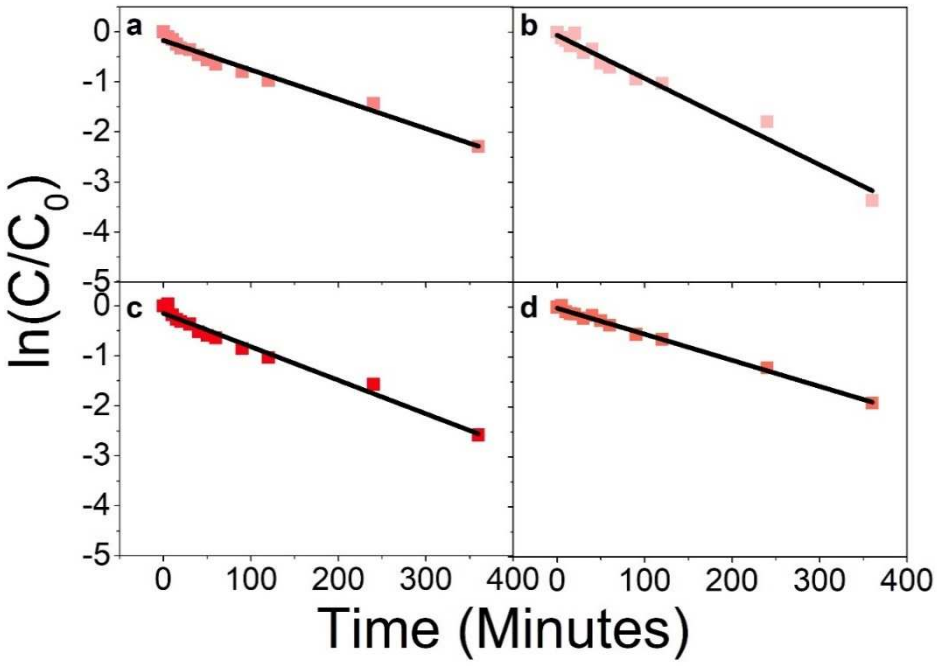

Figure 15. The Natural Log of The ratio of Congo Red Peak Area to Starting Peak Area Upon Repeated Exposure to Simulates Solar Light for the TiO_2 / Nanoparticle Coated Fiber Samples: a) 1mM $AgTiO_2$ Coated Fibers, b) 1 mM $AuTiO_2$ Coated Fibers, c) TiO_2 Coated Fibers, and d) Pristine Cotton Fibers.

Increasing the nanoparticle concentration had somewhat unclear effects with the Congo red, with the higher concentration of gold nanoparticles performing worse (Figure 16), however the gold nanoparticle coated samples did perform better than the silver nanoparticle coated

samples in general. The improved performance of the gold nanoparticle coated samples could be due to the overlap of the Congo red absorption maxima at 496 nm, 338 nm, and 236 nm with the silver nanoparticle absorption maximum at 440 nm. The gold absorption peak was at 547 nm however, which was far enough outside the absorption range of Congo red to not be interfered with. The improved performance of the gold nanoparticle coated sample strongly suggests that electron transfer is taking place between the gold nanoparticle and the TiO_2 coating, and that the gold nanoparticles are acting as photosensitizers.

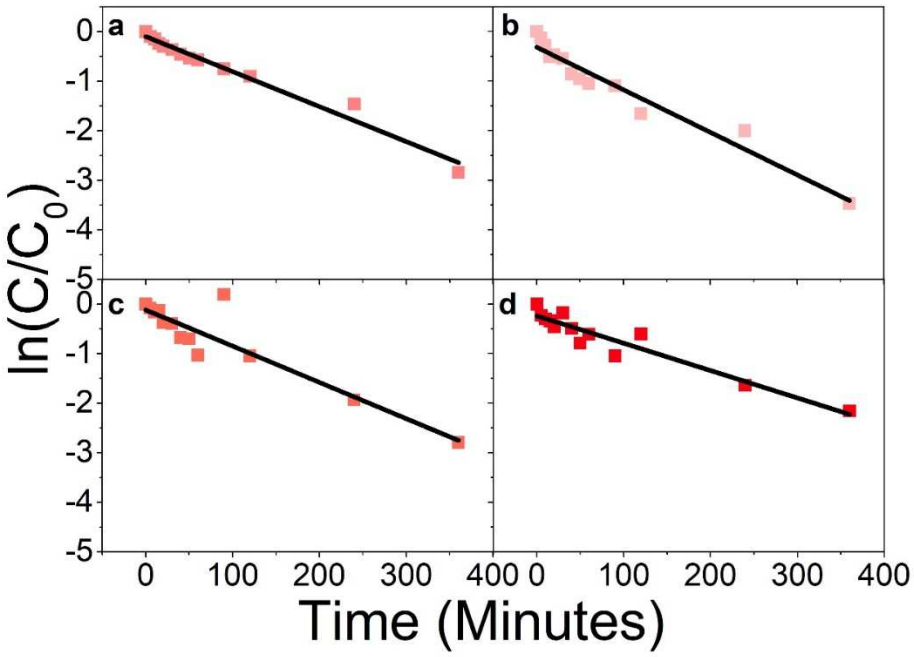

Figure 16. Natural Log of the Ratio of Congo Red Peak Area to Starting Peak Area Upon Repeated Exposure to Simulated Solar Light for the TiO_2 / Nanoparticle Coated Samples: a) 0.5 mM Ag-TiO_2 Coated Fibers, b) 0.5 mM Au-TiO_2 Coated Fibers, c) 2 mM Ag-TiO_2 Coated Fibers, and d) 2 mM Au-TiO_2 Coated Fibers.

Tabulation of the kinetic data for the Congo red staining reveals that on average the nanoparticle coated samples performed better than the TiO_2 only sample, and all samples performed better than the untreated sample. The 1 mM Au-TiO_2 coated sample performed the best out of the tested samples, which matches up with previous statements about gold nanoparticles being a good sensitizer when the organic stain itself absorbs a fair amount of the incident high-energy radiation that would usually be photocatalytically utilized by the TiO_2 layer.

Sample	K	Avg
2 mM $AgTiO_2$	0.00732	.00675
1 mM $AgTiO_2$	0.00588	
0.5 mM $AgTiO_2$	0.00706	
2 mM $AuTiO_2$	0.00552	.00758
1 mM $AuTiO_2$	0.00864	
0.5 mM $AuTiO_2$	0.00858	
TiO_2 Only	0.00670	.00670
Virgin Cotton	0.00523	.00523

Table 2. Tabulated Kinetic Data from the Congo Red Extinction Fitting.

Another important metric for evaluating the performance of the catalytic coating is stability over multiple staining events. If the gold or silver nanoparticles are truly stable when integrated into the TiO_2 coating the rate of stain removal should remain consistent over multiple cycles. It has been found in the literature that gold nanoparticles, particularly gold spheroid nanoparticles, are very resistant to photodegradation whereas gold rods and prisms are

vulnerable to degradation [148]. To determine the stability of the photocatalyst itself, multiple cycles of staining and stain extinction were conducted on the 1 mM Ag-TiO_2 coated sample with methylene blue dye, the raw results of which are presented in Figure 17.

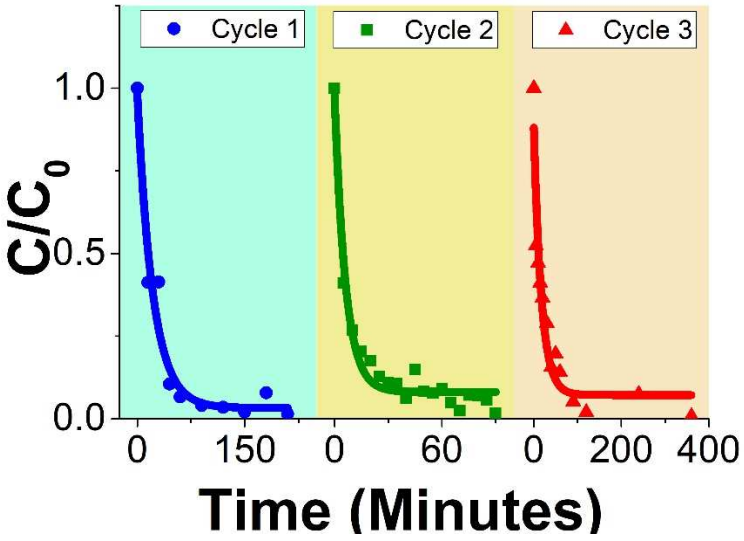

Figure 17. C/C_0 Data for the 1 mM Ag-TiO_2 Sample Over Repeated Cycles of Staining and Exposure to Simulated Solar Light. Note How Extinction Proceeds in the Same Way Each Time.

By examining the kinetic data from the results of Figure 17, we can see that the rate of stain extinction is nearly the same each time (Figure 18). Furthermore, it is important to note that the concentration of the stain on the surface of the fabric, at least within the range of concentrations tested (0.001 % w/v to 0.1 % w/v) had no effect on the rate of stain removal. It is likely that the produced photocatalyst would be able to handle very high levels of stain loading given the aggregated TiO_2 clusters which act to increase the surface area / area for the stain molecules to be adsorbed and mineralized.

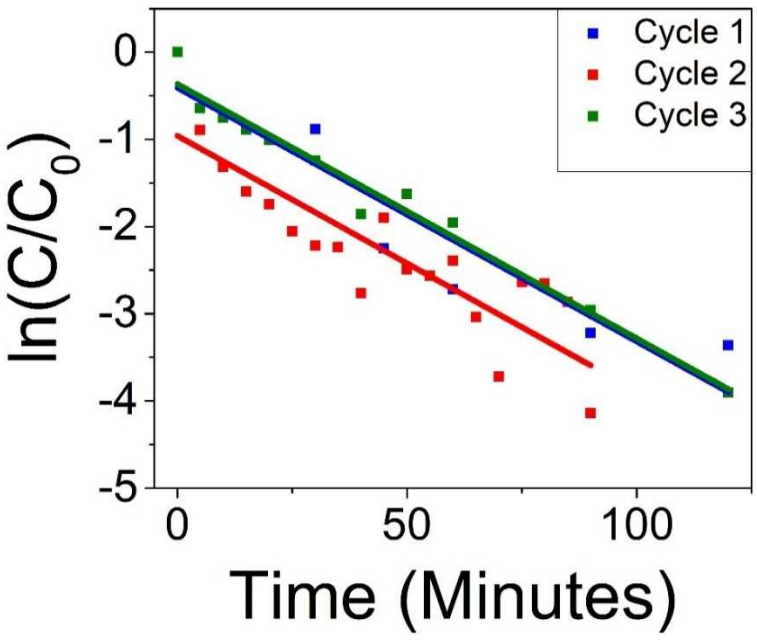

Figure 18. Performance of the 1 mM Ag-TiO_2 Coated Sample over Multiple Cycles of Staining and Exposure to Simulated Solar Light. Note that the Third Staining was Performed using a 0.1 % w/v Methylene Blue Solution, and the First Two Were with a 0.001% w/v Solution of Methylene Blue.

Apart from the stability of the photoactive layer, the stability of the underlying cellulose is also of concern. The cellulosic substrate is not innately immune to photodegradation, and indeed research into utilizing photoactive catalysts to degrade cellulose for use in biofuels or other biomaterial related applications is ongoing [149]. Cellulose, however, is an intrinsically robust biopolymer due to rigid long chains and intra-molecular coupling due to hydrogen bonding [150]. To verify that no photodegradation of the cellulosic backbone was taking place, FTIR spectra of the 1 mM Au-TiO_2 coated fiber sample were collected at regular intervals after exposure to simulated solar light, and it can be seen that the spectra are effectively unchanged (Figure 19).

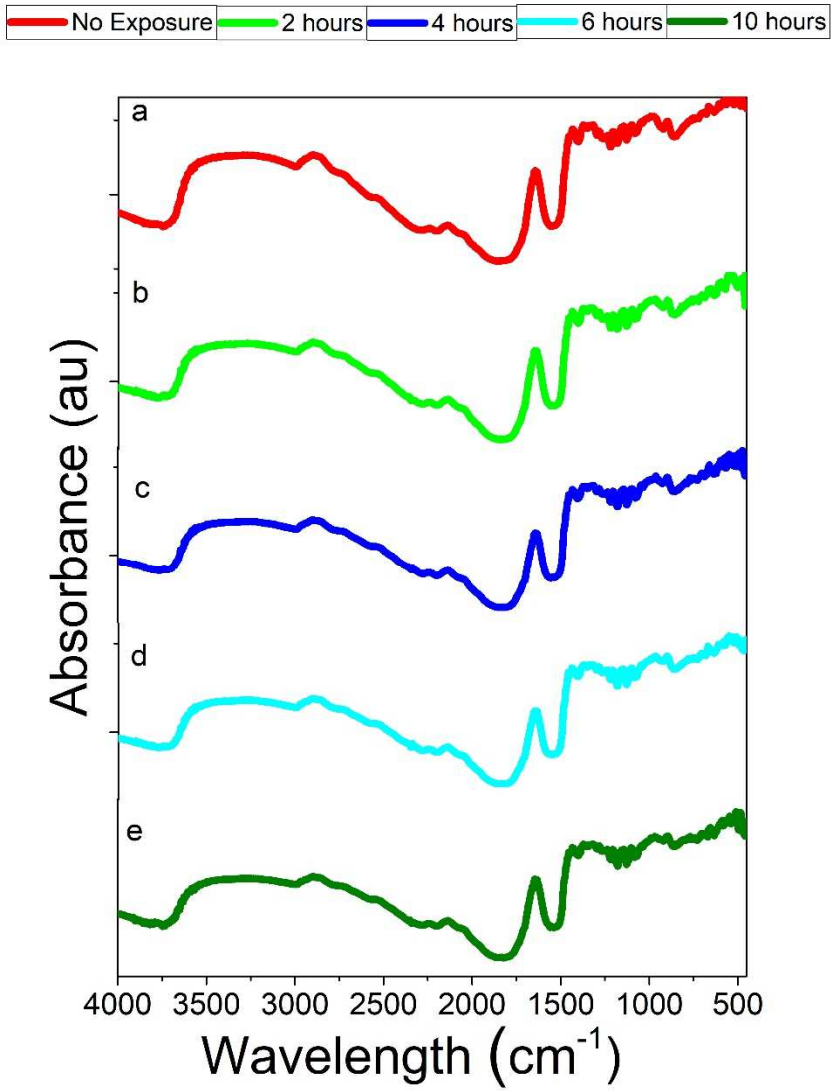

Figure 19. FTIR Spectra of the Au-TiO_2 Coated Fibers After Repeated Exposure to Simulated Solar Light for Exposure Times of: a) No Exposure, b) 2 Hours, c) Four Hours, d) Six Hours, and e) Ten Hours. The Spectra are Essentially Unchanged Indicating no Photodegradation.

Apart from verification that no photodegradation of the underlying cellulosic substrate was taking place, further insight into the structure of the functionalized cellulose can be gained by analyzing the FTIR spectra of the various sample types (Figure 20). While no difference was

noted between the Au-TiO_2, Ag-TiO_2, and TiO_2 coated samples, marked differences between the pristine / control sample and the other samples were noted. Characteristic peaks that ban be observed include a broad O-H stretching band at 3378 cm^{-1}, a C-H stretching bad at 2900 cm^{-1}, and the H-O-H bending band at 1650 cm^{-1} [151]. The H-O-H bending band is observed to be more intense in the Au-TiO_2 coated sample, although this could be due to the somewhat hydrophobic nature of the potassium bromide (KBr) used to prepare the samples for FTIR analysis, or just simply more water present in the Au-TiO_2 sample as a result of the synthetic technique. The TiO_2 band is expected to appear at ~700 cm^{-1}, and indeed the Au-TiO_2 absorption spectra lack the "dip" observed in the spectra of pristine cotton near 700 cm^{-1}, which suggests that the TiO_2 while not immediately visible is indeed present as a relatively broad peak [152]. Reduction of the intensity of the C-H stretching band at 2900 cm^{-1} was also observed. Overall, the consistency of the FTIR spectra suggest that the coated material possesses long-term photostability.

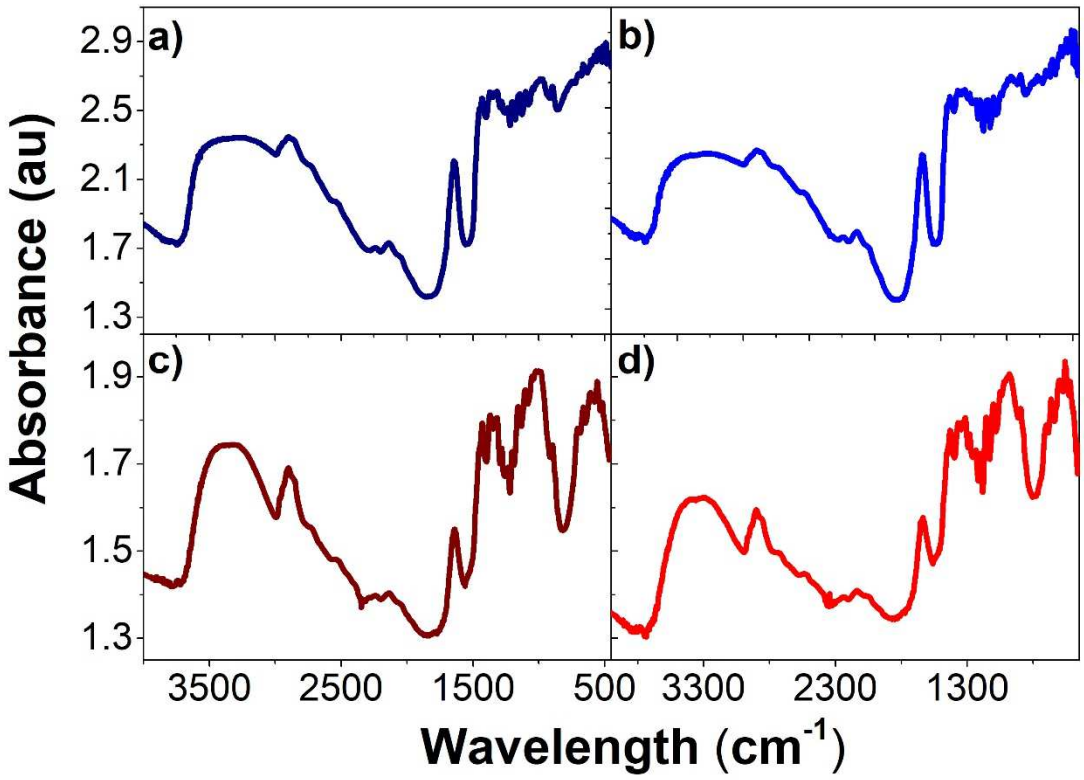

Figure 20. FTIR Spectra After Repeated Exposure to Simulated Solar Light for: a) Au-TiO_2 Fibers with no Exposure, b) Au-TiO_2 Fibers After Ten Hours of Exposure, c) Pristine Fibers With no Exposure, and d) Pristine Fibers After Ten Hours of UV Exposure.

Finally, the antimicrobial properties of the produced Au/Ag-TiO_2 fabric samples were evaluated using the Kirby-Bauer disk diffusion method (Figure 21). The nanoparticle coated fiber samples were expected to show antimicrobial properties via the same mechanisms that grant them self-cleaning properties, and indeed the Ag/Au-TiO_2 coated fibers demonstrated antimicrobial activity as evidenced by the zone of inhibition around the fabric samples after inoculation and incubation of the plates. It's also worth noting that the relative size of the zone of exclusion was about equivalent for the Au-TiO_2 and Ag-TiO_2 coated samples. It was expected

that the zone of inhibition would be present in the case of the silver nanoparticle coated sample, as silver nanoparticles have seen wide spread utilization as antimicrobial agents [153], however the apparent high activity of the gold nanoparticle coated sample was somewhat unexpected. Gold nanoparticles have prompted a great deal of recent research into their antimicrobial properties [154,155], and it appears that they do indeed have marked antibacterial properties when deployed on a TiO_2-based thin film. The TiO_2 and pristine cotton fiber samples exhibited little to no bacterial inhibition, which is notable as some limited degree of bactericidal activity would be expected simply from the oxidizing potential generated by the TiO_2 layer. While the zone of exclusion was absent in the case of the plain TiO_2 coating, it is likely that bacteria located directly on the illuminated fiber sample would be quickly destroyed, as *E. Coli, Staphylococcus aureus, and Pseudomonas aeruginosa* have all been experimentally observed to be killed rapidly on illuminated TiO_2 surfaces [156]. Furthermore, the toxic compounds produced by the bacteria are themselves decomposed by the catalytic action of TiO_2 [157].

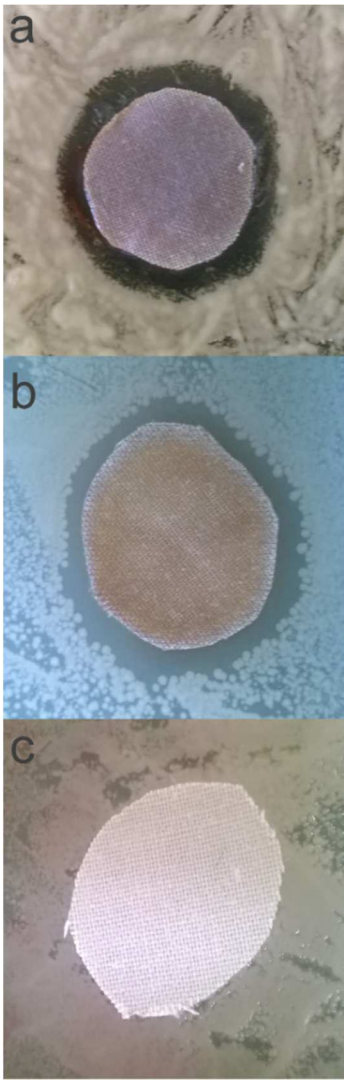

Figure 21. Results of the Kirby-Baur Disk Diffusion Test with the Exclusion Zones around the Fibers Clearly Visible for: a) Au-TiO_2 Coated Cotton Fibers, b) Ag-TiO_2 Coated Fibers, and c) Pristine Cotton Fibers.

Apart from the bactericidal mechanisms suggested in the introduction, direct free radical generation and reaction has also been proposed as a key bactericidal mechanism for silver nanoparticles [158]. The reaction between nanoparticles and the membrane structures of both gram positive and gram negative bacteria are not completely understood, however the formation of "pits" in the outer membranes has been observed due to the presence of silver nanoparticles,

leading to increased membrane and ultimately cell death [158]. However despite these observations there remains a strong argument for free radical generation being the principle causal mechanism behind the bactericidal effects, as the inclusion of an antioxidant in one study was found to eliminate the anti-microbial activity of silver nanoparticles [158]. Furthermore it has been suggested that the evolution of silver ions produced from the silver nanoparticles via their oxidation by the holes produced on the TiO_2 layer may be another mechanism by which the hybrid TiO_2 / Ag nanoparticle interface exhibits antimicrobial activity, as a similar mechanism has been experimentally observed with TiO_2 / copper hybrid surfaces [159]. Our results suggest that some combination of the above outlined mechanisms is responsible for enhancing the antibacterial activity of the nanoparticle coated fiber samples, and further elucidation of the mechanism could be had by testing the antimicrobial activity in the presence of an antioxidant. Fine tuning of the nanoparticle surface chemistry could further improve the anti-bacterial properties of the Ag/Au-TiO_2 coated fibers, and lend them increased activity against particularly hazardous bacteria [154].

Flexible Dye-Sensitized Solar Cells

It has been demonstrated that the TiO_2 coating was successfully deposited on the cellulose fibers, and that the coating was thin and homogenous and successfully functionalized with Au/Ag-TiO_2 nanoparticles. As mentioned above, this type of coating procedure also has applications for dye sensitized solar cells, as the coating process generates a nanostructured layer ideal for the impregnation of dye molecules / other sensitizers for the fabrication of high efficiency solar cells. Fabrication of cells of this type on carbon nanotube yarn was performed

and the characteristics of the cells were suboptimal for a variety of reasons. The lessons learned from the fabrication of these hybrid dye-sensitized solar cells were used to fabricate organic / polymer-based hybrid cells (reported later).

Previous work on carbon nanotube based dye sensitized solar cells by Uddin et al. has demonstrated that the incorporation of additional sensitizers (CdS / CdSe) has the potential to increase the PCE of the traditional dye sensitized solar cell architecture markedly, up to 7.39% [89]. Further work by Grissom et al. indicates that the deposition of a PCBM / P3HT layer can increase cell PCE further to ~7.6%. This study aimed to further improve cell efficiency with the use of low molecular weight P3HT to allow better penetration of the polymer layer into the mesoporous TiO_2 layer, and attempted to test whether doping of the TiO_2 layer with graphene could effectively act as a blocking layer [160] to prevent back recombination / enhance overall cell efficiency. While the maximum obtained cell efficiency was low (~2% PCE), valuable information about the kinetic properties of this type of hybrid cell architecture was obtained. The fabrication methodology used for the preparation of the DSSC based hybrid cells was as follows:

All solvents and acids were purchased from Sigma Aldrich. All precursors were purchased from Sigma Aldrich. Carbon nanotube yarn purchased from Nanocomp Incorporated was thermally treated at 300 C under light air flow for two hours to degrade the polymer coating that it was supplied with. Yarn was then sonicated sequentially in acetone, water, and isopropanol. The yarn was then placed in a stirred solution of 10% w/v HNO_3 in distilled water for twelve hours, washed sequentially with acetone, water, isopropanol, and sonicated in water. The yarn was then rinsed with ethanol and allowed to dry.

The working electrode of the cells was assembled by twisting together of six individual carbon nanotube yarns, granting the final raw working electrode an outer diameter of ~ 75 μm. The solution for the deposition of the nanoporous TiO_2 layer was then prepared as follows: to 50 ml isopropanol 5.92 ml (0.02 mol) titanium isopropoxide was added under vigorous stirring. 1.39 ml (0.01 mol) triethylamine was then added to this solution to act as a stabilizer. In a separate beaker, 50 ml isopropanol, 3.0 ml concentrated hydrochloric acid, and 0.72 ml distilled water were added sequentially under vigorous stirring. The HCl containing solution was then slowly added to the titanium isopropoxide containing solution under vigorous stirring and allowed to stir for a period of thirty minutes. The carbon nanotube yarn working electrodes were immersed in this solution for a period of thirty seconds, removed and calcined at 70 °C for five minutes and then at 95 °C.

The mesoporous TiO_2 layer (that provides a thick porous substrate for dye adsorption) was prepared as follows: 15 ml deionized water, 1 ml glacial acetic acid, three drops of triethylamine, and 5.921 ml titanium isopropoxide were sequentially mixed under vigorous stirring. A second solution containing 15 mL deionized water and 0.25 ml of 70 % nitric acid was prepared, and both solutions were stirred separately for a period of five minutes. The HNO_3 containing solution was slowly added to the isopropoxide containing solution and the mixture was stirred for an additional five minutes. The mixture was then placed in a Teflon-lined autoclavable pressure vessel and heated at 240 C for a period of twelve hours. Once removed from the pressure vessel 2.6 grams of polyethylene glycol (20,000 g/mol) was added and half of the total solution volume was boiled off while the polyethylene glycol dissolved. For the samples that had graphene incorporated into the TiO_2 layer, graphene was added to this mixture at a rate of 1.0 wt % to the final weight of the TiO_2 (16 mg for this procedure). This mixture was dip

coated onto the nanoporous TiO_2 coated carbon nanotube yarn working electrodes, followed by calcination at 350 C for a period off five minutes. This dip coating and annealing process was repeated four times. In hindsight it is likely that a final high-temperature or longer-term annealing here would have been appropriate to remove any last trace of the polyethylene glycol that may still be adsorbed in or on the porous TiO_2 layer. Incomplete thermal evaporation / mineralization of the polyethylene glycol here could leave residue on the porous TiO_2 layer which would impair cell performance.

The thus deposited microporous TiO_2 layer was annealed to ensure homogeneity / good interfacial contact between the nanoporous and microporous coatings as follows: A solution of 0.05 M $TiCl_4$ in ethanol was prepared and the electrodes were submerged in this solution for twelve hours. A final annealing of this layer at 300 C for a period of thirty minutes was performed.

Both separate synthesis followed by deposition and direct growth of the cadmium sulfide / cadmium selenide quantum dot sensitizers was evaluated, and it was determined that in the case of these cells the direct growth method produced superior results, likely due to the inherent difficulty with incorporating already fully formed / insoluble quantum dots into the porous TiO_2 layer via simple dip coating. Furthermore, more aggressive incorporation techniques such as sonication run the risk of disrupting the morphology of the oxide layer or destroying it all together. However, for the later reported batch of organic polymer / hybrid cells separate synthesis and direct deposition onto the working electrode surface was performed. It should be noted that, as was the case with the gold and silver nanoparticles grown directly on the surface of the TiO_2 layer in the above work, such a process produces a larger range of nanoparticle sizes and is less optimizable than fully solution-based synthetic techniques.

Cadmium sulfide and cadmium selenide direct growth was carried out as follows: 50 mL of 0.3 M cadmium nitrate in ethanol was prepared and stirred, and 50 mL of 0.3 M sodium sulfide in ethanol was prepared and stirred. The TiO_2 coated working electrode was immersed in the $CdNO_3$ containing solution for five minutes, followed by immersion in the Na_2S solution for five minutes, and then was allowed to dry overnight. For the deposition of cadmium selenide, sodium selenium sulfate was prepared by heating of 0.3 M sodium selenite mixed with 0.3 M sodium sulfate in water for a period of eight hours at 70 C. A separate solution of 0.3 M $Cd(NO_3)_2$ in ethanol was prepared, and the electrodes were dipped in this solution for five minutes, rinsed with ethanol for one minutes, and then heated in the sodium selenium sulfate solution for one hour at 50 °C.

Ideally the dye should have been deposited at this step rather than post P3HT / PCBM deposition, however the stability / insolubility of the dye in the solvents used for P3HT / PCBM deposition is questionable. If the dye were deposited prior to the deposition of the P3HT / PCBM it would be more incorporated into the mesoporous TiO_2 structure, however solubilization by the chloroform / chlorobenzene used for the polymer deposition it would impair cell efficiency dramatically. This inability to deposit the dye prior to the deposition of the polymers (or even prior to the deposition of the CdS / CdSe quantum dots) is a major limitation holding back this type of hybrid DSSC / polymeric cell architecture. However deposition of N719 after the P3HT / PCBM depositions is likely acceptable as P3HT / PCBM have minimal solubility in highly polar solvents like acetonitrile and tert-butanol [130].

The deposition of the P3HT / PCBM / N719 was carried out as follows: solutions of 5 mg/ml of P3HT in chloroform and 5 mg/ml of PCBM in chlorobenzene were prepared separately and then mixed in a 1:1 ratio. The prepared working electrodes were immersed in this solution

for a period off twelve hours. Finally a solution of 0.003 % by weight of N719 in a 1:1 mixture of tert-butanol : acetonitrile was prepared, and the electrodes were immersed and allowed to soak for 24 hours.

Preparation of the carbon nanotube yarn for the counter electrode was carried out using the same above-listed polymer removal and washing steps, followed by platinization of the yarn via sputtering with a platinum target at 1.5 kV and 5 mA for a period of 60 seconds. In order to coat the yarn as evenly as possible it was then flipped and sputtered using the same parameters on the opposite side of the yarn. Cell assembly was then performed by wrapping the counter electrode around the working electrode at a pitch of ~ 15°.

The thus assembled cells were then saturated with electrolyte by immersing them in the electrolyte solution for 2-3 seconds. The electrolyte was prepared as follows: .669 grams LiI, .1269 grams I_2, and .624 ml of tert-butyl pyridine were mixed and brought up to 10 ml total volume in 3-methoxy propionitrile, then 0.5 grams of poly(vinylidene fluoride-co-hexafluoropropene) was added and the mixture was stirred and heated to dissolve all of the electrolyte components.

Overall, six batches of cells were synthesized: containing graphene and P3HT purchased from Sigma Aldrich, containing no graphene and P3HT purchased from Sigma Aldrich, containing graphene and batch A of a low molecular weight P3HT sample, containing no graphene and batch A of a low molecular weight P3HT sample, containing graphene and batch B of a low molecular weight P3HT sample, and containing no graphene and batch B of a low molecular weight P3HT sample. Five to six samples were ultimately prepared for each of the

above stated batches, with six per batch being the initial number but various issues during the lengthy cell preparation process led to the destruction of some of the cells.

Of the steps involved in the preparation of these cells, there are a few that likely dramatically impair fabrication yield (the ratio of the number of working cells to the number of non-functional cells). The dip coating process that involved the suspension of microporous TiO_2 clusters in an aqueous, polyethylene glycol containing solution is very liable to generate uneven coatings especially when performed by hand. This is further complicated by the fact that the cells are composed of several twisted individual yarns which lend the cells a somewhat uneven surface profile to which the coating is applied. Due to the viscosity of the coating polyethylene glycol containing solution it is likely that the depth of the coating generated in the "valleys" between the individual carbon nanotube yarns is greater than the thickness of the coating generated on the "hills". This high viscosity also makes analysis via the dip-coating equations presented above difficult, and makes evaluating layer thickness a process of trial and error. Furthermore, during annealing / the burning off of the ethylene glycol and water that was in solution with the porous TiO_2, a thicker coating is generated on the bottom side of the cell than on the top. In summary, depositing a uniform TiO_2 layer from a suspension of TiO_2 in water / polyethylene glycol on an irregularly shaped cylindrical electrode is difficult and likely acts as a major bottleneck to cell efficiency, as if the solid TiO_2 layer is more than 20 nm thick electron injection through the oxide layer will be significantly impaired as will overall cell efficiency [89].

A second major limiting factor with this type of cell architecture is the electrolyte. A great deal of research has gone into developing solid phase electrolytes for the reasons discussed above [107,161–163], and for such an electrolyte to generate high PCE it must be non-viscous

enough to penetrate the microporous TiO_2 structure. However, for it to be solid state / stable without additional sealing of the cell being required, it must be viscous enough or completely in the solid state so that it won't evaporate. Furthermore, for commercial applications the electrolyte, if at all in the liquid state, must remain unfrozen to low enough temperatures to allow for cell deployment in climates where cold external temperatures are common. High temperature stability is also a problem; the electrolyte used in these cells, while indeed being "semi" solid state, evaporates quite quickly under the intense heat of the solar simulator and this during characterization continually rewetting of the cells is required to obtain peak efficiency. While this problem could be overcome with additional sealing of the cell that is a difficult proposition in cell architectures that are designed to be flexible.

The electrolyte used for this type of cell architecture has another unfortunate effect that applies only to in-lab characterization but, in cells deployed for power-generation in the field, likely wouldn't be an issue at all. That is that the semi-solid-state electrolyte relies on diffusion of the reduced / oxidized species to the dye / counter electrode respectively, and this diffusion is a process that occurs on the order of seconds (Figure 22) rather than almost instantaneously as is the case in silicon cells / cells built on crystalline materials. This effect makes characterization of the cell's incident photon-to-electron conversion efficiency (IPCE) impossible using traditional instruments as they rely on a monochromatic light source that is rapidly switched on and off via a chopper at a frequency of 10-60 hertz. A lock in current amplifier is then employed to amplify / measure cell current that is detected fluctuating at the same frequency as the light source. This allows for continual blanking as many wavelengths of the incident light are scanned through. However, because of the liquid electrolyte and the slow cell response time such characterization would require that the frequency be decreased to ~ 1/120 Hz to allow stabilization of the cell

output at the incident wavelength. This would make a typical scan from 250-1100 nm at the standard 1 nm resolution take 28 hours which, practical considerations aside, is further ruled out due to the unstable nature of the unsealed electrolyte over long periods of time. Given the importance of IPCE as a characterization technique for this type of cell, especially with the utilization of multiple sensitizers, to gauge the effectiveness of the cell over a range of wavelengths to determine which sensitizers are having a positive effect on overall cell efficiency, the lack of this characterization technique effectively restricts the further optimization of this type of cell architecture.

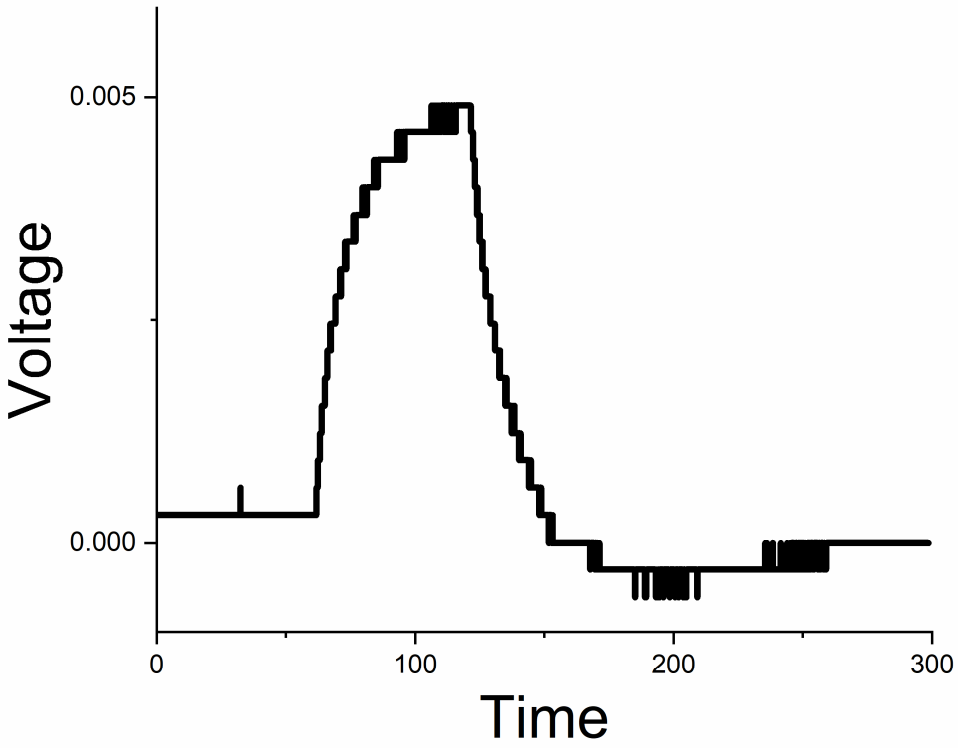

Figure 22. Cell Kinetics of a DSSC With Semi-Solid-State Electrolyte. Illumination of One Sun (AM 1.5) was Switched on at 60 Seconds, and off at 120 Seconds.

For the electrical characterization cyclic voltammetry was performed using a Princeton Applied Research VersaSTAT 3 with a scan rate 0.1 V/s and variable lower and upper bounding voltages. Illumination of the cells was performed with a Honle UVA-Cube 400 under one sun intensity of AM 1.5 solar spectrum irradiation. The cells were characterized at their full operational length (~6 cm) and then cut down in 0.5 cm increments and characterized until the cells were destroyed.

The synthesis of the flexible DSSC-based hybrid architecture cells was also carried out to determine the applicability of graphene to this type of cell. The presence of contradictory information in the literature stating both graphene's effectiveness at preventing recombination [160,164] as having a positive effect on overall cell efficiency, and stating that the introduction of crystallographic defects provides more sites for charge recombination and reduced overall cell efficiency [89] was a key issue this work aimed to resolve. Of the cells utilizing P3HT purchased from Sigma Aldrich, graphene was observed to lower the average maximum (the average of the maximum efficiencies obtained from each cell) from 0.57 % to 0.47 % PCE, of the cells utilizing batch A low molecular weight P3HT, the average maximum efficiency was lowered from 0.44 % to 0.36 % PCE with the inclusion of graphene, and of the cells utilizing a separate batch of low molecular weight P3HT the average maximum efficiency was lowered from 0.97 % to 0.43 % PCE. So, it is obvious from these results that the inclusion of graphene has a markedly negative impact on the obtained cell efficiencies.

The other experimental parameter that was being tested with this batch of hybrid DSSC architecture cells was whether the inclusion of low molecular P3HT could improve cell performance, which is reasonable as lower molecular weight P3HT would be more able to penetrate the porous TiO_2 electrode and would theoretically make better contact with the CdS /

CdSe / dye molecules to better facilitate charge separation. It is clear from the results that batch B of the low molecular weight P3HT produced significantly higher conversion efficiencies than either the P3HT purchased from Sigma Aldrich (MW: 54,000 – 75,000 g/mol), and a cell made from batch B of the low molecular weight P3HT obtained the highest efficiency of this study with 1.83 %. Again, because of the lack of IPCE data, indeed the inability to obtain IPCE data, further optimization of this particular cell architecture is complicated, as it is unclear which of the sensitizers is contributing the most to the observed efficiency of the cells.

Despite the low overall efficiency of these cells, another interesting set of data obtained from these was the observed efficiency of the cells when back-illuminated by placing a mirror underneath them (Figure 23). Reflectors are a popular area of research due to their potential to increase the efficiency of solar cells by allowing for the harvesting of light that would otherwise be wasted due to either cell geometry or semi-transparency [165–167]. The ability to take advantage of reflected light is another property enhanced in the case of three-dimensionally structured cells and the data indicated that an additional 30% improvement in IPCE is obtained if a reflector is placed behind the cell, allowing light entering the immediate area of the cell to be reflected up and harvested by the areas of the cell that are usually in the shadow produced by the top half of the cell. This improvement in IPCE suggests that properly designed reflectors could dramatically increase the performance of three dimensionally structured fiber-type cells woven together in a breathable mesh-like configuration, by allowing the light entering through the gaps between the cells to be reflected and effectively harvested by the areas of the fiber-type cells that are not exposed to direct illumination.

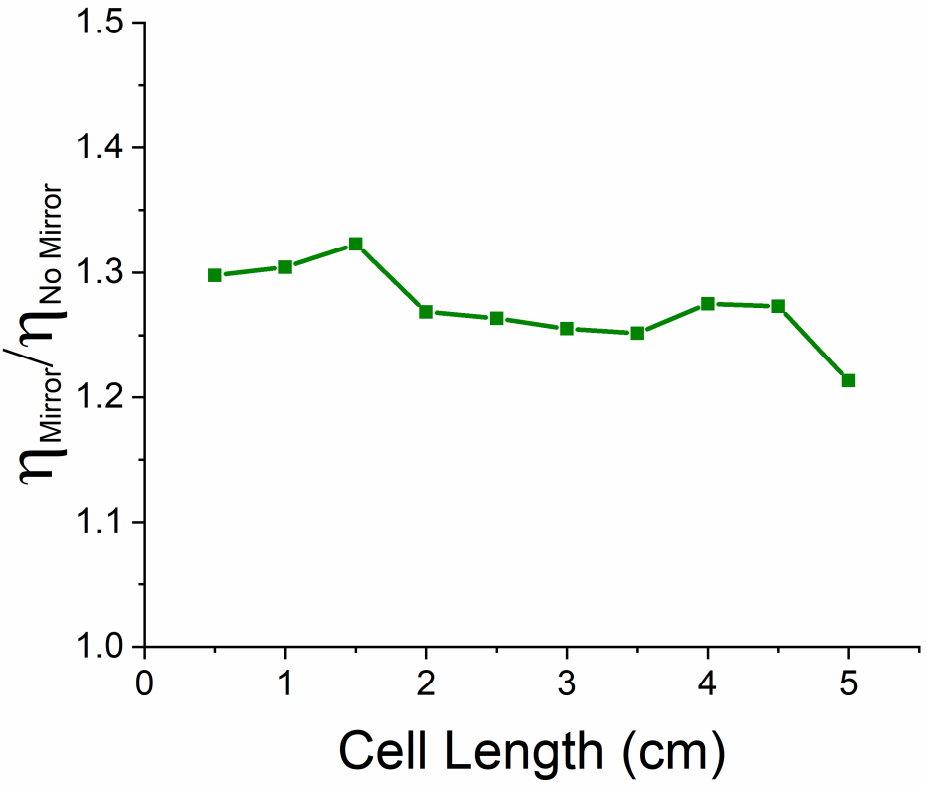

Figure 23. Ratio Between Overall Power Conversion Efficiency (PCE) with and without Back Reflectance of a DSSC / Hybrid Type Cell at Varying Cell Lengths.

Organic / Polymer Based Hybrid Solar Cells

The final experiment carried out as part of this work was the fabrication of the hybrid / polymer based solar cells. The synthetic technique used to produce these cells was as follows: the carbon nanofiber yarn purchased from Nanocomp Inc (OD ~ 25 μm) was thermally treated at 240 °C for four hours to remove the polymer coating, washed with water, acetone, and isopropanol, treated in a 10 % by nitric acid solution for a period of twelve hours under vigorous stirring, then washed with water, acetone, and isopropanol once more. SEM was carried out on

the raw, untreated yarn before and after the polymer-removal treatment to verify that the coating had been successfully removed.

The TmPyPB electron transport layer dip coating solution was prepared from 10 mL of chlorobenzene and 8.22 mg of TmPyPB (both purchased from Sigma Aldrich), and the six carbon nanotube yarn twisted working electrodes were immersed in this solution, allowed to become saturated with the solution for a minute, and then withdrawn from the dip coating solution at a rate of 1 cm s^{-1}. The PCBM layer dip coating solution was prepared from 10 mL of chlorobenzene and 37 mg of PCBM purchased from Sigma Aldrich, the TmPyPB coated electrodes were immersed in this solution and likewise withdrawn at a rate of 1 cm s^{-1}. The bulk heterojunction layer dip coating solution was prepared by dissolving 63.7 mg of P3HT in 5 mL of chloroform (both purchased from Sigma Aldrich), and 63.7 mg of PCBM in 5 mL of chlorobenzene. These solutions were then mixed to generate the dip bulk heterojunction layer dip coating solution, and the TmPYPB / PCBM coated cells were immersed in this solution and withdrawn at a rate of 1 cm s^{-1}. To generate the appropriate layer thickness of the bulk heterojunction layer (~200 nm), the dip coating process was repeated three times (for a total of four times). Finally the platinized counter electrode was wound around these cells, the PEDOT:PSS (Sigma Aldrich) dip coating solution was prepared from 80 mg of PEDOT:PSS dissolved in 10 mL of water, and the counter electrode wound cells were immersed in this solution and withdrawn at a rate of 1 cm s^{-1}.

Qualitatively, the deposition of the P3HT / PCBM layer over multiple dipping cycles appeared to be impaired by the previous layers of P3HT / PCBM that had been deposited; the successive dip coatings after the initial one did not appear to deposit the same thickness of bulk heterojunction layer as the initial coating when prepared on FTO glass as analog cells for IPCE

analysis. Furthermore, the layer thickness appeared to be constant after ~4 dip coating cycles into P3HT / PCBM in 1:1 DCM / chlorobenzene, and remained unchanged with up to 8 total dipping cycles. A nanoporous TiO_2 coating was applied to attempt to increase surface roughness / porosity to allow the growth of the bulk heterojunction layer to proceed more uniformly, and this appeared to increase the observed layer thickness of P3HT / PCBM. It is probable that over the course of dip coating steps that occur after the initial couple of cycles, a similar amount of the P3HT / PCBM layer is solubilized into the bulk dip-coating precursor solution as it deposited by the evaporating solution that remains on the substrate after it is withdrawn. This issue could likely be remedied to some degree by utilizing either spin coating (a technique that requires less solution and presents less of an opportunity for solubilization), providing a nanostructured scaffold so that the dip coating can be carried out in a single or couple steps and can generate a layer of appropriate thickness, or by utilizing a well-mixed super-saturated colloidal suspension of PCBM / P3HT at the above stated concentration for single-dip coating to be successful (509.8 mg to 10 mL 1:1 DCM / chlorobenzene). A representative *I / V* curve of the totally polymer-based cells obtained up to this point is presented below as Figure 24.

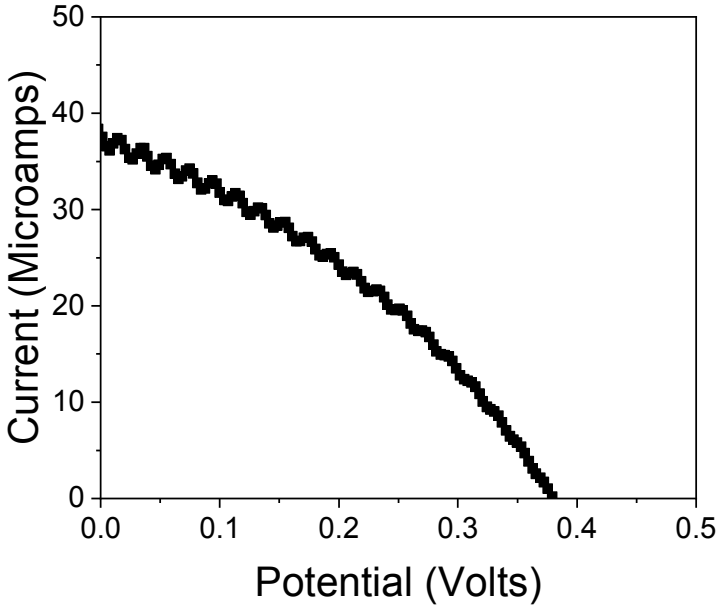

Figure 24. Representative *I / V* Curve for the PCBM / P3HT Hybrid Cell Architecture.

Furthermore, the kinetics of these polymer-type cells with a PEDOT / PSS based electrolyte were observed to be much more rapid compared to the DSSC type cell architecture cells with an iodine based redox couplet electrolyte, which means that they are well-suited to IPCE analysis and further optimization. Another issue was that the PEDOT / PSS electrolyte was highly conductive which led to the carbon nanotube-based cells being very prone to shorting out due to imperfections in the applied polymer coating. This issue was likely compounded by the fact that the working electrode design was initially kept the same as it was for the DSSC / hybrid type cells (six carbon nanotube yarns twisted around each other), leading to many potential sites of slight surface imperfections at the points where the individual carbon nanotube yarns came into contact with one another. This issue was resolved in the case of the DSSC / hybrid type cells via the inclusion of a microporous / relatively thick layer of TiO_2, however for the polymer type cells this layer was not included. In subsequent experiments a nanoporous TiO_2 layer was

included as the first layer for the carbon nanotube-based cells which led to the above referenced *I / V* curve (Figure 24), however the fabrication yield was still remarkably low for the previously stated reasons.

CHAPTER IV

SUMMARY AND CONCLUSIONS

Fiber-type devices have the potential to open up an entirely new market of consumer electronics; one composed of flexible textiles with integrated self-cleaning capabilities and on-board power generation to meet the demands of the next generation of flexible, portable electronic devices. Herein the self-cleaning ability of an Ag / Au nanoparticle augmented TiO_2 textile coating deposited via a simple solution-based process was evaluated, and it was found that the photocatalytic activity of the coating was considerably enhanced via the incorporation of Ag / Au nanoparticles. The anti-microbial activity of this hybrid coating material was confirmed, and the long-term stability of the coating and the underlying cellulose was examined via FTIR and both were observed to be stable over multiple staining / detaining cycles.

Solar cells based on carbon nanotube yarn have great potential to be incorporated into textile materials to provide power generation while themselves being flexible. A more traditional DSSC / hybrid type solar cell architecture was prepared and evaluated, and it was found that the microporous TiO_2 coating impaired the overall flexibility of the cells by introducing a relatively thick crystalline element into the cell architecture. Furthermore, the redox-based iodine couplet electrolyte has a couple innate disadvantages, namely it being only “semi-solid state” under

normal atmospheric conditions, and it being reliant on a diffusion-limited process for charge transfer. However, these cells produced acceptable results given their limitations.

Entirely polymer / hybrid type solar cell architectures are much more appropriate for preparation of a flexible carbon-nanotube based substrate, as most or all of the cell components are amorphous and thus flexible. Polymer-type solar cells composed of P3HT / PCBM with TmPyPB and a PEDOT / PSS based electrolyte were prepared and evaluated, however a couple of complications, namely the extreme conductivity of PEDOT / PSS and the difficulties associated with depositing a sufficiently thick P3HT / PCBM layer via successive dip coating cycles have led to a low fabrication yield up to this point. Further work towards incorporating CdS / CdSe layered sensitizers into the P3HT / PCBM bulk heterojunction layer in completely polymer-based solid-state cells based on carbon nanotube yarn could potentially open up a new field of polymer / nanoparticle hybrid type cell architectures.

More broadly, with further tweaking of the synthetic process, and the continual development of novel / cheaper polymers that lend themselves well to incorporation in polymer-type solar cells, it is very likely that cheap, roll-to-roll manufacturing of entirely polymer and / or hybrid-polymer type solar cells based on either carbon nanotubes or another flexible substrate will become commercially viable / substantially competitive with more traditional silicon based crystalline / DSSC type cell architectures in the coming years. The development of flexible, photoactive materials will continue to be an important area of research to meet consumer demand for novel, wearable electronic devices.

REFERENCES

[1] W.A. Hermann, Quantifying global exergy resources, Energy. 31 (2006) 1685–1702. doi:10.1016/j.energy.2005.09.006.

[2] Technology Roadmap - Solar Photovoltaic Energy 2014, IEA Webstore. (n.d.). https://webstore.iea.org/technology-roadmap-solar-photovoltaic-energy-2014 (accessed May 2, 2018).

[3] C.A. Gueymard, The sun's total and spectral irradiance for solar energy applications and solar radiation models, Solar Energy. 76 (2004) 423–453. doi:10.1016/j.solener.2003.08.039.

[4] C. Starr, C.A. Evers, L. Starr, Biology: Concepts and Applications, Thomson, Brooks/Cole, 2006.

[5] A. Fujishima, K. Honda, Electrochemical Photolysis of Water at a Semiconductor Electrode, Nature. 238 (1972) 37–38. doi:10.1038/238037a0.

[6] Y. Tamaki, A. Furube, M. Murai, K. Hara, R. Katoh, M. Tachiya, Dynamics of efficient electron–hole separation in TiO2 nanoparticles revealed by femtosecond transient absorption spectroscopy under the weak-excitation condition, Phys. Chem. Chem. Phys. 9 (2007) 1453–1460. doi:10.1039/B617552J.

[7] A. Fujishima, X. Zhang, D.A. Tryk, TiO2 photocatalysis and related surface phenomena, Surface Science Reports. 63 (2008) 515–582. doi:10.1016/j.surfrep.2008.10.001.

[8] X. Hu, H. Ji, L. Wu, Singlet oxygen photogeneration and 2,4,6-TCP photodegradation at Pt/TiO2 under visible light illumination, RSC Adv. 2 (2012) 12378–12383. doi:10.1039/C2RA21661B.

[9] Visible Light Absorption by Various Titanium Dioxide Specimens - The Journal of Physical Chemistry B (ACS Publications), (n.d.). https://pubs.acs.org/doi/abs/10.1021/jp064253b (accessed May 2, 2018).

[10] A. Houas, H. Lachheb, M. Ksibi, E. Elaloui, C. Guillard, J.-M. Herrmann, Photocatalytic degradation pathway of methylene blue in water, Applied Catalysis B: Environmental. 31 (2001) 145–157. doi:10.1016/S0926-3373(00)00276-9.

[11] V. Kandavelu, H. Kastien, K.R. Thampi, Photocatalytic degradation of isothiazolin-3-ones in water and emulsion paints containing nanocrystalline TiO2 and ZnO catalysts, Applied Catalysis B: Environmental. 48 (2004) 101–111. doi:10.1016/j.apcatb.2003.09.022.

[12] C.H. Ao, S.C. Lee, J.Z. Yu, J.H. Xu, Photodegradation of formaldehyde by photocatalyst TiO2: effects on the presences of NO, SO2 and VOCs, Applied Catalysis B: Environmental. 54 (2004) 41–50. doi:10.1016/j.apcatb.2004.06.004.

[13] M. Stylidi, D.I. Kondarides, X.E. Verykios, Visible light-induced photocatalytic degradation of Acid Orange 7 in aqueous TiO2 suspensions, Applied Catalysis B: Environmental. 47 (2004) 189–201. doi:10.1016/j.apcatb.2003.09.014.

[14] M. Mrowetz, A. Villa, L. Prati, E. Selli, Effects of Au nanoparticles on TiO2 in the photocatalytic degradation of an azo dye, Gold Bull. 40 (2007) 154–160. doi:10.1007/BF03215573.

[15] M. Alvaro, C. Aprile, M. Benitez, E. Carbonell, H. García, Photocatalytic Activity of Structured Mesoporous TiO2 Materials, J. Phys. Chem. B. 110 (2006) 6661–6665. doi:10.1021/jp0573240.

[16] Y. Dong, Z. Bai, L. Zhang, R. Liu, T. Zhu, Finishing of cotton fabrics with aqueous nano-titanium dioxide dispersion and the decomposition of gaseous ammonia by ultraviolet irradiation, J. Appl. Polym. Sci. 99 (2006) 286–291. doi:10.1002/app.22476.

[17] M. Alvaro, B. Cojocaru, A.A. Ismail, N. Petrea, B. Ferrer, F.A. Harraz, V.I. Parvulescu, H. Garcia, Visible-light photocatalytic activity of gold nanoparticles supported on template-synthesized mesoporous titania for the decontamination of the chemical warfare agent Soman, Applied Catalysis B: Environmental. 99 (2010) 191–197. doi:10.1016/j.apcatb.2010.06.019.

[18] A. Fujishima, T.N. Rao, D.A. Tryk, Titanium dioxide photocatalysis, Journal of Photochemistry and Photobiology C: Photochemistry Reviews. 1 (2000) 1–21. doi:10.1016/S1389-5567(00)00002-2.

[19] K.B. Mogensen, K. Kneipp, Size-Dependent Shifts of Plasmon Resonance in Silver Nanoparticle Films Using Controlled Dissolution: Monitoring the Onset of Surface Screening Effects, J. Phys. Chem. C. 118 (2014) 28075–28083. doi:10.1021/jp505632n.

[20] Gold Nanoparticles: Properties and Applications, Sigma-Aldrich. (n.d.). http://www.sigmaaldrich.com/technical-documents/articles/materials-science/nanomaterials/gold-nanoparticles.html (accessed April 20, 2017).

[21] Silver Nanoparticles: Properties and Applications, Sigma-Aldrich. (n.d.). http://www.sigmaaldrich.com/materials-science/nanomaterials/silver-nanoparticles.html (accessed April 12, 2017).

[22] W. Huilei, L. Xiaoheng, Preparation of Silver Nanoparticle Loaded Mesoporous TiO2 and Its Photocatalytic Property, Wuji Cailiao Xuebao. 31 (2016) 560.

[23] P.L. Taylor, A.L. Ussher, R.E. Burrell, Impact of heat on nanocrystalline silver dressings: Part I: Chemical and biological properties, Biomaterials. 26 (2005) 7221–7229. doi:10.1016/j.biomaterials.2005.05.040.

[24] R. Tankhiwale, S.K. Bajpai, Graft copolymerization onto cellulose-based filter paper and its further development as silver nanoparticles loaded antibacterial food-packaging material, Colloids and Surfaces B: Biointerfaces. 69 (2009) 164–168. doi:10.1016/j.colsurfb.2008.11.004.

[25] S. Agnihotri, S. Mukherji, S. Mukherji, Size-controlled silver nanoparticles synthesized over the range 5–100 nm using the same protocol and their antibacterial efficacy, RSC Advances. 4 (2014) 3974–3983. doi:10.1039/C3RA44507K.

[26] E. López-Tobar, B. Hernández, M. Ghomi, S. Sanchez-Cortes, Stability of the Disulfide Bond in Cystine Adsorbed on Silver and Gold Nanoparticles As Evidenced by SERS Data, J. Phys. Chem. C. 117 (2013) 1531–1537. doi:10.1021/jp3112606.

[27] T.C. Dakal, A. Kumar, R.S. Majumdar, V. Yadav, Mechanistic Basis of Antimicrobial Actions of Silver Nanoparticles, Front Microbiol. 7 (2016). doi:10.3389/fmicb.2016.01831.

[28] Y. Cui, Y. Zhao, Y. Tian, W. Zhang, X. Lü, X. Jiang, The molecular mechanism of action of bactericidal gold nanoparticles on Escherichia coli, Biomaterials. 33 (2012) 2327–2333. doi:10.1016/j.biomaterials.2011.11.057.

[29] W.-R. Li, X.-B. Xie, Q.-S. Shi, H.-Y. Zeng, Y.-S. Ou-Yang, Y.-B. Chen, Antibacterial activity and mechanism of silver nanoparticles on Escherichia coli, Appl. Microbiol. Biotechnol. 85 (2010) 1115–1122. doi:10.1007/s00253-009-2159-5.

[30] N. Chandrasekharan, P.V. Kamat, Improving the Photoelectrochemical Performance of Nanostructured TiO2 Films by Adsorption of Gold Nanoparticles, J. Phys. Chem. B. 104 (2000) 10851–10857. doi:10.1021/jp0010029.

[31] H. Gerischer, M.E. Michel-Beyerle, F. Rebentrost, H. Tributsch, Sensitization of charge injection into semiconductors with large band gap, Electrochimica Acta. 13 (1968) 1509–1515. doi:10.1016/0013-4686(68)80076-3.

[32] J. Jaksik, H.J. Moore, T. Trad, O.I. Okoli, M.J. Uddin, Nanostructured functional materials for advanced three-dimensional (3D) solar cells, Sol. Energy Mater. Sol. Cells. 167 (2017) 121–132. doi:10.1016/j.solmat.2017.03.033.

[33] M.J. Alam, D.C. Cameron, Preparation and properties of transparent conductive aluminum-

doped zinc oxide thin films by sol–gel process, Journal of Vacuum Science & Technology A. 19 (2001) 1642–1646. doi:10.1116/1.1340659.

[34] A Perspective on Mesoporous TiO2 Materials - Chemistry of Materials (ACS Publications), (n.d.). https://pubs.acs.org/doi/abs/10.1021/cm4014859 (accessed May 3, 2018).

[35] A High Molar Extinction Coefficient Sensitizer for Stable Dye-Sensitized Solar Cells - Journal of the American Chemical Society (ACS Publications), (n.d.). https://pubs.acs.org/doi/abs/10.1021/ja0436190 (accessed May 3, 2018).

[36] J.D. Servaites, M.A. Ratner, T.J. Marks, Organic solar cells: A new look at traditional models, Energy Environ. Sci. 4 (2011) 4410–4422. doi:10.1039/C1EE01663F.

[37] C.A. Nelson, N.R. Monahan, X.-Y. Zhu, Exceeding the Shockley–Queisser limit in solar energy conversion, Energy Environ. Sci. 6 (2013) 3508–3519. doi:10.1039/C3EE42098A.

[38] Detailed Balance Limit of Efficiency of p□n Junction Solar Cells: Journal of Applied Physics: Vol 32, No 3, (n.d.). https://aip.scitation.org/doi/abs/10.1063/1.1736034 (accessed May 3, 2018).

[39] M. Green, Third Generation Photovoltaics: Advanced Solar Energy Conversion, Springer-Verlag, Berlin Heidelberg, 2003. //www.springer.com/us/book/9783540401377 (accessed May 3, 2018).

[40] J. Zhang, C. Yu, L. Wang, Y. Li, Y. Ren, K. Shum, Energy barrier at the N719-dye/$CsSnI_3$ interface for photogenerated holes in dye-sensitized solar cells, Scientific Reports. 4 (2014) 6954. doi:10.1038/srep06954.

[41] F. De Angelis, S. Fantacci, E. Mosconi, M.K. Nazeeruddin, M. Grätzel, Absorption Spectra and Excited State Energy Levels of the N719 Dye on TiO2 in Dye-Sensitized Solar Cell Models, J. Phys. Chem. C. 115 (2011) 8825–8831. doi:10.1021/jp111949a.

[42] M.F. Torresan, A.M. Baruzzi, R.A. Iglesias, Thermal annealing of photoanodes based on CdSe Qdots sensitized TiO2, Solar Energy Materials and Solar Cells. 155 (2016) 202–208. doi:10.1016/j.solmat.2016.06.015.

[43] Quantum Dot Solar Cells. Tuning Photoresponse through Size and Shape Control of CdSe−TiO2 Architecture - Journal of the American Chemical Society (ACS Publications), (n.d.). https://pubs.acs.org/doi/abs/10.1021/ja0782706 (accessed May 3, 2018).

[44] Synthesis and characterization of nearly monodisperse CdE (E = sulfur, selenium, tellurium) semiconductor nanocrystallites - Journal of the American Chemical Society (ACS Publications), (n.d.). https://pubs.acs.org/doi/abs/10.1021/ja00072a025 (accessed May 3, 2018).

[45] High fabrication yield organic tandem photovoltaics combining vacuum- and solution-processed subcells with 15% efficiency | Nature Energy, (n.d.). https://www.nature.com/articles/s41560-018-0134-z (accessed May 3, 2018).

[46] The influence of electrical effects on device performance of organic solar cells with nano-structured electrodes | Scientific Reports, (n.d.). https://www.nature.com/articles/s41598-017-05591-8 (accessed May 3, 2018).

[47] Efficiency of bulk-heterojunction organic solar cells - ScienceDirect, (n.d.). https://www.sciencedirect.com/science/article/pii/S0079670013000427 (accessed May 3, 2018).

[48] D.M. Huang, R. Faller, K. Do, A.J. Moulé, Coarse-Grained Computer Simulations of Polymer/Fullerene Bulk Heterojunctions for Organic Photovoltaic Applications, J. Chem. Theory Comput. 6 (2010) 526–537. doi:10.1021/ct900496t.

[49] P3HT/PCBM Bulk Heterojunction Organic Photovoltaics: Correlating Efficiency and Morphology - Nano Letters (ACS Publications), (n.d.). https://pubs.acs.org/doi/abs/10.1021/nl103482n (accessed May 3, 2018).

[50] P. Vanlaeke, A. Swinnen, I. Haeldermans, G. Vanhoyland, T. Aernouts, D. Cheyns, C. Deibel, J. D'Haen, P. Heremans, J. Poortmans, J.V. Manca, P3HT/PCBM bulk heterojunction solar cells: Relation between morphology and electro-optical characteristics, Solar Energy Materials and Solar Cells. 90 (2006) 2150–2158. doi:10.1016/j.solmat.2006.02.010.

[51] P3HT:PCBM, Best Seller in Polymer Photovoltaic Research - Dang - 2011 - Advanced Materials - Wiley Online Library, (n.d.). https://onlinelibrary.wiley.com/doi/abs/10.1002/adma.201100792 (accessed May 3, 2018).

[52] H. Tokuhisa, S. Tsukamoto, S. Morita, S. Ise, M. Tomita, N. Shirakawa, Fabrication of micro-textured surfaces for a high hydrophobicity by evaporative patterning using screen mesh templates, Appl. Surf. Sci. 400 (2017) 64–70. doi:10.1016/j.apsusc.2016.11.213.

[53] Z. Li, J. Meng, W. Wang, Z. Wang, M. Li, T. Chen, C.-J. Liu, The room temperature electron reduction for the preparation of silver nanoparticles on cotton with high antimicrobial activity, Carbohydrate Polymers. 161 (2017) 270–276. doi:10.1016/j.carbpol.2017.01.020.

[54] M.R. Nateghi, M. Shateri-Khalilabad, Silver nanowire-functionalized cotton fabric, Carbohydrate Polymers. 117 (2015) 160–168. doi:10.1016/j.carbpol.2014.09.057.

[55] T. Yuranova, D. Laub, J. Kiwi, Synthesis, activity and characterization of textiles showing self-cleaning activity under daylight irradiation, Catalysis Today. 122 (2007) 109–117.

doi:10.1016/j.cattod.2007.01.040.

[56] N. Veronovski, M. Sfiligoj-Smole, J.L. Viota, Characterization of TiO2/TiO2—SiO2 Coated Cellulose Textiles, Textile Research Journal. 80 (2010) 55–62. doi:10.1177/0040517509104012.

[57] M.J. Uddin, F. Cesano, F. Bonino, S. Bordiga, G. Spoto, D. Scarano, A. Zecchina, Photoactive TiO2 films on cellulose fibres: synthesis and characterization, Journal of Photochemistry and Photobiology A: Chemistry. 189 (2007) 286–294. doi:10.1016/j.jphotochem.2007.02.015.

[58] M.S.A. Amin, M.J. Uddin, M.A. Islam, Removal of azo dye by synthesized TiO2 nanoparticles, Nanomaterials and the Environment. 1 (2012) 18–22. doi:10.2478/nanome-2012-0003.

[59] D. Reyes-Coronado, G. Rodríguez-Gattorno, M.E. Espinosa-Pesqueira, C. Cab, R. de Coss, G. Oskam, Phase-pure TiO 2 nanoparticles: anatase, brookite and rutile, Nanotechnology. 19 (2008) 145605. doi:10.1088/0957-4484/19/14/145605.

[60] D.A.H. Hanaor, C.C. Sorrell, Review of the anatase to rutile phase transformation, Journal of Materials Science. 46 (2011). doi:10.1007/s10853-010-5113-0.

[61] L. Palmisano, M. Bellardita, A.D. Paola, Brookite, the Least Known TiO2 Photocatalyst, Catalysts. 3 (2013) 36–73.

[62] Tailoring the activity of Ti-based photocatalysts by playing with surface morphology and silver doping - ScienceDirect, (n.d.). http://www.sciencedirect.com/science/article/pii/S1010603007003930?via%3Dihub (accessed September 20, 2017).

[63] J. Livage, C. Sanchez, M. Henry, S. Doeuff, The chemistry of the sol-gel process, Solid State Ionics. 32–33 (1989) 633–638. doi:10.1016/0167-2738(89)90338-X.

[64] P. Kajitvichyanukul, J. Ananpattarachai, S. Pongpom, Sol–gel preparation and properties study of TiO2 thin film for photocatalytic reduction of chromium(VI) in photocatalysis process, Science and Technology of Advanced Materials. 6 (2005) 352–358. doi:10.1016/j.stam.2005.02.014.

[65] P.H. Davis, C.P. Morrisey, S.M.V. Tuley, C.I. Bingham, Synthesis and Stabilization of Colloidal Gold Nanoparticle Suspensions for SERS, in: Nanoparticles: Synthesis, Stabilization, Passivation, and Functionalization, American Chemical Society, 2008: pp. 16–30. doi:10.1021/bk-2008-0996.ch002.

[66] P. Priecel, H. Adekunle Salami, R.H. Padilla, Z. Zhong, J.A. Lopez-Sanchez, Anisotropic gold nanoparticles: Preparation and applications in catalysis, Chinese Journal of Catalysis. 37 (2016) 1619–1650. doi:10.1016/S1872-2067(16)62475-0.

[67] C. Renz, Über die Einwirkung von Oxyden auf Silbernitrat und Goldchlorid im Licht, HCA. 15 (1932) 1077–1084. doi:10.1002/hlca.193201501118.

[68] S. Boufi, A.M. Ferraria, A.M.B. do Rego, N. Battaglini, F. Herbst, M.R. Vilar, Surface functionalisation of cellulose with noble metals nanoparticles through a selective nucleation, Carbohydrate Polymers. 86 (2011) 1586–1594. doi:10.1016/j.carbpol.2011.06.067.

[69] J.-H. Kim, K.M. Twaddle, J. Hu, H. Byun, Sunlight-Induced Synthesis of Various Gold Nanoparticles and Their Heterogeneous Catalytic Properties on a Paper-Based Substrate, ACS Appl. Mater. Interfaces. 6 (2014) 11514–11522. doi:10.1021/am503745w.

[70] H. Lachheb, E. Puzenat, A. Houas, M. Ksibi, E. Elaloui, C. Guillard, J.-M. Herrmann, Photocatalytic degradation of various types of dyes (Alizarin S, Crocein Orange G, Methyl Red, Congo Red, Methylene Blue) in water by UV-irradiated titania, Applied Catalysis B: Environmental. 39 (2002) 75–90. doi:10.1016/S0926-3373(02)00078-4.

[71] J. Cenens, Visible Spectroscopy of Methylene Blue on Hectorite, Laponite B, and Barasym in Aqueous Suspension, Clays and Clay Minerals. 36 (1988) 214–224. doi:10.1346/CCMN.1988.0360302.

[72] A. Kay, M. Grätzel, Low cost photovoltaic modules based on dye sensitized nanocrystalline titanium dioxide and carbon powder, Solar Energy Materials and Solar Cells. 44 (1996) 99–117. doi:10.1016/0927-0248(96)00063-3.

[73] G. Guan, Z. Yang, L. Qiu, X. Sun, Z. Zhang, J. Ren, H. Peng, Oriented PEDOT:PSS on aligned carbon nanotubes for efficient dye-sensitized solar cells, J. Mater. Chem. A. 1 (2013) 13268–13273. doi:10.1039/C3TA12669B.

[74] Freestanding Aligned Carbon Nanotube Array Grown on a Large□Area Single□Layered Graphene Sheet for Efficient Dye□Sensitized Solar Cell - Qiu - 2015 - Small - Wiley Online Library, (n.d.). https://onlinelibrary.wiley.com/doi/abs/10.1002/smll.201400703 (accessed May 7, 2018).

[75] A New and General Fabrication of an Aligned Carbon Nanotube/Polymer Film for Electrode Applications - Huang - 2011 - Advanced Materials - Wiley Online Library, (n.d.). https://onlinelibrary.wiley.com/doi/abs/10.1002/adma.201102472 (accessed May 7, 2018).

[76] S. Zhang, C. Ji, Z. Bian, R. Liu, X. Xia, D. Yun, L. Zhang, C. Huang, A. Cao, Single-Wire Dye-Sensitized Solar Cells Wrapped by Carbon Nanotube Film Electrodes, Nano Lett. 11 (2011) 3383–3387. doi:10.1021/nl201790w.

[77] J. Liang, G. Zhang, J. Yin, Y. Yang, Transparent, 3-dimensional light-collected, and flexible fiber-type dye-sensitized solar cells based on highly ordered hierarchical anatase TiO2

nanorod arrays, Journal of Power Sources. 272 (2014) 719–729. doi:10.1016/j.jpowsour.2014.09.002.

[78] M. Peng, X. Yu, X. Cai, Q. Yang, H. Hu, K. Yan, H. Wang, B. Dong, F. Zhu, D. Zou, Waveguide fiber dye-sensitized solar cells, Nano Energy. 10 (2014) 117–124. doi:10.1016/j.nanoen.2014.07.011.

[79] G. Liu, X. Gao, H. Wang, A.-Y. Kim, Z. Zhao, J.K. Lee, D. Zou, A novel photoanode with high flexibility for fiber-shaped dye sensitized solar cells, J. Mater. Chem. A. 4 (2016) 5925–5931. doi:10.1039/C5TA10488B.

[80] Y. Rui, Y. Wang, Q. Zhang, Q. Chi, M. Zhang, H. Wang, Y. Li, C. Hou, In-situ construction of three-dimensional titania network on Ti foil toward enhanced performance of flexible dye-sensitized solar cells, Applied Surface Science. 380 (2016) 210–217. doi:10.1016/j.apsusc.2016.01.156.

[81] Z. Li, Y. Zhou, Y. Yang, H. Dai, Electrophoretic deposition of graphene-TiO2 hierarchical spheres onto Ti thread for flexible fiber-shaped dye-sensitized solar cells, Materials & Design. 105 (2016) 352–358. doi:10.1016/j.matdes.2016.05.060.

[82] Photovoltaic Wire Derived from a Graphene Composite Fiber Achieving an 8.45 % Energy Conversion Efficiency - Yang - 2013 - Angewandte Chemie International Edition - Wiley Online Library, (n.d.). https://onlinelibrary.wiley.com/doi/abs/10.1002/anie.201301776 (accessed May 7, 2018).

[83] L. Chen, Y. Zhou, H. Dai, T. Yu, J. Liu, Z. Zou, One-step growth of CoNi2S4 nanoribbons on carbon fibers as platinum-free counter electrodes for fiber-shaped dye-sensitized solar cells with high performance: Polymorph-dependent conversion efficiency, Nano Energy. 11 (2015) 697–703. doi:10.1016/j.nanoen.2014.11.047.

[84] X. Ma, H. Elbohy, S. Sigdel, C. Lai, Q. Qiao, H. Fong, Electrospun carbon nano-felt derived from alkali lignin for cost-effective counter electrodes of dye-sensitized solar cells, RSC Adv. 6 (2016) 11481–11487. doi:10.1039/C5RA23856K.

[85] T. Chen, L. Qiu, Z. Cai, F. Gong, Z. Yang, Z. Wang, H. Peng, Intertwined Aligned Carbon Nanotube Fiber Based Dye-Sensitized Solar Cells, Nano Lett. 12 (2012) 2568–2572. doi:10.1021/nl300799d.

[86] S. Mallakpour, S. Soltanian, Surface functionalization of carbon nanotubes: fabrication and applications, RSC Adv. 6 (2016) 109916–109935. doi:10.1039/C6RA24522F.

[87] Hybrid solar cell on a carbon fiber. - PubMed - NCBI, (n.d.). https://www.ncbi.nlm.nih.gov/pubmed/27216603 (accessed May 7, 2018).

[88] M. Peng, D. Zou, Flexible fiber/wire-shaped solar cells in progress: properties, materials, and designs, J. Mater. Chem. A. 3 (2015) 20435–20458. doi:10.1039/C5TA03731J.

[89] J. Yan, M.J. Uddin, T.J. Dickens, D.E. Daramola, O.I. Okoli, 3D Wire-Shaped Dye-Sensitized Solar Cells in Solid State Using Carbon Nanotube Yarns with Hybrid Photovoltaic Structure, Advanced Materials Interfaces. 1 (2014) 1400075. doi:10.1002/admi.201400075.

[90] Quantum dots: promises and accomplishments - ScienceDirect, (n.d.). https://www.sciencedirect.com/science/article/pii/S1369702111701833 (accessed May 8, 2018).

[91] Review paper: Toward highly efficient quantum-dot- and dye-sensitized solar cells - ScienceDirect, (n.d.). https://www.sciencedirect.com/science/article/pii/S1567173913000539 (accessed May 8, 2018).

[92] R.J. Ellingson, M.C. Beard, J.C. Johnson, P. Yu, O.I. Micic, A.J. Nozik, A. Shabaev, A.L. Efros, Highly Efficient Multiple Exciton Generation in Colloidal PbSe and PbS Quantum Dots, Nano Lett. 5 (2005) 865–871. doi:10.1021/nl0502672.

[93] J. Yu, W. Wang, Z. Pan, J. Du, Z. Ren, W. Xue, X. Zhong, Quantum dot sensitized solar cells with efficiency over 12% based on tetraethyl orthosilicate additive in polysulfide electrolyte, J. Mater. Chem. A. 5 (2017) 14124–14133. doi:10.1039/C7TA04344A.

[94] A. Matlack, Introduction to Green Chemistry, Second Edition, CRC Press, 2010.

[95] A.L. Gollenberg, M.L. Hediger, P.A. Lee, J.H. Himes, G.M. Buck Louis, Association between Lead and Cadmium and Reproductive Hormones in Peripubertal U.S. Girls, Environ Health Perspect. 118 (2010) 1782–1787. doi:10.1289/ehp.1001943.

[96] D.E. Keil, J. Berger-Ritchie, G.A. McMillin, Testing for Toxic Elements: A Focus on Arsenic, Cadmium, Lead, and Mercury, Lab Med. 42 (2011) 735–742. doi:10.1309/LMYKGU05BEPE7IAW.

[97] N.V. Hullavarad, S.S. Hullavarad, P.C. Karulkar, Cadmium sulphide (CdS) nanotechnology: synthesis and applications, J Nanosci Nanotechnol. 8 (2008) 3272–3299.

[98] L.E. Brus, Electron–electron and electron□hole interactions in small semiconductor crystallites: The size dependence of the lowest excited electronic state, The Journal of Chemical Physics. 80 (1984) 4403–4409. doi:10.1063/1.447218.

[99] Ligand Control of Growth, Morphology, and Capping Structure of Colloidal CdSe Nanorods - Chemistry of Materials (ACS Publications), (n.d.). https://pubs.acs.org/doi/abs/10.1021/cm0705791 (accessed May 8, 2018).

[100] M. Salavati-Niasari, M. Esmaeili-Zare, A. Sobhani, Synthesis and characterisation of

cadmium selenide nanostructures by simple sonochemical method, IET Micro Nano Letters. 7 (2012) 831–834. doi:10.1049/mnl.2012.0443.

[101] S.P. Malyukov, A.V. Sayenko, I.A. Kirichenko, Laser sintering of a TiO<Subscript>2</Subscript> nanoporous film on a flexible substrate for application in solar cells, Semiconductors. 50 (2016) 1198–1202. doi:10.1134/S1063782616090153.

[102] Serrated, flexible and ultrathin polyaniline nanoribbons: An efficient counter electrode for the dye-sensitized solar cell - ScienceDirect, (n.d.). https://www.sciencedirect.com/science/article/pii/S0378775316305596 (accessed May 8, 2018).

[103] M. Gerosa, A. Sacco, A. Scalia, F. Bella, A. Chiodoni, M. Quaglio, E. Tresso, S. Bianco, Toward Totally Flexible Dye-Sensitized Solar Cells Based on Titanium Grids and Polymeric Electrolyte, IEEE Journal of Photovoltaics. 6 (2016) 498–505. doi:10.1109/JPHOTOV.2016.2514702.

[104] C. Du, Y. Ji, J. Xue, T. Hou, J. Tang, S.-T. Lee, Y. Li, Morphology and Performance of Polymer Solar Cell Characterized by DPD Simulation and Graph Theory, Scientific Reports. 5 (2015) 16854. doi:10.1038/srep16854.

[105] S. Wu, S. Li, Q. Sun, C. Huang, M.-K. Fung, Highly Efficient White Organic Light-Emitting Diodes with Ultrathin Emissive Layers and a Spacer-Free Structure, Scientific Reports. 6 (2016) 25821. doi:10.1038/srep25821.

[106] D. Chi, S. Qu, Z. Wang, J. Wang, High efficiency P3HT:PCBM solar cells with an inserted PCBM layer, J. Mater. Chem. C. 2 (2014) 4383–4387. doi:10.1039/C4TC00003J.

[107] Electrolytes in Dye-Sensitized Solar Cells - Chemical Reviews (ACS Publications), (n.d.). https://pubs.acs.org/doi/full/10.1021/cr400675m?src=recsys (accessed May 8, 2018).

[108] B. Conings, S. Bertho, K. Vandewal, A. Senes, J. D'Haen, J. Manca, R.A.J. Janssen, Modeling the temperature induced degradation kinetics of the short circuit current in organic bulk heterojunction solar cells, Appl. Phys. Lett. 96 (2010) 163301. doi:10.1063/1.3391669.

[109] S.B. Dkhil, M. Pfannmöller, M.I. Saba, M. Gaceur, H. Heidari, C. Videlot□Ackermann, O. Margeat, A. Guerrero, J. Bisquert, G. Garcia□Belmonte, A. Mattoni, S. Bals, J. Ackermann, Toward High-Temperature Stability of PTB7-Based Bulk Heterojunction Solar Cells: Impact of Fullerene Size and Solvent Additive, Advanced Energy Materials. 7 (2017) 1601486. doi:10.1002/aenm.201601486.

[110] J.M. Peralta, B.E. Meza, S.E. Zorrilla, Mathematical Modeling of a Dip-Coating Process Using a Generalized Newtonian Fluid. 1. Model Development, Ind. Eng. Chem. Res. 53 (2014) 6521–6532. doi:10.1021/ie500407t.

[111] L. Landau, B. Levich, Dragging of a Liquid by a Moving Plate, in: P. Pelcé (Ed.), Dynamics of Curved Fronts, Academic Press, San Diego, 1988: pp. 141–153. doi:10.1016/B978-0-08-092523-3.50016-2.

[112] Chapter 10 Dip Coating - Semantic Scholar, (n.d.). /paper/Chapter-10-Dip-Coating-Coating-Brinker/9a86efbac2d107c42b100f3f1fd1c50e66dee7ee (accessed May 30, 2018).

[113] B.B. Sauer, G.T. Dee, Molecular weight and temperature dependence of polymer surface tension: comparison of experiment with theory, Macromolecules. 24 (1991) 2124–2126. doi:10.1021/ma00008a070.

[114] M. Javidi Soufiani, Investigation And Modeling of Dip-Coating Process for Dispersions, Electronic Thesis and Dissertation Repository. (2016). https://ir.lib.uwo.ca/etd/3641.

[115] E. Blanco, J.M. González-Leal, M. Ramírez-del Solar, Photocatalytic TiO2 sol–gel thin films: Optical and morphological characterization, Solar Energy. 122 (2015) 11–23. doi:10.1016/j.solener.2015.07.048.

[116] R. Mechiakh, F. Meriche, R. Kremer, R. Bensaha, B. Boudine, A. Boudrioua, TiO2 thin films prepared by sol–gel method for waveguiding applications: Correlation between the structural and optical properties, Optical Materials. 30 (2007) 645–651. doi:10.1016/j.optmat.2007.02.047.

[117] R.C. Suciu, E. Indrea, T.D. Silipas, S. Dreve, M.C. Rosu, V. Popescu, G. Popescu, H.I. Nascu, TiO 2 thin films prepared by sol – gel method, J. Phys.: Conf. Ser. 182 (2009) 012080. doi:10.1088/1742-6596/182/1/012080.

[118] M.J. Uddin, F. Cesano, D. Scarano, F. Bonino, G. Agostini, G. Spoto, S. Bordiga, A. Zecchina, Cotton textile fibres coated by Au/TiO2 films: Synthesis, characterization and self cleaning properties, Journal of Photochemistry and Photobiology A: Chemistry. 199 (2008) 64–72. doi:10.1016/j.jphotochem.2008.05.004.

[119] H.-H. Wang, C. Su, H.-S. Chen, Y.-C. Liu, Y.-W. Hsu, N.-M. Hsu, W.-R. Li, Preparation of Nanoporous TiO2 Electrodes for Dye-Sensitized Solar Cells, Journal of Nanomaterials. (2011). doi:10.1155/2011/547103.

[120] E.C. Muniz, M.S. Góes, J.J. Silva, J.A. Varela, E. Joanni, R. Parra, P.R. Bueno, Synthesis and characterization of mesoporous TiO2 nanostructured films prepared by a modified sol–gel method for application in dye solar cells, Ceramics International. 37 (2011) 1017–1024. doi:10.1016/j.ceramint.2010.11.014.

[121] B.-H. Moon, Y.-M. Sung, C.-H. Han, Titanium oxide Films Prepared by Sputtering, Sol Gel and Dip Coating Methods for Photovoltaic Application, Energy Procedia. 34 (2013) 589–596. doi:10.1016/j.egypro.2013.06.789.

[122] E. Rio, F. Boulogne, Withdrawing a solid from a bath: how much liquid is coated?, Advances in Colloid and Interface Science. 247 (2017) 100–114. doi:10.1016/j.cis.2017.01.006.

[123] F. S. Goucher, H. Ward, A problem in viscosity., Phil Mag. 44 (1922) 1002–1014.

[124] D.W.H. Rankin, CRC handbook of chemistry and physics, 89th edition, edited by David R. Lide, Crystallography Reviews. 15 (2009) 223–224. doi:10.1080/08893110902764125.

[125] 108-90-7 CAS | CHLOROBENZENE | Aryl Halides | Article No. 02736, (n.d.). https://www.lobachemie.com/aryl-halides-02736/CHLOROBENZENE-CASNO-108-90-7.aspx (accessed May 30, 2018).

[126] C. Wei, J. Zhuang, Y. Chen, D. Zhang, W. Su, Z. Cui, Highly Air-Stable Electron-Transport Material for Ink-Jet-Printed OLEDs, Chemistry – A European Journal. 22 (n.d.) 16576–16585. doi:10.1002/chem.201603994.

[127] S. Liu, X. Zhang, L. Zhang, W. Xie, Ultrasonic spray coating polymer and small molecular organic film for organic light-emitting devices, Scientific Reports. 6 (2016) 37042. doi:10.1038/srep37042.

[128] M.A. Rocha, J.N. Low, L.R. Gomes, A. Quesada, L.M.N.B.F. Santos, 2,6-Diphenyl-pyridine, Acta Cryst E, Acta Cryst Sect E, Acta Crystallogr E, Acta Crystallogr Sect E, Acta Crystallogr E Struct Rep Online, Acta Crystallogr Sect E Struct Rep Online. 63 (2007) o4833–o4833. doi:10.1107/S1600536807058850.

[129] TmPyPB 790907, Sigma-Aldrich. (n.d.). https://www.sigmaaldrich.com/catalog/product/aldrich/790907 (accessed May 31, 2018).

[130] F. Machui, S. Langner, X. Zhu, S. Abbott, C.J. Brabec, Determination of the P3HT:PCBM solubility parameters via a binary solvent gradient method: Impact of solubility on the photovoltaic performance, Solar Energy Materials and Solar Cells. 100 (2012) 138–146. doi:10.1016/j.solmat.2012.01.005.

[131] Y. Sun, Y. Han, J. Liu, Controlling PCBM aggregation in P3HT/PCBM film by a selective solvent vapor annealing, Chin. Sci. Bull. 58 (2013) 2767–2774. doi:10.1007/s11434-013-5944-6.

[132] N. Chaudhary, R. Chaudhary, J.P. Kesari, A. Patra, Effect of composition ratio of P3HT:PC61BM in organic solar cells: optical and morphological properties, Materials Research Innovations. 22 (2018) 282–286. doi:10.1080/14328917.2017.1317061.

[133] R. de Bettignies, J. Leroy, M. Firon, C. Sentein, Study of P3HT:PCBM bulk heterojunction solar cells: influence of components ratio and of the nature of electrodes on performances and lifetime, in: Organic Photovoltaics VI, International Society for Optics and Photonics, 2005: p. 59380C. doi:10.1117/12.613454.

[134] W. R. Gambill, How to estimate mixtures viscositties, Chemical Engineering. 66 (1959) 151–152.

[135] J.G. Eberhart, The Surface Tension of Binary Liquid Mixtures1, J. Phys. Chem. 70 (1966) 1183–1186. doi:10.1021/j100876a035.

[136] Surface tension prediction for liquid mixtures - Escobedo - 1998 - AIChE Journal - Wiley Online Library, (n.d.). https://onlinelibrary.wiley.com/doi/abs/10.1002/aic.690441021 (accessed May 31, 2018).

[137] Y. Ding, W. Xu, W. Wang, H. Fong, Z. Zhu, Scalable and Facile Preparation of Highly Stretchable Electrospun PEDOT:PSS@PU Fibrous Nonwovens toward Wearable Conductive Textile Applications, ACS Appl. Mater. Interfaces. 9 (2017) 30014–30023. doi:10.1021/acsami.7b06726.

[138] PEDOT:PSS | Poly(3,4-ethylenedioxythiophene)-poly(styrenesulfonate) 2.2-2.6% in H2O, (high-conductivity grade) | Sigma-Aldrich, (n.d.). https://www.sigmaaldrich.com/catalog/product/aldrich/655201?lang=en&region=US (accessed May 31, 2018).

[139] F. Amano, K. Nogami, M. Tanaka, B. Ohtani, Correlation between Surface Area and Photocatalytic Activity for Acetaldehyde Decomposition over Bismuth Tungstate Particles with a Hierarchical Structure, Langmuir. 26 (2010) 7174–7180. doi:10.1021/la904274c.

[140] Photocatalytic activity, surface area and phase modification of mesoporous SiO2–TiO2 prepared by a one-step hydrothermal procedure - ScienceDirect, (n.d.). https://www.sciencedirect.com/science/article/pii/S027288421400412X (accessed May 9, 2018).

[141] K. Al-Attafi, A. Nattestad, Y. Yamauchi, S.X. Dou, J.H. Kim, Aggregated mesoporous nanoparticles for high surface area light scattering layer TiO 2 photoanodes in Dye-sensitized Solar Cells, Scientific Reports. 7 (2017) 10341. doi:10.1038/s41598-017-09911-w.

[142] E. Albiter, M.A. Valenzuela, S. Alfaro, G. Valverde-Aguilar, F.M. Martínez-Pallares, Photocatalytic deposition of Ag nanoparticles on TiO2: Metal precursor effect on the structural and photoactivity properties, Journal of Saudi Chemical Society. 19 (2015) 563–573. doi:10.1016/j.jscs.2015.05.009.

[143] S. Eustis, M.A. El-Sayed, Why gold nanoparticles are more precious than pretty gold: Noble metal surface plasmon resonance and its enhancement of the radiative and nonradiative properties of nanocrystals of different shapes, Chem. Soc. Rev. 35 (2006) 209–217. doi:10.1039/B514191E.

[144] W. Haiss, N.T.K. Thanh, J. Aveyard, D.G. Fernig, Determination of Size and Concentration of Gold Nanoparticles from UV−Vis Spectra, Anal. Chem. 79 (2007) 4215–4221. doi:10.1021/ac0702084.

[145] M.A. Moharram, T.Z. Abou El Nasr, N.A. Hakeem, X-Ray diffraction and infrared studies on the effect of thermal treatments on cotton celluloses I and II, J. Polym. Sci. B Polym. Lett. Ed. 19 (1981) 183–187. doi:10.1002/pol.1981.130190405.

[146] E.K. Golz, D.A. Vander Griend, Modeling methylene blue aggregation in acidic solution to the limits of factor analysis, Anal. Chem. 85 (2013) 1240–1246. doi:10.1021/ac303271m.

[147] H. Zhu, R. Jiang, L. Xiao, Y. Chang, Y. Guan, X. Li, G. Zeng, Photocatalytic decolorization and degradation of Congo Red on innovative crosslinked chitosan/nano-CdS composite catalyst under visible light irradiation, J. Hazard. Mater. 169 (2009) 933–940. doi:10.1016/j.jhazmat.2009.04.037.

[148] Y.A. Attia, D. Buceta, F.G. Requejo, L.J. Giovanetti, M.A. López-Quintela, Photostability of gold nanoparticles with different shapes: the role of Ag clusters, Nanoscale. 7 (2015) 11273–11279. doi:10.1039/C5NR01887K.

[149] H. Fan, G. Li, F. Yang, L. Yang, S. Zhang, Photodegradation of cellulose under UV light catalysed by TiO2, Journal of Chemical Technology & Biotechnology. 86 (2011) 1107–1112. doi:10.1002/jctb.2632.

[150] D. Klemm, B. Heublein, H.-P. Fink, A. Bohn, Cellulose: Fascinating Biopolymer and Sustainable Raw Material, Angewandte Chemie International Edition. 44 (2005) 3358–3393. doi:10.1002/anie.200460587.

[151] C. Chung, M. Lee, E.K. Choe, Characterization of cotton fabric scouring by FT-IR ATR spectroscopy, Carbohydrate Polymers. 58 (2004) 417–420. doi:10.1016/j.carbpol.2004.08.005.

[152] R. Beranek, H. Kisch, Tuning the optical and photoelectrochemical properties of surface-modified TiO2, Photochem. Photobiol. Sci. 7 (2008) 40–48. doi:10.1039/b711658f.

[153] H.H. Lara, E.N. Garza-Treviño, L. Ixtepan-Turrent, D.K. Singh, Silver nanoparticles are broad-spectrum bactericidal and virucidal compounds, J Nanobiotechnology. 9 (2011) 30. doi:10.1186/1477-3155-9-30.

[154] X. Li, S.M. Robinson, A. Gupta, K. Saha, Z. Jiang, D.F. Moyano, A. Sahar, M.A. Riley, V.M. Rotello, Functional Gold Nanoparticles as Potent Antimicrobial Agents against Multi-Drug-Resistant Bacteria, ACS Nano. 8 (2014) 10682–10686. doi:10.1021/nn5042625.

[155] Y. Zhang, T.P. Shareena Dasari, H. Deng, H. Yu, Antimicrobial Activity of Gold

Nanoparticles and Ionic Gold, J Environ Sci Health C Environ Carcinog Ecotoxicol Rev. 33 (2015) 286–327. doi:10.1080/10590501.2015.1055161.

[156] A. Fujishima, K. Hashimoto, T. Watanabe, TiO2 photocatalysis: fundamentals and applications, Bkc, Tokyo, 1999.

[157] K. Sunada, Y. Kikuchi, K. Hashimoto, A. Fujishima, Bactericidal and Detoxification Effects of TiO2 Thin Film Photocatalysts, Environ. Sci. Technol. 32 (1998) 726–728. doi:10.1021/es970860o.

[158] J.S. Kim, E. Kuk, K.N. Yu, J.-H. Kim, S.J. Park, H.J. Lee, S.H. Kim, Y.K. Park, Y.H. Park, C.-Y. Hwang, Y.-K. Kim, Y.-S. Lee, D.H. Jeong, M.-H. Cho, Antimicrobial effects of silver nanoparticles, Nanomedicine: Nanotechnology, Biology and Medicine. 3 (2007) 95–101. doi:10.1016/j.nano.2006.12.001.

[159] K. Sunada, T. Watanabe, K. Hashimoto, Bactericidal Activity of Copper-Deposited TiO2 Thin Film under Weak UV Light Illumination, Environ. Sci. Technol. 37 (2003) 4785–4789. doi:10.1021/es034106g.

[160] L. Wei, P. Wang, Y. Yang, Y. Dong, R. Fan, W. Song, Y. Qiu, Y. Yang, T. Luan, Enhanced performance of dye sensitized solar cells by using a reduced graphene oxide/TiO2 blocking layer in the photoanode, Thin Solid Films. 639 (2017) 12–21. doi:10.1016/j.tsf.2017.08.011.

[161] O. Byrne, A. Coughlan, P.K. Surolia, K.R. Thampi, Succinonitrile-based solid-state electrolytes for dye-sensitised solar cells, Progress in Photovoltaics: Research and Applications. 23 (2015) 417–427. doi:10.1002/pip.2441.

[162] M. Suzuka, N. Hayashi, T. Sekiguchi, K. Sumioka, M. Takata, N. Hayo, H. Ikeda, K. Oyaizu, H. Nishide, A Quasi-Solid State DSSC with 10.1% Efficiency through Molecular Design of the Charge-Separation and -Transport, Scientific Reports. 6 (2016) 28022. doi:10.1038/srep28022.

[163] Solid-state composite electrolyte LiI/3-hydroxypropionitrile/SiO2 for dye-sensitized solar cells. - PubMed - NCBI, (n.d.). https://www.ncbi.nlm.nih.gov/pubmed/15853347 (accessed May 10, 2018).

[164] J.D. Roy-Mayhew, I.A. Aksay, Graphene Materials and Their Use in Dye-Sensitized Solar Cells, Chem. Rev. 114 (2014) 6323–6348. doi:10.1021/cr400412a.

[165] S. Lee, S. Lee, S. Choi, J. Kim, J. Kim, S. Kim, D. Lee, Improving the efficiency of a dye-sensitized solar cell with a reflex condenser system, Opt. Express, OE. 20 (2012) A908–A915. doi:10.1364/OE.20.00A908.

[166] Y.-W. Kim, B.-S. Kang, D.-W. Lee, Improving efficiency of dye-sensitized solar cell by micro reflectors, Int. J. Precis. Eng. Manuf. 16 (2015) 1257–1261. doi:10.1007/s12541-

015-0164-4.

[167] P. Ramasamy, J. Kim, Combined plasmonic and upconversion rear reflectors for efficient dye-sensitized solar cells, Chem. Commun. 50 (2013) 879–881. doi:10.1039/C3CC47290F.

BIOGRAPHICAL SKETCH

Jared Ray Jaksik started his Master's program at the University of Texas Rio Grande Valley in 2016. He received his Bachelor's of Science degree (2016) in Chemistry from the University of Texas at Austin. He worked as a research assistant at the Nanostructured Surface and Interface Science Lab under Dr. Mohammed Uddin during his Master's studies. He received his Master's of Science degree in Chemistry in August of 2018. He can be reached at: Jaksik3@gmail.com.